Identifikacija novih monogenskih uzroka segmentalnih progeroidnih sindroma

Lessel, Davor

Doctoral thesis / Disertacija

2020

Degree Grantor / Ustanova koja je dodijelila akademski / stručni stupanj: **University of Split, School of Medicine / Sveučilište u Splitu, Medicinski fakultet**

Permanent link / Trajna poveznica: https://urn.nsk.hr/urn:nbn:hr:171:120702

Rights / Prava: In copyright/Zaštićeno autorskim pravom.

Download date / Datum preuzimanja: **2024-05-22**

SVEUČILISTE U SPLITU

MEDICINSKI FAKULTET

Davor Lessel

IDENTIFIKACIJA NOVIH MONOGENSKIH UZROKA SEGMENTALNIH PROGEROIDNIH SINDROMA

Doktorska disertacija

Hamburg, 2020

SVEUČILISTE U SPLITU

MEDICINSKI FAKULTET

Davor Lessel

IDENTIFIKACIJA NOVIH MONOGENSKIH UZROKA SEGMENTALNIH PROGEROIDNIH SINDROMA

Doktorska disertacija

Hamburg, 2020

Doktorska disertacija sadrži rezultate znanstvenih istraživanja provedenih pri institutima za humanu genetiku, sveučilišnih bolnica u Kölnu, Ulmu i Hamburgu, u SR Njemačkoj

VODITELJ RADA: izv. prof. dr. sc. Ivana Marinović Terzić

SADRŽAJ

1.) POPIS OZNAKA I KRATICA

HEK293T: stanična linija izvorno uzgojena iz bubrežnih stanica ljudskog embrija koji izražava mutantnu verziju SV40 velikog T antigena (engl. *Human Embryonic Kidney cells that express a mutant version of the SV40 large T antigen*)

HGPS: Hutchinson-Gilford progerijski sindrom (engl. *Hutchinson-Gilford Progeria syndrome*)

LMNA: lamin A/C, gen mutiran kod Hutchinson-Gilfordovog progerijskog sindroma

LCL: limfoblastne stanične linije (engl. *lymphoblastoid cell lines*)

OMIM: baza podataka u kojoj su zabilježeni ljudski geni i njihove mutacije (engl. *Online Mendelian Inheritance in Man*, https://omim.org/)

RecQL4: gen mutiran kod Rothmund-Tomsonovog sindroma (engl. *ATP-dependent DNA helicase Q4*)

U2OS: stanična linija uzgojena iz koštanog tkiva petnaestogodišnje djevojke koja je bolovala od osteosarkoma (engl. *Human Bone Osteosarcoma Epithelial Cells*)

WRN: gen mutiran kod Wernerovog sindroma (engl. *Werner syndrome ATP-dependent helicase*)

WS: Wernerov sindrom (engl. *Werner syndrome*),

2) UVOD

Starenje je sa sigurnošću jedan od najkompliciranijih bioloških procesa u ljudskom tijelu i jedan od rijetkih kroz koji svaki čovjek neminovno prolazi. Za ovaj proces se smatra da je reguliran kompleksnim interakcijama genetskog naslijeđa i utjecajima najrazličitijih vanjskih faktora. Usprkos velikom napretku u istraživanjima posljednjih godina, stanični mehanizmi koji reguliraju fiziološko i patološko starenje još uvijek nisu u potpunosti razjašnjeni. Bolesti povezane sa starijom životnom dobi postaju sve važnije za zdravstvene sustave budući da svjetska populacija, a posebno populacija tzv. zapadnog svijeta posljednjih desetljeća neprekidno produžuje životni vijek. Sukladno tome, bolesti povezane s visokom životnom dobi predstavljaju jedan od glavnih izazova za zdravstvene sustave.

Proces starenja moguće je proučavati na različite načine. Jedna od mogućnosti su istraživanja na samih starijim osobama, tj. ciljana istraživanja oboljenja koja su povezana s visokom životnom dobi kao primjerice poremećaji sluha i vida, demencija, dijabetes melitus tipa 2, osteoporoza, ateroskleroza i koronarne bolesti srca, i različiti zloćudni tumori. Također, mnogi znanstvenici koriste razne životinjske modele, od miševa, štakora, crva do voćnih mušica kako bi otkrili molekularne mehanizme koji reguliraju različite procese starenja, te identificirali molekularno-definirane lijekove za profilaksu i/ili terapiju.

Jedan mogući pristup istraživanju procesa starenja je i istraživanje sindroma prijevremenog/ubrzanog starenja nazvanih segmentalni progeroidni sindromi. Segmentalni progeroidni sindromi su izrazito rijetki, klinički i genetski heterogeni poremećaji koje karakteriziraju znakovi preranog/ubrzanog starenja, koji pogađaju više tkiva ili organa (1, 2). Kao humanog genetičara ovi sindromi su posebno privukli moju pažnju zato što se u velikoj većini slučajeva radi o tzv. monogenskim oboljenjima. To znači da su ovi sindromi uzrokovani jednom izmjenom u ljudskom genomu, mutacijom u specifičnom genu, koja određuje kliničku sliku i tijek bolesti. Identifikacija genetskih uzroka segmentalnih progeroidnih sindroma, te analiza njihovih molekularnih mehanizama mogla bi doprinijeti razvoju ciljanih terapijskih pristupa kako bi se poboljšala skrb za bolesti povezane s visokom životnom dobi općenito. Ova pretpostavka se ne temelji samo na činjenici da pacijenti koji boluju od segmentalnog progeroidnog sindroma rano razvijaju cijeli niz simptoma koji su tipični za starije osobe, nego i na sličnosti glavnih molekularnih obilježja tzv. fiziološkog starenja i starenja kod segmentalnih progeroidnih sindroma (2). Naime, glavna molekularna obilježja oba procesa starenja uključuju disfunkciju telomera, genomsku nestabilnost, mitohondrijsku disfunkciju, iscrpljivanje baze matičnih stanica, senescenciju stanica, deregulaciju staničnog ciklusa, epigenetske promjene i upalne procese (3, 4).

Do sada je u literaturi opisano preko 100 različitih segmentalnih progeroidnih sindroma, koji se s obzirom na dob kada oboljeli razvijaju prve simptome mogu podijeliti na kongenitalne, juvenilne i adultne (2). Najpoznatiji i do sada najbolje istraženi primjeri ovih sindroma su Wernerov sindrom (WS, engl. *Werner syndrome*), uzrokovan autosomalno recesivnim mutacijama u *WRN* genu (5) i Hutchinson-Gilford progerijski sindrom (HGPS, engl. *Hutchinson-Gilford Progeria syndrome*), sindrom segmentalnog progeroida u ranom djetinjstvu, uzrokovan heterozigotnom *de novo* sinonimnom mutacijom u *LMNA* genu (6, 7).

Wernerov sindrom (OMIM # 277700) prvi je puta opisao u svojoj medicinskoj disertaciji njemački liječnik Otto C. W. Werner još 1904. godine (originalni naslov: „Über Katarakt in Verbindung mit Sklerodermie"). Wernerov sindrom je tipičan primjer tzv. adultnog segmentalnog progeroidnog sindroma. Naime, iako je prvi klinički simptom izostanak tipičnog naglog rasta na početku puberteta, kompletna klinička slika se razvija nakon 20. godine života. Tada oboljeli razvijaju sjedenje i/ili stanjivanje kose, sklerodermijske promjene na koži, atrofiju potkožnog masnog tkiva, te razvijaju specifičan visokotonski glas na osnovu kojega specijalisti za ovaj sindrom mogu pacijente prepoznati i razgovorom preko telefona. U daljnjem tijeku bolesti, pacijenti često razvijaju bilateralne katarakte, dijabetes melitus tipa 2, kožne ulceracije (tipično u predjelu gležnjeva), osteoporozu s posebnim zahvatom dugih kostiju, kalcifikaciju Ahilove tetive, hipogonadizam, aterosklerozu koronarnih žila s povećanim rizikom od infarkta, te različite tumore primjerice sarkome mekog tkiva, osteosarkome, melanome i karcinome štitnjače (8, 9). Najčešći uzroci smrti su posljedice kardiovaskularnih i malignih bolesti, a prosječni životni vijek je 54 godine (2).

Wernerova helikaza, protein koji kodira *WRN* gen, spada u obitelj proteina RecQ helikaza. Zanimljivo je da mutacije u dodatna dva člana ove obitelji proteina, naime, BLM i RecQL4, također uzrokuju segmentalne progeroidne sindrome, Bloomov sindrom (10) i Rothmund-Thomsonov sindrom (11). Funkcionalne analize Wernerove helikaze su pokazale da ovaj protein ima važnu ulogu u održavanju genomske stabilnosti na staničnoj razini, budući da sudjeluje u popravku DNA oštećenja, rekombinaciji i replikaciji DNA, transkripciji i regulaciji integriteta telomera (8, 12). Iz tog je razloga u primarnim stanicama oboljelih vidljiva izrazita genomska nestabilnost (13).

Zadnjih 11 godina surađujem s kolegama iz Međunarodnog registra za Wernerov sindrom (engl. *International   Registry   of   Werner   Syndrome*, http://www.wernersyndrome.org/registry/registry.html) s ciljem identifikacije genetskih uzroka kod oboljelih sa kliničkom slikom Wernerovog sindroma. Zajedničkim radom smo identificirali cijeli niz novih mutacija u *WRN* genu i detaljnije opisali razvoj ove bolesti (14-16). Nadalje smo pokazali da jedan dio pacijenata sa sličnom kliničkom slikom nosi uzročnu mutaciju u genima

koji su ranije bili asocirani sa razvojem segmentalnih progeroidnih sindroma, *LMNA* (17, 18) i *CTC1* genu (19), te identificirali *SAMHD1* gen kao mogući modifikator ovog sindroma (20). Iz moje perspektive jedan od najzanimljivijih otkrića je da smo pokazali da otprilike 10-15% pacijenata s kliničkom sumnjom na Wernerov sindrom nema uzročnu mutaciju u genima koji su ranije bili povezani s razvojem segmentalnih progeroidnih sindroma (14, 21). Ove osobe smo operativno klasificirali kao primjere atipičnog Wernerovog sindroma. Otkriće genetskog uzroka kod tih pacijenata, te klinička i funkcionalna karakterizacija novih genetskih uzroka je iz tog razloga moj glavni znanstveni cilj i interes.

Hutchinson-Gilford progerijski sindrom (OMIM # 176670) su neovisno jedan od drugoga prvi puta opisali 1886. i 1897. godine sir Jonathan Hutchinson i Hastings Gilford. Za razliku od Wernerovog sindroma, Hutchinson-Gilford progerijski sindrom predstavlja tipičan primjer tzv. juvenilnog segmentalnog progeroidnog sindroma. Naime, prvi klinički simptomi su vidljivi već krajem prve godine života, te oboljela djeca u toj dobi razvijaju karakteristični oblik lica s nerazvijenošću donje čeljusti, uskim mostom nosa i šiljastim nosom. Uz to, razvijaju progresivnu alopeciju s postepenim gubitkom obrva i trepavica, usporeni postnatalni rast, sklerodermijske promjene na koži, atrofiju potkožnog masnog tkiva, progresivne kontrakture zglobova i distrofiju noktiju. U daljnjem tijeku bolesti često razvijaju gubitak slušne provodljivosti, osteoporozu, kardiovaskularne bolesti, a neki oboljeli pokazuju i inzulinsku rezistenciju bez tipične šećerne bolesti. Najčešći uzroci smrti su posljedice komplikacija od ateroskleroze, miokardijalni infarkt i moždani udar, a prosječni životni vijek je otprilike 15 godina (2, 22).

LMNA gen kroz proces alternativnog izrezivanja kodira proteine lamin A i C (23), koji su integralni dio jezgrine lamine. Njihova primarna stanična funkcija je održavanje mehaničke stabilnosti jezgre stanice, stvaranje nuklearne ovojnice nakon mitoze, regulacija DNA replikacije i transkripcije, regulacija staničnog ciklusa, organizacija kromatina i diferencijacija stanica (24, 25). S obzirom na funkciju ovih proteina jedno od glavnih obilježja primarnih stanica oboljelih je deformacija oblika i funkcije jezgrine membrane (26). Daljnja istraživanja Hutchinson-Gilfordovog progerijskog sindroma identificirala su stvaranje skraćenog lamin A proteina, tzv. progerina, kao vjerojatan uzrok razvoja ove bolesti (27). Ovu je pretpostavku potkrijepila i naša identifikacija oboljelih s blažom kliničkom slikom koji proizvode manje progerina od tipičnih HGPS-a pacijenata (18).

U suradnji s kolegama iz Zaklade za istraživanje Progerije (engl. *Progeria Research Foundation*, https://www.progeriaresearch.org/) sam pokazao da otprilike 10% djece s kliničkom sumnjom na Hutchinson-Gilford progerijski sindrom nema uzročnu mutaciju u *LMNA* genu (28). Otkriće genetskog uzroka kod tih pacijenata, te klinička i funkcionalna karakterizacija novih genetskih uzroka je iz tog razloga moj glavni znanstveni cilj i interes.

Wiedemann–Rautenstrauchov sindroma (OMIM # 264090) su neovisno jedan od drugoga prvi puta opisali 1977. i 1979. Thomas Rautenstrauch i Hans-Rudolph Wiedemann. Od tada je u literaturi opisano oko 50 pacijenata ali genetski uzrok ovog sindroma nije bio otkriven (29). Wiedemann–Rautenstrauchov sindroma je tipičan primjer tzv. kongenitalnog segmentalnog progeroidnog sindroma. Naime, pacijenti pokazuju poremećaje rasta već prije rođenja, što dovodi do smanjene težine i smanjene veličine tijela pri samom rođenju. Nadalje ovi pacijenti pri rođenju prikazuju izrazito specifične promjene na glavi i licu koje uključuju rijetku kosu i izražene vene na vlasištu, trokutasto lice, duboko postavljene očne jabučice, mala usta s hipoplastičnom gornjom čeljusti, zube pri rođenju i šiljastu bradu. Često razvijaju perinatalne probleme s disanjem koji mogu i fatalno završiti. U daljnjem tijeku bolesti razvija se tanka i atrofična koža, atrofija potkožnog masnog tkiva, kontrakture zglobova, progresivna ataksija i tremor, kao i zastoj u mentalnom i motoričkom razvoju (2, 29). Potrebno je naglasiti da se kod ovog sindroma radi o izrazito karakterističnom i prepoznatljivom fenotipu (engl. *recognisable phenotype*), kojeg je moguće dijagnosticirati na osnovu kliničkih simptoma i posebnih, prepoznatljivih promjena na glavi i licu. Baš iz tog razloga je postojala u polju humane genetike velika zagonetka zašto nitko od znanstvenika koji su istraživali ovaj sindrom nije uspio identificirati njegov genetski uzrok. U suradnji s kolegama iz Zaklade za istraživanje progerije sam pokušao pronaći genetski uzrok kod troje djece s kliničkom sumnjom na Wiedemann–Rautenstrauchov sindrom.

3) CILJ OBJEDINJENIH RADOVA

Cilj istraživanja znanstvenih radova objedinjenih u ovoj disertaciji bio je:

1. Identificirati nove monogenske uzroke segmentalnih progeroidnih sindroma koristeći razne tehnike DNA analize, prvenstveno kombinacijom mapiranja homozigotnih regija genoma i sekvenciranjem kompletnog egzoma.

2. Otkriti na koji način mutacije u novim uzročnim genima na molekularnoj razini uzrokuju segmentalne progeroidne sindrome koristeći stanične modele (primarne dermalne fibroblaste pacijenata, Epstein-Barr virus-transformirane limfoblastne stanične linije (LCL), tumorske stanice U2OS i HEK293T) te ribice zebrice (Danio rerio).

3. Uraditi kliničku karakterizaciju novih segmentalnih progeroidnih sindroma, kako bi se s obzirom na kliničku sliku omogućilo postavljanje diferencijalne dijagnoze kod oboljelih sa sličnom kliničkom slikom.

4) ZNANSTVENI DOPRINOS OBJEDINJENIH RADOVA

Kao liječnik koji već više od 12 godina skrbi za pacijente oboljele od različitih genetskih poremećaja, uvidio sam da je najteže pogledati u oči teško oboljelog pacijenta i/ili njihovih roditelja i reći im da ne znam od čega boluju. Identifikacija novih monogenskih uzroka bolesti omogućuje kolegama u cijelom svijetu da kod pacijenata sa sličnim kliničkim simptomima postave diferencijalnu dijagnozu, te ciljano analiziraju novo-pronađene gene. Pravovremena dijagnoza monogenskih bolesti sprječava dijagnostičku potragu koja se nerijetko pretvara u pravu Odiseju, omogućava diferenciranu procjenu rizika od ponavljanja za roditelje i druge članove obitelji, te omogućava u sve većem broju slučajeva, primjerice kod Wernerovog sindroma i Hutchinson-Gilfordovog progerijskog sindroma, kreiranje personaliziranog programa prevencije. Sukladno tome i otkriće uzročnih mutacija u genima *SPRTN (30)*, *MDM2 (31)* i *POLR3A (28)*, kao genetskim uzrocima Ruijs-Aalfs sindroma (OMIM #616200), Lessel-Kubisch sindroma (OMIM # 618681) i Wiedemann–Rautenstrauch sindroma (OMIM #264090), omogućuje postavljanje pravovremene dijagnoze. Valja naglasiti da su ovi rezultati imali već i direktne kliničke implikacije. Naime u vrijeme identifikacije mutacija u *SPRTN* genu kao genetskog uzroka Ruijs-Aalfs sindroma, jedan od troje oboljelih još nije bio razvio hepatocelularni karcinom. Mjerama ranog otkrivanja, koje su uključivale redovitu sonografiju unutarnjih organa i magnetsku rezonancu, rak jetre otkriven je u vrlo ranoj fazi kod tada 14-godišnjeg dječaka. Pravovremeno je izvršena transplantacija jetre te mu je time produljen život. Rano postavljanje dijagnoze i kod druga dva sindroma koja su opisana u ovoj disertaciji također može produžiti život oboljelima. Primjerice kod Lessel-Kubisch sindroma može omogućiti praćenje rada bubrega i eventualnu transplantaciju slično kao i kod Ruijs-Aalfs sindroma. Isto tako, rana dijagnoza Wiedemann–Rautenstrauch sindroma omogućuje ciljano praćenje respiratornih problema, koji su glavni uzrok smrtnosti u perinatalnoj dobi.

Nadalje, rezultati ova tri objedinjena rada ukazuju na izrazitu genetsku i kliničku heterogenost segmentalnih progeroidnih sindroma, koja je najupečatljivija kod osoba koje boluju od kongenitalnog ili juvenilnog segmentalnog progeroidnog sindroma (28). Naime, petero pacijenata kod kojih sam otkrio autosomalno recesivne mutacije u *PYCR1* genu, su razvili većinu kliničkih karakteristika inače povezanih s Hutchinson-Gilfordovim progerijskim sindromom, iako samo u prve dvije godine života. Te su karakteristike bile trokutasti oblik lica, rijetka kosa, tanka i prozirna koža s istaknutim venama, mandibularna nerazvijenost i lipodistrofija. Mutacije u *PYCR1* genu su inicijalno bile identificirane kod pacijenata s Cutis Laxa tip IIB s progeroidnim simptomima (32), a kasnija istraživanja su pokazala izrazitu kliničku heterogenost i fenotipski kontinuum u rasponu od Gerodermije osteodysplastilke, De Barsy-jevog sindroma, pa čak i kod

pacijenta klasificiranih kao Hallermann-Streiff progeroidni sindrom (33). Također kod tri pacijenta sekvenciranjem cijelog egzoma nisam identificirao genetski uzrok bolesti, što ukazuje na postojanje drugih, još neotkrivenih genetskih uzroka segmentalnih progeroidnih sindroma koje bi se možda mogle otkriti primjenom sekvenciranja cijelog genoma (28).

Povrh toga, funkcionalne analize, prvenstveno mutacije u genima *SPRTN* i *MDM2* ukazuju da različita regulacija sličnih molekularnih puteva može voditi do sindroma sa znakovima ubrzanog/preuranjenog starenja. Naime, karakterizacija *SPRTN* mutacija pomoću staničnih modela, te modela ribice zebrice, je pokazala da mutacije uzrokuju nemogućnost ispravnog popravka DNA oštećenja, rezultirajući u izrazitoj genomskoj nestabilnosti i razvoju hepatocelularnog karcinoma (30). Suprotno tome, slična karakterizacija *MDM2* mutacija je pokazala da one uzrokuju izrazitu genomsku stabilnost, te ovi pacijenti ne razvijaju karcinome (31). Zanimljivo je da i povećana genomska nestabilnost, kod *MDM2* mutacija, kao i povećana genomska nestabilnost, kod *SPRTN* mutacija, na staničnoj razini vode do smanjene proliferacije stanica. Time ovi rezultati ukazuju da je usporavanje umnažanja i održivosti stanica kompatibilno sa razvojem znakova ubrzanog starenja na nivou organizma.

Rezultati mojih istraživanja imaju i mogući translacijski potencijal, posebno u boljem razumijevanju razvoja tumora, a eventualno čak i u razvoju njihove ciljane terapije. Sva tri pacijenta sa bialelnim mutacijama u *SPRTN* genu su razvili izrazito rano hepatocelularni karcinom. Daljnja istraživanja ovog proteina bi mogla dovesti do boljeg razumijevanja razvoja ovog tipa tumora te eventualno otkriti nove načine za terapiju istih. Također, vjerojatno nije pretjerano reći da je p53 jedna od najvažnijih molekula u polju onkologije. Moji rezultati ukazuju na potencijalno povećan rizik od nuspojava za dugotrajne sistemske terapije s MDM2-inhibitorima kod tumora s *TP53* mutacijom, za koje su već u tijeku kliničke studije, te time moguće imaju izravne kliničke implikacije.

5) PRESLIKE RADOVA KOJI SE OBJEDINJUJU U DOKTORSKOM RADU

Doktorska disertacija pripremljena je objedinjenjem triju znanstvenih radova:

1. Davor Lessel, Bruno Vaz, Swagata Halder, Paul J Lockhart, Ivana Marinovic-Terzic, Jaime Lopez-Mosqueda, Melanie Philipp, Joe C H Sim, Katherine R Smith, Judith Oehler, Elisa Cabrera, Raimundo Freire, Kate Pope, Amsha Nahid, Fiona Norris, Richard J Leventer, Martin B Delatycki, Gotthold Barbi, Simon von Ameln, Josef Högel, Marina Degoricija, Regina Fertig, Martin D Burkhalter, Kay Hofmann, Holger Thiele, Janine Altmüller, Gudrun Nürnberg, Peter Nürnberg, Melanie Bahlo, George M Martin, Cora M Aalfs, Junko Oshima, Janos Terzic, David J Amor, Ivan Dikic, Kristijan Ramadan, Christian Kubisch: *Mutations in SPRTN cause early onset hepatocellular carcinoma, genomic instability and progeroid features*. Nature Genetics 09/2014; 46(11)., DOI:10.1038/ng.3103

2. Davor Lessel, Danyi Wu, Carlos Trujillo, Thomas Ramezani, Ivana Lessel, Mohammad K. Alwasiyah, Bidisha Saha, Fuki M. Hisama, Katrin Rading, Ingrid Goebel, Petra Schütz, Günter Speit, Josef Högel, Holger Thiele, Gudrun Nürnberg, Peter Nürnberg, Matthias Hammerschmidt, Yan Zhu, David R. Tong, Chen Katz, George M. Martin, Junko Oshima, Carol Prives, Christian Kubisch: *Dysfunction of the MDM2/p53 axis is linked to premature aging*. Journal of Clinical Investigation 08/2017;, DOI:10.1172/JCI92171

3. Davor Lessel, Ayse Bilge Ozel, Susan E. Campbell, Abdelkrim Saadi, Martin F. Arlt, Keisha Melodi McSweeney, Vasilica Plaiasu, Katalin Szakszon, Anna Szőllős, Cristina Rusu, Armando J. Rojas, Jaime Lopez-Valdez, Holger Thiele, Peter Nürnberg, Deborah A. Nickerson, Michael J. Bamshad, Jun Z. Li, Christian Kubisch, Thomas W. Glover, Leslie B. Gordon: *Analyses of LMNA-negative juvenile progeroid cases confirms biallelic POLR3A mutations in Wiedemann–Rautenstrauch-like syndrome and expands the phenotypic spectrum of PYCR1 mutations*. Human Genetics 11/2018; 137(11-12)., DOI:10.1007/s00439-018-1957-1

Mutations in *SPRTN* cause early onset hepatocellular carcinoma, genomic instability and progeroid features

Davor Lessel[1,2,26], Bruno Vaz[3,26], Swagata Halder[3,4,26], Paul J Lockhart[5,6,26], Ivana Marinovic-Terzic[7,26], Jaime Lopez-Mosqueda[8,9], Melanie Philipp[10], Joe C H Sim[5], Katherine R Smith[11,12], Judith Oehler[3,4], Elisa Cabrera[13], Raimundo Freire[13], Kate Pope[5], Amsha Nahid[11], Fiona Norris[14], Richard J Leventer[6,15,16], Martin B Delatycki[5,6,17], Gotthold Barbi[1], Simon von Ameln[1], Josef Högel[1], Marina Degoricija[7], Regina Fertig[4], Martin D Burkhalter[18], Kay Hofmann[19], Holger Thiele[20], Janine Altmüller[20], Gudrun Nürnberg[20], Peter Nürnberg[20–22], Melanie Bahlo[11,23], George M Martin[24], Cora M Aalfs[25], Junko Oshima[24], Janos Terzic[7], David J Amor[5,6], Ivan Dikic[8,9], Kristijan Ramadan[3,4] & Christian Kubisch[1,2]

Age-related degenerative and malignant diseases represent major challenges for health care systems. Elucidation of the molecular mechanisms underlying carcinogenesis and age-associated pathologies is thus of growing biomedical relevance. We identified biallelic germline mutations in *SPRTN* (also called *C1orf124* or *DVC1*)[1–7] in three patients from two unrelated families. All three patients are affected by a new segmental progeroid syndrome characterized by genomic instability and susceptibility toward early onset hepatocellular carcinoma. SPRTN was recently proposed to have a function in translesional DNA synthesis and the prevention of mutagenesis[1–7]. Our *in vivo* and *in vitro* characterization of identified mutations has uncovered an essential role for SPRTN in the prevention of DNA replication stress during general DNA replication and in replication-related G2/M-checkpoint regulation. In addition to demonstrating the pathogenicity of identified *SPRTN* mutations, our findings provide a molecular explanation of how SPRTN dysfunction causes accelerated aging and susceptibility toward carcinoma.

Monogenic syndromes with highly penetrant tumor susceptibility and/or signs of premature aging affecting more than one tissue have been instrumental in identifying the genes and pathways involved in carcinogenesis and age-related diseases[8,9]. The latter are commonly defined as segmental progeroid syndromes[10] and can be caused by germline mutations in genes encoding DNA repair proteins with concomitant cancer predisposition. Examples include *WRN*, the Werner helicase gene, in Werner syndrome or *BLM*, the Bloom helicase gene, in Bloom syndrome. In addition, mutations in nuclear lamina–associated genes, for example, *LMNA* (encoding lamin A/C) in Hutchinson-Gilford syndrome or *BANF1* in Nestor-Guillermo progeria[11,12], can result in segmental progeria. Although *LMNA* mutations are also found in a few atypical cases of Werner syndrome[13], some patients with suspected Werner syndrome do not harbor mutations in any known progeria gene[14].

Here we studied three patients from two unrelated families presenting with early onset hepatocellular carcinoma (HCC), genomic instability and progeroid features. Consanguineous family A (**Fig. 1a**) of Moroccan origin was referred to the International Registry of Werner Syndrome, and the clinical characteristics of the affected boy in the family, A-IV:1, have been described previously[15]. The patient had short stature, bilateral cataracts, premature hair graying and died of HCC at the age of 17 years. Family B is a nonconsanguineous Australian family of European ancestry (**Fig. 1b**). Both affected boys, B-II:1 and B-II:4, presented similar clinical features, including

10

Figure 1 Identification of causative *SPRTN* mutations. (**a,b**) The pedigrees of families A and B. Filled and open symbols denote affected and healthy individuals, respectively; an arrow indicates the index patient, and diagonal lines indicate deceased status. The double line shows parental consanguinity, and the question mark denotes that the exact degree of consanguinity is unknown. (**c**) Axial view of magnetic resonance imaging of the liver of patient B-II:4. The green arrow indicates a 12 mm × 13 mm lesion mass with an absence of arterial phase enhancement within segment VIII of the liver that was subsequently shown to be a HCC. (**d**) Analysis of total cell extracts of patients' LCLs with SPRTN antibodies (Ab) raised against the N- or C-terminal part of the protein. (**e**) Genomic localization and protein structure of SPRTN. The genomic structure is based on the longest ORF containing five coding exons (black rectangles). The positions of the identified mutations are shown at both the gene (top) and protein (bottom) levels. The protein diagram depicts the predicted functional domains of SPRTN. aa, amino acids.

low body weight, micrognathia, triangular face, muscular atrophy, lipodystrophy, bilateral simian creases, delayed bone age and mild joint restrictions in the fingers and elbows. Although hepatitis A, B and C serologies and α-fetoprotein levels were normal in these two boys, both developed early onset HCC at age 16 and 14, respectively (**Fig. 1c**). B-II:1 died at age 18 years from complications of acute fulminant hepatic failure. The clinical characteristics of all three affected individuals are summarized and compared to those of known segmental progeroid syndromes in **Table 1**.

To identify the genetic cause of this putatively autosomal-recessive segmental progeroid disorder, we performed genome-wide linkage analysis (**Supplementary Fig. 1**) followed by exome sequencing of unrelated individuals A-IV:1 and B-II:4. Bioinformatic filtering identified *SPRTN* as the only gene with rare, biallelic mutations in the exomes of both individuals (**Supplementary Tables 1** and **2**). In A-IV:1, a 1-bp deletion at cDNA position 721 bp (c.721delA) was the only nonannotated sequence change with a severe impact on protein structure within the homozygous regions and is predicted to introduce a premature stop codon at amino acid 249 (p.Lys241AsnfsX8). B-II:4 was compound heterozygous for a c.350A>G missense alteration, resulting in the amino acid substitution p.Tyr117Cys, and a 4-bp deletion at cDNA position 717 bp (c.717_718+2delAGGT). At the cDNA level, this deletion predominantly caused intron inclusion, inducing a premature stop codon at amino acid 246 (p.Lys239LysfsX7). A very small fraction of cDNA demonstrated skipping of exon 4, resulting in a premature stop at position 161 bp (p.Val151IlefsX10) (**Supplementary Fig. 2a–c**). This finding was further supported by protein analysis, which identified a reduced amount of full-length protein and a new truncated protein (**Fig. 1d**). Sanger sequencing confirmed the mutations in all three patients (**Supplementary Fig. 2d**) and cosegregation with disease state in their families (**Supplementary Table 3**). None of these variants was present in dbSNP137 or the 1000 Genomes data. The substitution p.Tyr117Cys is located in a putative zinc metalloprotease SprT domain five amino acids upstream of Glu112, which was recently shown to be necessary for the regulation of error-prone translesional DNA synthesis (TLS)[5]. The identified truncating mutations (ΔC-ter SPRTN) lead to the loss of functionally important C terminal–located domains, including the ubiquitin-segregase p97 (VCP)[16]-interacting motif (SHP), the proliferating cell nuclear antigen interacting box (PIP) and the ubiquitin binding domain (UBZ4; **Fig. 1e**). The C-terminal part of SPRTN has an essential function at ultraviolet (UV)-induced stalled replication forks by the removal of DNA polymerase η in a p97-dependent manner after the completion of TLS[2,3]. Taken together, these genetic findings have already provided strong evidence for the pathogenicity of the identified mutations. The analysis of 48 additional patients with
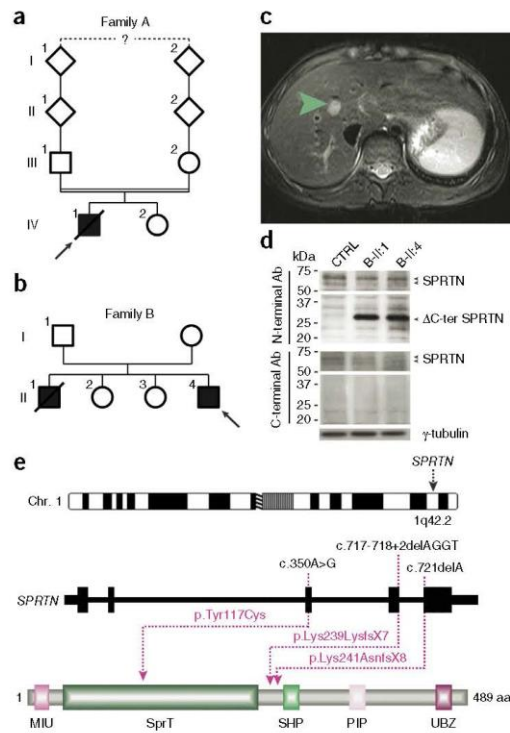
suspected Werner syndrome but without mutations in *WRN* or *LMNA*[14] revealed no other *SPRTN* mutation, providing further evidence of extended locus heterogeneity for segmental progeroid syndromes.

We next performed morphological and immunohistochemical analyses of patients' liver tumor biopsies. Staining with a C-terminal SPRTN antibody (**Fig. 2a**) showed the absence of the C-terminal part of SPRTN in A-IV:1, thus confirming the truncation of the mutated protein in A-IV:1 *in vivo*. We observed focal accumulations of anti-SPRTN immunoreactive material in B-II:1 and B-II:4, as well as in idiopathic HCC. *In vitro* analysis of focal nuclear accumulation of ectopically expressed wild-type (WT) SPRTN and mutant SPRTN from patients additionally supported the *in vivo* finding and disclosed that WT and p.Tyr117Cys SPRTN are able to form nuclear foci, but ΔC-ter SPRTN is not (**Fig. 2b**). Analyses of cancer biomarkers revealed strong focal accumulations of both γ-H2AX (H2AFX) and 53BP1 (TP53BP1) (**Fig. 2a**). In addition, and opposite to what we observed in patient primary cell lines (**Fig. 3a–c**), Ki-67 (MKI67) staining in the biopsies of A-IV:1, B-II:1 and B-II:4 indicated a high proliferative index compared to healthy liver or idiopathic HCC (**Fig. 2a**). These data suggest a relatively aggressive neoplasm[17,18].

We next tested whether the cellular phenotypes described previously in A-IV:1, namely chromosomal instability with concomitant sensitivity toward genotoxic agents and severe proliferation defects[15], were also present in primary cell lines from B-II:1 and B-II:4. Indeed, we found increased chromosomal instability in peripheral blood (**Supplementary Fig. 3**) and lymphoblastoid cell lines (LCLs) from the patients, which was enhanced after treatment with mitomycin C (MMC) and 4-nitroquinoline 1-oxide (4-NQO) (**Fig. 3d**). In patient

Table 1 Clinical and cellular findings in Werner syndrome, atypical Werner syndrome and patients described here

Clinical findings	Werner syndrome	Atypical Werner syndrome	A-IV:1	B-II:1	B-II:4
Short stature	+	+	+	−	−
Low body weight	+	+	+	+	+
Dermatological abnormalities	+	+	−	+	−
Cataracts	+	−	+	−	−
Sparse hair	+	+	−	−	−
Premature hair graying	+	+	+	−	−
Diabetes mellitus	+	+	−	−	−
Hypogonadism	+	−	−	−	−
Osteoporosis	+	−	−	−	−
General skeletal abnormalities	−	−	+	−	−
Atherosclerosis	+	+	−	−	−
Neoplasms	+	−	+	+	+
Hepatocellular carcinoma	Rare	−	+	+	+
Micrognathia	-	+	+	+	+
Lipodystrophy	+	+	?	+	+
Muscular atrophy	+	+	?	+	+
Attention deficit	−	−	−	+	+
Cellular findings					
Chromosomal instability	+	?	+	+	+
Sensitivity to genotoxic agents	+	?	+	+	+
Mutated gene	WRN	LMNA	SPRTN	SPRTN	SPRTN

Atypical Werner syndrome includes cases with *LMNA* mutations. +, present in most patients; −, not present in most patients; ?, not known.

fibroblasts, we observed multiple and variable aberrations that were clonal in nature (**Supplementary Fig. 4**), which is compatible with variegated translocation mosaicism, a phenomenon previously described in Werner syndrome cells[19]. Measurement of a proliferation

index revealed a severe growth defect in cultured B-II:1 fibroblasts (**Fig. 3a–c**), thus confirming prior findings in cells from A-IV:1 (ref. 15). Further, short interfering RNA (siRNA)-mediated depletion of SPRTN in HEK293T and U2OS human cell lines also caused chromosomal instability and severe proliferation defects, respectively (**Supplementary Figs. 5** and **6**).

To assess the consequences of patient mutations in an *in vivo* complementation assay, we performed morpholino-mediated down-regulation of the *SPRTN* ortholog in zebrafish (*LOC101886162*, called here *sprtn*). *sprtn* silencing, verified by a GFP reporter assay (**Supplementary Fig. 7a**), led to a substantial increase of γ-H2AX foci (**Supplementary Fig. 7b,c**), indicating an evolutionarily conserved functional role of SPRTN in the DNA damage response. When injecting higher doses of morpholino, embryos displayed phenotypically normal development until the shield stage at 6 h post fertilization (hpf), a stage when maternal gene products are degraded[20]. At 10 hpf, however, embryos exhibited either early mortality or were delayed in development up to 4 h. This growth retardation phenotype is compatible with the proliferation defects observed in patients' fibroblasts and the relative growth deficits observed in patients. This phenotype was partially rescued by co-injection of WT human *SPRTN* mRNA but not by equimolar amounts of mRNA from *SPRTN* harboring the identified mutations (**Fig. 3e,f**), thus further confirming their pathogenicity.

The lack of sun sensitivity and the presence of severe chromosomal breakage, proliferation defects and early onset HCC in patients indicated a more complex role of SPRTN in the maintenance of genome stability than solely TLS, as was proposed recently[1–7]. Defects in DNA replication have been proposed to be a major cause of the variegated translocation mosaicism and genomic instability that consequently lead to aging and cancer[21–23]. To test for a role of SPRTN in DNA replication, we analyzed the progression of replication forks directly by
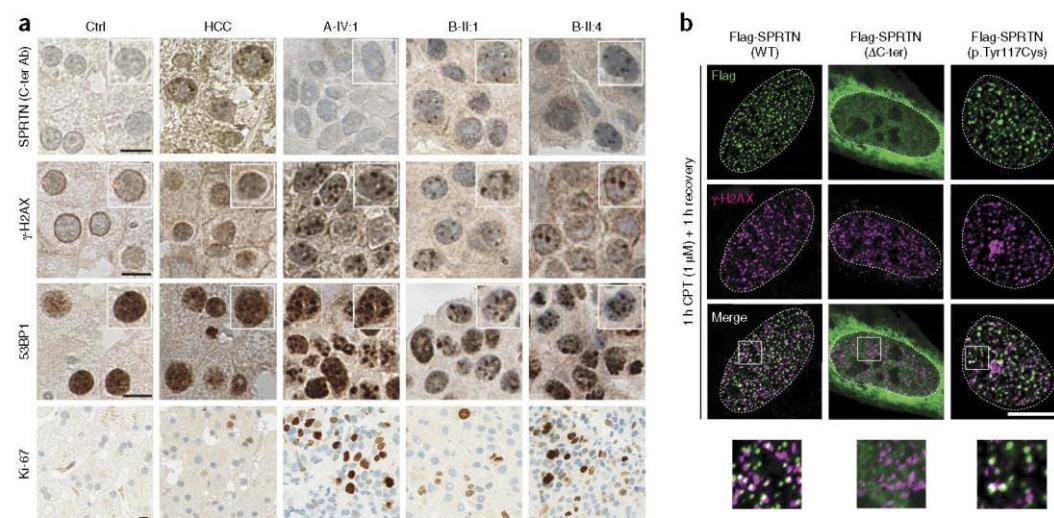
Figure 2 Severe DNA damage in hepatocellular carcinoma biopsies and focal nuclear accumulation of SPRTN. (**a**) Histological and immunohistochemical analyses of human liver biopsies from a healthy control (Ctrl), a patient with idiopathic, non–viral caused HCC and the HCC of patients with *SPRTN* mutations (A-IV:1, B-II:1 and B-II:4). The samples were stained with antibody raised against the C-terminal part of SPRTN (C-ter Ab) or with antibodies against γ-H2AX, 53BP1 or Ki-67. The insets in the top three rows are at 1.25× magnification. (**b**) U2OS cells were transiently transfected with Flag-tagged WT or mutant SPRTN and challenged with 1 μM of CPT to induce replication-related DSBs and thus mimic the DNA damage observed in patients' livers. The images at the bottom of **b** are 3× magnified versions of the boxed areas in the merged images above. Scale bars, 10 μm (**a,b**).

12

Figure 3 Genomic instability and cell proliferation defects. (a) A growth curve of control and patient primary skin fibroblasts. The data are from three independent experiments. (b) Primary skin fibroblasts stained with the proliferation marker Ki-67. Scale bars, 10 μm. DAPI, 4′,6-diamidino-2-phenylindole. (c) Quantification of the data in b. The data are from three independent experiments with greater than 100 cells scored per condition per experiment. (d) Chromosomal aberrations in patients' LCLs under untreated conditions or the following genotoxic conditions: 40 ng/ml of MMC or 200 ng/ml of 4-NQO. The data are from three independent experiments with 33 analyzed metaphase cells per condition per experiment. The data in a, c and d were analyzed with unpaired t-test and are presented as the mean ± s.e.m. (e) Morpholino oligonucleotide (MO)-mediated gene downregulation of Sprtn in zebrafish at 10 hpf and a rescue experiment with human WT SPRTN or SPRTN harboring the two patient mutations. Ctrl MO denotes embryos injected with control MO, ATG MO denotes embryos injected with SPRTN MO targeting the start codon, and splice MO denotes embryos injected with a splice-site MO. The bar graph summarizes analyses in more than 100 embryos in three independent experiments showing the distribution of phenotypes observed after injections with 17.6 ng of MO and co-injections of 100 pg of SPRTN mRNA. P values in e were calculated using the χ^2 test. *$P < 0.01$, **$P < 0.001$, ***$P < 0.0001$ (a,c–e). (f) Western blot analysis of the experiment shown in e. Sprtn, endogenous zebrafish protein; SPRTN, ectopically expressed human protein.

DNA fiber assay (**Fig. 4a**), the clearest method to unambiguously characterize the DNA replication machinery[24]. The speed of DNA replication was significantly but only mildly affected in patients' LCLs under unchallenged conditions (**Fig. 4b**), but increased levels of stalled forks (**Fig. 4c**) and newly fired origins (**Fig. 4d**) indicated DNA replication stress as the cause of DNA damage in these patients[25]. When we treated LCLs with a low dose of aphidicolin (APH), mimicking the physiological barriers the DNA replication machinery approaches during DNA synthesis[26], patients' cells showed a typical signature of DNA replication stress, namely shorter replication forks than in control cells (**Fig. 4e,f**). This observation is comparable to cellular findings in Werner and Bloom syndromes[27,28]. Moreover, B-II:1 fibroblasts showed markedly increased numbers of double-strand breaks (DSBs) in S-phase cells (**Supplementary Fig. 8**). To further confirm that mutations in *SPRTN* are the cause of the DNA replication defect, we transfected patients' cells with WT SPRTN, which almost completely corrected the replication defect (**Fig. 4g** and **Supplementary Fig. 9a**) and restored cellular proliferation (**Supplementary Fig. 9b,c**). siRNA-mediated SPRTN depletion severely affected the progression of DNA replication and induced an increased number of stalled forks, newly fired origins and formation of DSBs in the S phase of the cell cycle (**Supplementary Fig. 10**), providing further evidence of the role of SPRTN in general DNA replication. Notably, depletion of DNA polymerase η in patients' cells or in SPRTN-depleted U2OS cells did not complement the DNA replication phenotype (**Supplementary Fig. 11**), suggesting that DNA polymerase η is not the main substrate, as reported previously[2,3].

To evaluate how replication-related DNA damage is transferred to mitosis and may thus contribute to chromosomal instability, we measured the ability of patients' cells to activate the G2/M checkpoint, the main guardian of genome stability after DNA replication stress[29]. We exposed patients' LCLs to different genotoxic agents and measured the arrival of cells to mitosis by flow cytometry (**Fig. 4h–j** and **Supplementary Figs. 12** and **13**). We observed a severe G2/M-checkpoint defect in cells from B-II:1 and B-II:4

after treatment with genotoxic agents that interfere with DNA replication, such as camptothecin (CPT) (**Fig. 4h–j**), a topoisomerase I inhibitor that causes replication-related DSBs, or UV radiation (**Supplementary Fig. 13**). Notably, the G2/M checkpoint was completely functional when we created random and non–replication related DSBs using ionizing radiation (**Supplementary Fig. 13**). The hypersensitivity of patient cells to replication-related genotoxic agents but not to ionizing radiation (**Supplementary Fig. 14**) correlates with G2/M leakage.

To further assess the role of patients' mutations in DNA replication and G2/M-checkpoint regulation, we tested their function in U2OS cells that we depleted of endogenous SPRTN using siRNA (**Fig. 5** and **Supplementary Fig. 15**). Ectopic expression of WT SPRTN restored DNA replication and G2/M-checkpoint defects. The expression of ΔC-ter SPRTN was also able to restore the progression of the DNA replication fork but to a much lesser extent then WT SPRTN, suggesting that this mutant is defective in proper DNA synthesis (**Fig. 5b**). The difference in efficacy was even more pronounced when we exposed cells to mild replication stress (APH treatment; **Fig. 5c**), further supporting the function of the C-terminal part of SPRTN in TLS. Notably, the cells ectopically expressing p.Tyr117Cys SPRTN were completely unable to restore DNA replication fork progression, suggesting the essential role of the SprT domain in general DNA replication. We obtained similar results in HEK293 cells (data not shown). In contrast to DNA replication, cells expressing either of the patient mutations or coexpressing both mutations were equally defective in activation of the G2/M checkpoint after exposure to UV radiation or CPT treatment (**Fig. 5d** and data not shown), indicating the communal function of the SprT domain and the C-terminal part of SPRTN in the regulation of the G2/M-checkpoint response. Taken together, these data demonstrate that SPRTN dysfunction leads to sustained DNA replication stress and consequent replication-related DNA damage, especially DSBs, which are transferred to the next cell generation because of a leakage of the G2/M checkpoint and, consequently, lead to cancer or aging.
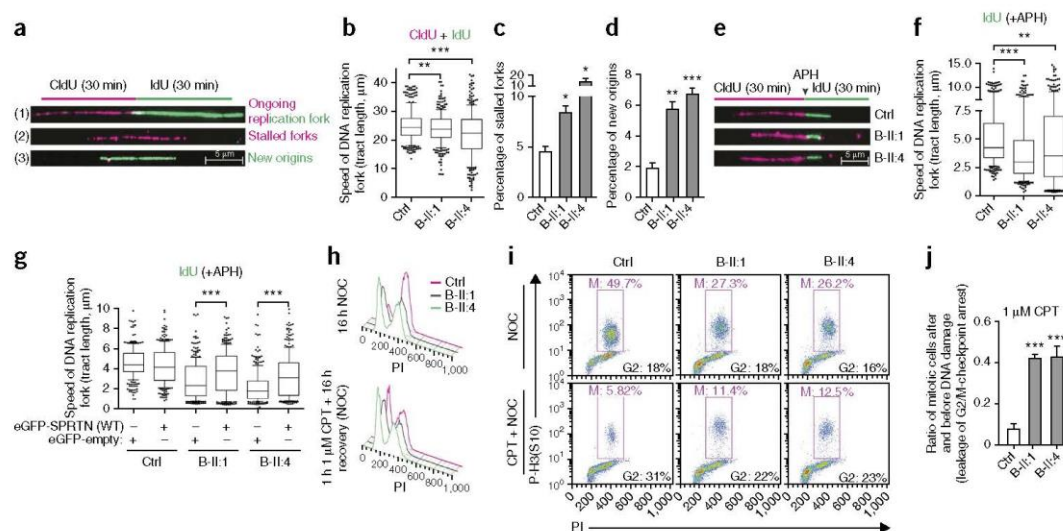
13

Figure 4 DNA replication stress and leakage of the G2/M cell cycle checkpoint as the origin of genomic instability. (**a**) Schematic representation of a single DNA replication fork analysis by DNA fiber assay and its outcome ((1)–(3)). (**b**–**d**) DNA replication forks, as described in **a**, were analyzed in LCLs and quantified for velocity (**b**), percentage of stalled forks (**c**) and percentage of newly fired replication origins (**d**). $n = 3$; 100 CldU (5-chloro-2′-deoxyuridine) and 100 IdU (5-iodo-2′-deoxyuridine) symmetrical tracts were individually quantified, counted and are presented as total tract length (**b**), or 400 forks were randomly scored per condition per experiments (**c**,**d**). (**e**) Representative replication forks analyzed in LCLs when the incorporation of IdU was in the presence of a low dose of APH (0.1 μM). (**f**) The speed of replication forks under mild genotoxic conditions (IdU only). $n = 3$; 100 DNA fibers analyzed per experiment per condition. (**g**) LCLs were transfected with WT SPRTN, and the speed of replication fork was measured under mild genotoxic conditions, as in **e**. $n = 2$; 100 DNA fibers analyzed per experiment per condition. (**h**) Cell cycle profile of LCLs. NOC, nocodazole. PI, propidium iodide. (**i**) Mitotic (red triangle) LCLs without and with CPT treatment analyzed in the presence of NOC. (**j**) Quantification of **i**; $n = 3$. Data in **b**, **f** and **g** are shown as the median (bar) with the 25th–75th percentile range (box) and the 10th–90th percentile range (whiskers). Data in **c**, **d** and **j** are shown as the mean ± s.e.m. Data in **b**–**d**, **f**, **g** and **j** were analyzed with unpaired two-tailed t-test. $*P < 0.0$, $**P < 0.001$, $***P < 0.0001$.

Studying the genetic and cellular basis of monogenic segmental progeroid and tumor susceptibility syndromes has been a meaningful approach in unraveling the molecular mechanisms and pathways involved in the regulation of cancer development and common

diseases of the elderly[8]. HCC, although rarely occurring before the age of 40 years[30], is the fifth most common malignancy and the third leading cause of cancer-related death worldwide[31]. Although major risk factors for HCC are well known, including hepatitis B and C

Figure 5 Characterization of patients' mutations in DNA replication and G2/M-checkpoint regulation. (**a**) Western blot analysis of U2OS cells depleted of endogenous SPRTN by siRNA (siSPRTN#1) and simultaneously expressing siRNA-resistant WT SPRTN, ΔC-ter SPRTN or p.Tyr117Cys SPRTN or coexpressing of ΔC-ter SPRTN and p.Tyr117Cys SPRTN. (**b**,**c**) U2OS cells, as in **a**, labeled with CldU for 30 min (unchallenged conditions; **b**) or with IdU and treated with APH for 30 min (mild genotoxic conditions; **c**) were analyzed by DNA fiber assay. 1 μm of DNA tract length corresponds to 2.6 kb of newly synthesized DNA[32]. $n = 3$; more than 100 DNA fibers analyzed per experiment and per condition. (**d**) U2OS cells, as in **a**, were analyzed for the efficacy of the G2/M checkpoint after treatment with UV radiation, as described in **Figure 4**. The graph summarizes three independent experiments. The data in **b** and **c** are presented as the median (bar) with the 25th–75th percentile range (box) and the 10th–90th percentile range (whiskers). Data in **d** are shown as a bar graph with the mean ± s.e.m. Data in **b**–**d** were analyzed with unpaired two-tailed t-test. $*P < 0.05$, $**P < 0.001$, $***P < 0.0001$. NS, no significant difference between the groups.

14
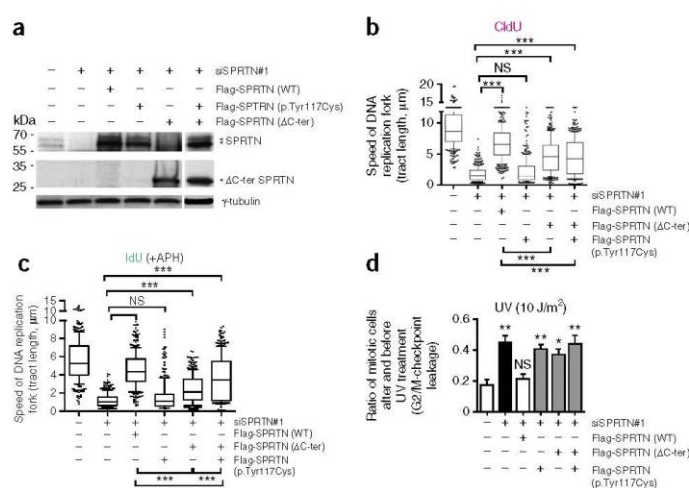
infection and alcohol abuse, the molecular pathogenesis of HCC remains largely elusive. All three patients presented here—in addition to showing signs of accelerated aging in selected tissues—developed early onset HCC, identifying *SPRTN* as a monogenic and apparently highly penetrant susceptibility gene for HCC. Consequently, our findings suggest *SPRTN* as the subject of future studies of hepatocarcinogenesis and therapy.

URLs. The International Registry of Werner Syndrome, http://www.wernersyndrome.org/registry/registry.html.

METHODS
Methods and any associated references are available in the online version of the paper.

Accession codes. NCBI reference sequences: UniGene: NM_032018, protein: NP_114407.3. Microarray probes: NM_032018.4. UniProt: Q9H040. GenBank: AL512744. *SPRTN* mutations: NM_032018.5 (c.721delA, ss1387933564, rs527236212; c.350A>G, ss1387933565, rs527236213; c.717_718+2delAGGT, ss1387933572, rs587593493).

Note: Any Supplementary Information and Source Data files are available in the online version of the paper.

Reprints and permissions information is available online at http://www.nature.com/reprints/index.html.

1. Centore, R.C., Yazinski, S.A., Tse, A. & Zou, L. Spartan/C1orf124, a reader of PCNA ubiquitylation and a regulator of UV-induced DNA damage response. *Mol. Cell* **46**, 625–635 (2012).
2. Davis, E.J. *et al.* DVC1 (C1orf124) recruits the p97 protein segregase to sites of DNA damage. *Nat. Struct. Mol. Biol.* **19**, 1093–1100 (2012).
3. Mosbech, A. *et al.* DVC1 (C1orf124) is a DNA damage–targeting p97 adaptor that promotes ubiquitin-dependent responses to replication blocks. *Nat. Struct. Mol. Biol.* **19**, 1084–1092 (2012).
4. Juhasz, S. *et al.* Characterization of human Spartan/C1orf124, an ubiquitin-PCNA interacting regulator of DNA damage tolerance. *Nucleic Acids Res.* **40**, 10795–10808 (2012).
5. Kim, M.S. *et al.* Regulation of error-prone translesion synthesis by Spartan/C1orf124. *Nucleic Acids Res.* **41**, 1661–1668 (2013).
6. Machida, Y., Kim, M.S. & Machida, Y.J. Spartan/C1orf124 is important to prevent UV-induced mutagenesis. *Cell Cycle* **11**, 3395–3402 (2012).
7. Ghosal, G., Leung, J.W., Nair, B.C., Fong, K.W. & Chen, J. Proliferating cell nuclear antigen (PCNA)-binding protein C1orf124 is a regulator of translesion synthesis. *J. Biol. Chem.* **287**, 34225–34233 (2012).
8. Burtner, C.R. & Kennedy, B.K. Progeria syndromes and ageing: what is the connection? *Nat. Rev. Mol. Cell Biol.* **11**, 567–578 (2010).
9. Fletcher, O. & Houlston, R.S. Architecture of inherited susceptibility to common cancer. *Nat. Rev. Cancer* **10**, 353–361 (2010).
10. Martin, G.M. Genetic syndromes in man with potential relevance to the pathobiology of aging. *Birth Defects Orig. Artic. Ser.* **14**, 5–39 (1978).
11. Navarro, C.L., Cau, P. & Levy, N. Molecular bases of progeroid syndromes. *Hum. Mol. Genet.* **15**, R151–R161 (2006).
12. Puente, X.S. *et al.* Exome sequencing and functional analysis identifies BANF1 mutation as the cause of a hereditary progeroid syndrome. *Am. J. Hum. Genet.* **88**, 650–656 (2011).
13. Chen, L. *et al.* LMNA mutations in atypical Werner's syndrome. *Lancet* **362**, 440–445 (2003).
14. Oshima, J. & Hisama, F.M. Search and insights into novel genetic alterations leading to classical and atypical Werner syndrome. *Gerontology* **60**, 239–246 (2014).
15. Ruijs, M.W. *et al.* Atypical progeroid syndrome: an unknown helicase gene defect? *Am. J. Med. Genet. A.* **116A**, 295–299 (2003).
16. Vaz, B., Halder, S. & Ramadan, K. Role of p97/VCP (Cdc48) in genome stability. *Front. Genet.* **4**, 60 (2013).
17. King, K.L. *et al.* Ki-67 expression as a prognostic marker in patients with hepatocellular carcinoma. *J. Gastroenterol. Hepatol.* **13**, 273–279 (1998).
18. Nowsheen, S., Aziz, K., Panayiotidis, M.I. & Georgakilas, A.G. Molecular markers for cancer prognosis and treatment: have we struck gold? *Cancer Lett.* **327**, 142–152 (2012).
19. Hoehn, H. *et al.* Variegated translocation mosaicism in human skin fibroblast cultures. *Cytogenet. Cell Genet.* **15**, 282–298 (1975).
20. Aanes, H. *et al.* Zebrafish mRNA sequencing deciphers novelties in transcriptome dynamics during maternal to zygotic transition. *Genome Res.* **21**, 1328–1338 (2011).
21. Shen, J.C. & Loeb, L.A. The Werner syndrome gene: the molecular basis of RecQ helicase–deficiency diseases. *Trends Genet.* **16**, 213–220 (2000).
22. Venkatesan, R.N. *et al.* Mutation at the polymerase active site of mouse DNA polymerase δ increases genomic instability and accelerates tumorigenesis. *Mol. Cell. Biol.* **27**, 7669–7682 (2007).
23. Branzei, D. & Foiani, M. Maintaining genome stability at the replication fork. *Nat. Rev. Mol. Cell Biol.* **11**, 208–219 (2010).
24. Zeman, M.K. & Cimprich, K.A. Causes and consequences of replication stress. *Nat. Cell Biol.* **16**, 2–9 (2014).
25. Costantino, L. *et al.* Break-induced replication repair of damaged forks induces genomic duplications in human cells. *Science* **343**, 88–91 (2014).
26. Lukas, C. *et al.* 53BP1 nuclear bodies form around DNA lesions generated by mitotic transmission of chromosomes under replication stress. *Nat. Cell Biol.* **13**, 243–253 (2011).
27. Sidorova, J.M., Li, N., Folch, A. & Monnat, R.J. Jr. The RecQ helicase WRN is required for normal replication fork progression after DNA damage or replication fork arrest. *Cell Cycle* **7**, 796–807 (2008).
28. Davies, S.L., North, P.S. & Hickson, I.D. Role for BLM in replication-fork restart and suppression of origin firing after replicative stress. *Nat. Struct. Mol. Biol.* **14**, 677–679 (2007).
29. Löbrich, M. & Jeggo, P.A. The impact of a negligent G2/M checkpoint on genomic instability and cancer induction. *Nat. Rev. Cancer* **7**, 861–869 (2007).
30. El-Serag, H.B. Hepatocellular carcinoma. *N. Engl. J. Med.* **365**, 1118–1127 (2011).
31. Caldwell, S. & Park, S.H. The epidemiology of hepatocellular cancer: from the perspectives of public health problem to tumor biology. *J. Gastroenterol.* **44** (suppl. 19), 96–101 (2009).
32. Wilsker, D., Petermann, E., Helleday, T. & Bunz, F. Essential function of Chk1 can be uncoupled from DNA damage checkpoint and replication control. *Proc. Natl. Acad. Sci. USA* **105**, 20752–20757 (2008).

15

ONLINE METHODS

Ethical approval and study procedures. The International Registry of Werner Syndrome has been recruiting patients suspected of having Werner syndrome since 1988. Studies of family A and B were approved by the University of Washington Institutional Review Board and the Human Research Ethics Committee of the Royal Children's Hospital, Melbourne, Australia, respectively. DNA samples from whole blood were isolated by standard procedures after written informed consent of participating individuals.

Linkage analysis in family A. Linkage analysis was performed using Genome-Wide Human SNP Array 6.0. (Affymetrix, Inc., Santa Clara, CA, USA). Data handling, evaluation and statistical analyses have been described in detail before[33].

Linkage analysis in family B. All individuals in pedigree B were genotyped using Illumina Human610-Quad BeadChips (USA) at the Australian Genome Research Facility, Melbourne. Genotypes were called using the GenCall algorithm implemented in Illumina's BeadStudio package. The LINKDATAGEN script[34] was used to select a subset of 11,913 SNP markers for analysis. These markers were chosen to be in approximate linkage equilibrium (spaced at least 0.15 cM apart) and to have high heterozygosity in the HapMap population of Utah residents with ancestry from northern and western Europe (CEU). Parametric linkage analysis was performed by MERLIN[35] under a fully penetrant recessive inheritance model with a 0% phenocopy rate and a disease allele frequency of 0.00001. Allele frequencies from CEU were used.

Estimation of inbreeding coefficients in family B. FEstim[36] was used to estimate genomic inbreeding coefficients for the genotyped members of family B. A subset of 11,374 high-heterozygosity markers in approximate linkage equilibrium were selected for analysis using LINKDATAGEN. FEstim was run in an independent model with starting values $F = 0.05$ and $A = 0.05$. All inbreeding coefficients were estimated to be 0.000, indicating no evidence of inbreeding.

Candidate gene sequencing. For candidate gene analysis, we designed intronic primers to PCR amplify coding exons and the respective exon-intron boundaries by using genomic DNA of the affected individual. Primer pairs for the amplification of the five *SPRTN* coding exons and their approximately 50 bp of flanking intronic sequences (RefSeq accession NM_032018.4) are available on request. PCR products were sequenced on an ABI 3730 DNA Analyzer with BigDye chemistry v3.1 (Applied Biosystems). Sequence traces were assembled, aligned and analyzed with SeqMan software (DNASTAR Lasergene). Cosegregation of the mutations in families A and B was tested by sequencing the PCR product of exon 5, or of exons 3 and 4, respectively, amplified from genomic DNA of all participating family members.

Exome sequencing in A-IV:1. We sequenced the exome of the proband on two lanes of an Illumina GAIIx Sequencer using a single-read 150-bp protocol after enrichment of exonic and splice-site sequences with the Agilent SureSelect Human All Exon 50 Mb kit. We mapped >194 million reads to the hg19 human reference genome. Approximately 89% of target sequences were covered at least 10-fold and 83% were covered at least 30-fold, with a mean coverage of about 112×. Data analysis of filter-passed reads was performed with the in-house pipeline V1.3 using BWA-short in combination with SAMtools pileup 0.1.7 for the detection of SNPs and short insertions and deletions (indels). In-house–developed scripts were applied to detect protein changes, affected splice sites and overlaps to known variations, with filtering against dbSNP build 137, the 1000 Genomes Project data build February 2012 and our in-house database of exome variants (with data from >200 exomes of individuals affected by different disorders). We focused our analysis on rare missense, nonsense, frameshift and splice-site mutations. The criteria for a variation to be taken into account were as follows: >6 reads, phred scaled quality score >15, population allele frequency <1%, <10 times seen in our in-house database and >15% of the reads supporting the allele.

Exome sequencing in B-II:4. The exome of the surviving affected male B-II:4 was sequenced by Axeq Technologies (Korea) on three lanes of an Illumina HiSeq sequencer using a paired-end 100-bp read protocol after exome capture with the Illumina TruSeq capture array. Novoalign (V2.08.03) alignment reads mapped 57,905,140 reads uniquely to the hg19 reference genome. Presumed PCR and optical duplicates were removed using Picard 1.65, and local realignment was performed using RealignerTargetCreator and IndelRealigner walkers from the Genome Analysis Toolkit (GATK)[37,38]. Greater than 80% of target sequences were covered at least tenfold, and the median coverage of targeted bases was 40×. Single-nucleotide variants and small indel variants were detected and genotyped using the UnifiedGenotyper walker from GATK version v2.3-3-g4706074. Variants were annotated using ANNOVAR[39] against the RefSeq gene annotation; dbSNP build 137; 69 genomes from Complete Genomics[40]; 1,092 genomes from the 1000 Genomes project, February 2012 release; 6,503 European and African American ancestry exomes from the National Heart, Lung, and Blood Institute Toolkit (NHLBI) Exome Sequencing Project (ESP6500, https://esp.gs.washington.edu/drupal/); and an in-house database of 131 exomes of various ethnicities. Read-backed phasing was performed using HapCUT[41]. Variants located within the 33 linkage peaks were extracted and initially filtered for quality (phred scaled quality ≥13) and rarity (alternate allele frequency of ≤1% in the 1000 Genomes and NHLBI ESP6500 data sets and ≤4% in the Complete Genomics 69 and in-house data sets). We focused our analysis on rare homozygous or compound heterozygous variants predicted to affect protein sequence or splicing. Pairs of heterozygous variants located in the same gene that were inferred to be *in cis* phase by HapCUT[41] were eliminated.

RT-PCR analysis. RT-PCR sequencing was done as described previously[42,43]. To distinguish between two *SPRTN* isoforms, we performed two RT-PCR reactions. Primer sequences used for reaction A to amplify the canonical 489-aa isoform 1 of *SPRTN* spanning exons 2 through 5 were SPRTN-2F and SPRTN-5R, with an expected WT size of 1,205 bp. Primer sequences used for reaction B to amplify the 250-aa isoform 2 of *SPRTN* spanning exons 2 through 4 were SPRTN-2F and intronic SPRTN-4r, with an expected WT size of 640 bp.

DNA fiber assay. The DNA fiber assay was performed as described previously[44]. Briefly, asynchronous LCL, U2OS or HEK293 cells were labeled with 30 μM of CldU for 30 min, washed three times with warm PBS and then labeled with 250 μM of IdU for an additional 30 min. The reaction was terminated by treating the cells with ice-cold PBS. Cells were lysed, and DNA fibers were spread onto glass slides, fixed with methanol and acetic acid, denatured with HCl, blocked with 2% BSA and stained with anti-rat and anti-mouse 5-bromo-2′-deoxyuridine (BrdU) that specifically recognize either CldU (Sigma, C6891) or IdU (Sigma, 17125). Anti-rat Cy3 (dilution 1:300, Jackson ImmunoResearch, 712-116-153) and anti-mouse Alexa-488 (dilution 1:300, Molecular Probes, A11001) were used as the respective secondary antibodies. Microscopy was done using a Leica DMRB microscope with a DFC360FX camera. The lengths of the CldU- and IdU-labeled tracts were measured by ImageJ software. Statistical analysis was done by GraphPad Prism software using unpaired *t*-test. For the DNA fiber assay under genotoxic stress, the second nucleotide (IdU) was incubated in the presence of 0.1 μM APH.

Flow cytometry and G2/M-checkpoint assay. These analyses were performed as described previously[45]. In brief, cells were harvested, washed with PBS and subsequently fixed in 3.6% formaldehyde at room temperature for 15 min. After washing, the cells were permeabilized and blocked with 1% FBS and 0.1% saponin in PBS for 30 min. For 5-ethynyl-2′-deoxyuridine (EdU) analysis, cells were incubated with 10 μM EdU before harvesting. EdU was detected with a Click-iT EdU Cell Proliferation Assay kit (Invitrogen, C10632). Alexa 647 (3458)– or Alexa 488 (9708)–conjugated anti–phosphorylated histone H3 (Ser10) (mitotic marker) was used (dilution 1:100, Cell Signaling). Mitotic index was determined as the ratio between the numbers of mitotic cells in the presence of nocodazole (400 nM for 16 h) after UV treatment compared to those in untreated cells. DNA content was analyzed by DAPI. Cells were analyzed on a Beckman Coulter CyAn ADP Analyzer. A minimum of 10,000 events were counted.

Growth assay. 50,000 primary skin fibroblast or U2OS cells were seeded at day 0. Every 24 h, cells were washed, trypsinized, resuspended in 1 ml medium (DMEM, Sigma, D6429) and counted (TC10 automated cell counter, Bio-Rad).

Histology. Human liver biopsy specimens were obtained from University Hospital Zürich, Academic Medical Centre Amsterdam and Royal Children's Hospital Parkville. Biopsy specimens were registered in respective biobanks and kept anonymous. The study protocol was in accordance with the ethical guidelines of the Helsinki declaration. Liver samples were prepared from paraffin blocks according to standard histological protocols and hemalaun-eosin stained, or immunohistochemical staining was performed using Leica Bond automated staining system.

Immunofluorescence studies. Cells were grown on glass coverslips, fixed with 4% formaldehyde, permeabilized with 0.2% Triton X-100, blocked with 5% BSA in PBS and immunostained with the respective antibodies. Images of immuno-stained cells were taken with an epifluorescent microscope (Olympus BX51) and acquired with a charge-coupled device (CCD) camera (Orca AG), a Zeiss LSM 510 META laser scanning microscope or an SP2 Leica confocal microscope.

Antibodies. The following antibodies were used in this study: anti-SPRTN (rabbit, polyclonal) raised against the N-terminal part (1–240 aa) of SPRTN (dilution 1:1,000, home made); anti-SPRTN raised against the C-terminal part of SPRTN (dilution 1:1,000, Atlas, HPA 025073); anti–DNA polymerase η (dilution 1:1,000, Abcam, Ab17725); anti–phosphorylated γ-H2AX (Ser139) (dilution 1:300, Millipore, 05-636); anti-zebrafish γ-H2AX (dilution 1:1,000, gift of J. Amatruda); anti-rabbit 53BP1 (dilution 1:200, Santa Cruz, sc-22760); anti–Ki-67 (dilution 1:200, Millipore, MAB 4190); anti-rat BrdU (dilution 1:500, Abcam, 6326); anti-mouse BrdU (dilution 1:100, Becton Dickinson, 347850); anti-mouse Alexa Flour 488 (dilution 1:300, Invitrogen, A21202), anti-mouse Alexa Flour 594 (dilution 1:300, Invitrogen, A11020); anti-mouse horseradish peroxidase (HRP) (dilution 1:10,000, Sigma, A2304); and anti-rabbit HRP (1:10,000, Sigma, A0545).

Cell lines. Primary skin fibroblasts, Epstein-Barr virus (EBV)-transformed LCLs, U2OS and HEK293T cells were used in this study. For stable transfected GFP-SPRTN (WT) or GFP–empty vector control or patient LCLs, cells were transfected by electroporation as indicated below and selected in a medium containing G418/Geneticin (Gibco, 10131-027).

DNA primers and siRNA sequences. The DNA primers and siRNA sequences used are listed in **Supplementary Tables 4** and **5**.

Plasmids. The I.M.A.G.E. full-length SPRTN cDNA clone (IRATp970E1156D, ImaGenes) was cloned into pFlag–CMV-1 (Sigma), peGFP-C1 (Clontech) or pcDNA3.1 (Invitrogen). Mutants were cloned using PCR amplification and restriction enzyme digestion and recombination. Site-directed mutagenesis was performed by PCR to introduce the desired mutations. The correctness of the DNA sequence was verified by sequencing.

Plasmid transfection. U2OS cells were transiently transfected with Lipofectamine 2000 (Life Technology), and primary skin fibroblasts and LCLs were transfected by electroporation (Amaxa Nucleofactor Technology, Lonza) following the manufacturer's instructions.

siRNA transfection. siRNA depletion experiments in mammalian cells were conducted using Lipofectamine RNAiMax (Invitrogen) according to the manufacturer's instructions. A final concentration of 20 nM siRNA oligonucleotides was used. siRNA-transfected cells were analyzed 48 or 72 h after transfections.

Chromosome analysis. For chromosome analysis, primary skin fibroblasts, LCLs and siRNA-transfected HEK293T cells were incubated with 40 ng/ml MMC or 200 ng/ml 4-NQO or left untreated for an additional 24 h. Metaphase spreads and G banding were prepared using standard procedures, analyzed using an Axio imaging 2 microscope (Zeiss, Jena, Germany) and captured using Ikaros software (Metasystems, Altlussheim, Germany). 100 metaphase spreads were scored for chromosomal aberrations in three independent experiments. Based on 100 cells (untreated or treated with MMC or 4-NQO), the frequencies of aberrant cells were compared between LCLs from a healthy individual (AG1010) and LCLs of both affected individuals or between SPRTN siRNA treatment and a nonspecific siRNA using Fisher's exact test, unless

otherwise stated. The numbers of breaks per cell were contrasted by two-sample Poisson tests, where P values were approximated using the χ^2 distribution with 1 degree of freedom.

Cloning of LOC101886162, the SPRTN ortholog in zebrafish, called here sprtn. The zebrafish sprtn ortholog was cloned using a reciprocal, tblastn protein query, BLAST (Basic Local Alignment Search Tool), which identified a partial sequence of a single zebrafish sprtn ortholog. Using 3′ RACE PCRs (first choice RLM RACE, Ambion, Life Technologies), the C-terminal part and the 3′ UTR of SPRTN were obtained. The complete ORF of SPRTN was subsequently amplified from the cDNA of eight somite-stage zebrafish and cloned into the pCS2+ vector.

Zebrafish maintenance and manipulation. Zebrafish were kept under controlled water and temperature conditions in a 14-h light and 10-h dark cycle. Fertilized eggs were allowed to develop at 28.5 °C up to the required stages and analyzed and processed as indicated. All husbandry procedures and experiments were approved by the ethics committee and research commission of the University of Ulm, Germany. For knockdown experiments, fertilized eggs were injected with RNA antisense MO or capped RNA transcribed with the mMessage mMachine Kit (Ambion) starting from linearized plasmids. Injections were carried out at the one- to two-cell stage with an Eppendorf Femtojet Microinjector (Germany). An antisense MO targeting the start codon of SPRTN and a splice-site MO were used to generate loss-of-function zebrafish. Injections were controlled against those with a five-base mismatch control (Ctrl) MO. 1.5–17.6 ng of antisense MO against zebrafish SPRTN or Ctrl MO were injected. The coding sequence of human SPRTN was amplified from pFlag–CMV-1–SPRTN and cloned into the pCRII-TOPO vector (Invitrogen, Darmstadt, Germany) and subsequently subcloned into vector pCS2+ by the use of BamHI and XhoI restriction sites followed by T4 ligation. The clinical mutations were introduced using the QuikChange II XL Site-Directed Mutagenesis Kit (Agilent, Waldbronn, Germany) and mutagenesis primers. Staining with antibody against phosphorylated zebrafish γ-H2AX (a gift from J. Amatruda) followed a standard protocol as described before[46].

GFP reporter assay. To verify the efficacy and specificity of MO-induced knockdown, capped mRNA of GFP fused to the whole ORF of SPRTN and parts of the 5′ UTR was injected alone or along with MO or CtrlL MO into zebrafish eggs at the one-cell stage. At 24 hpf, embryos were assayed for GFP fluorescence on a Keyence BZ8000K fluorescent microscope.

33. Borck, G. et al. Loss-of-function mutations of ILDR1 cause autosomal-recessive hearing impairment DFNB42. Am. J. Hum. Genet. **88**, 127–137 (2011).
34. Bahlo, M. & Bromhead, C.J. Generating linkage mapping files from Affymetrix SNP chip data. Bioinformatics **25**, 1961–1962 (2009).
35. Abecasis, G.R., Cherny, S.S., Cookson, W.O. & Cardon, L.R. Merlin—rapid analysis of dense genetic maps using sparse gene flow trees. Nat. Genet. **30**, 97–101 (2002).
36. Leutenegger, A.L. et al. Estimation of the inbreeding coefficient through use of genomic data. Am. J. Hum. Genet. **73**, 516–523 (2003).
37. DePristo, M.A. et al. A framework for variation discovery and genotyping using next-generation DNA sequencing data. Nat. Genet. **43**, 491–498 (2011).
38. McKenna, A. et al. The Genome Analysis Toolkit: a MapReduce framework for analyzing next-generation DNA sequencing data. Genome Res. **20**, 1297–1303 (2010).
39. Wang, K., Li, M. & Hakonarson, H. ANNOVAR: functional annotation of genetic variants from high-throughput sequencing data. Nucleic Acids Res. **38**, e164 (2010).
40. Drmanac, R. et al. Human genome sequencing using unchained base reads on self-assembling DNA nanoarrays. Science **327**, 78–81 (2010).
41. Bansal, V. & Bafna, V. HapCUT: an efficient and accurate algorithm for the haplotype assembly problem. Bioinformatics **24**, i153–i159 (2008).
42. Hisama, F.M. et al. Coronary artery disease in a Werner syndrome–like form of progeria characterized by low levels of progerin, a splice variant of lamin A. Am. J. Med. Genet. A. **155A**, 3002–3006 (2011).
43. Saha, B. et al. Ethnic-specific WRN mutations in South Asian Werner syndrome patients: potential founder effect in patients with Indian or Pakistani ancestry. Mol. Genet. Genomic Med. **1**, 7–14 (2013).
44. Jackson, D.A. & Pombo, A. Replicon clusters are stable units of chromosome structure: evidence that nuclear organization contributes to the efficient activation and propagation of S phase in human cells. J. Cell Biol. **140**, 1285–1295 (1998).
45. Cortez, D., Guntuku, S., Qin, J. & Elledge, S.J. ATR and ATRIP: partners in checkpoint signaling. Science **294**, 1713–1716 (2001).
46. Zhou, W. et al. FAN1 mutations cause karyomegalic interstitial nephritis, linking chronic kidney failure to defective DNA damage repair. Nat. Genet. **44**, 910–915 (2012).

17
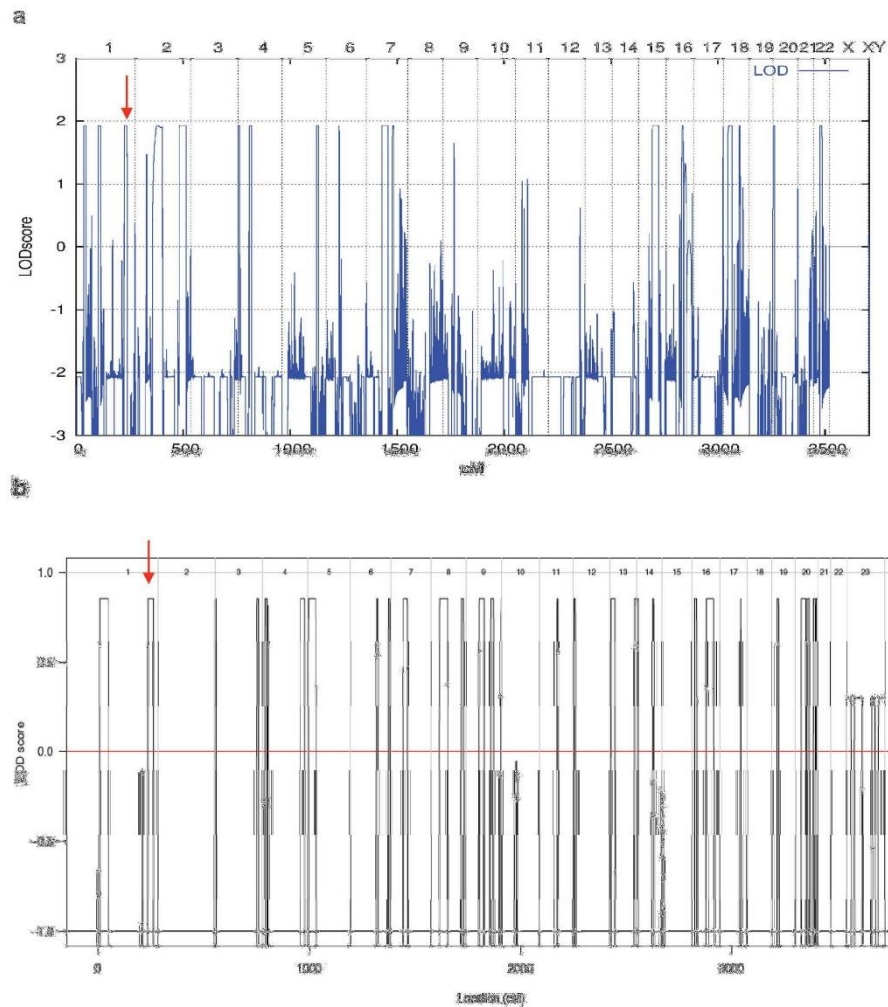
Supplementary Figure 1

Parametric genome-wide linkage analysis.

(**a**) LOD scores obtained from parametric linkage analysis of family A. Linkage was calculated using 20,044 selected SNP markers from the Affymetrix SNP Array 6.0. LOD scores calculated with ALLEGRO are given along the y-axis relative to genomic position in cM (centiMorgan) on the x-axis. Chromosomes are concatenated from p-ter to q-ter from left to right. Red arrow indicates position of *SPRTN*. (b) LOD scores

obtained from parametric linkage analysis of Family B under a recessive genetic model. LOD scores are on the y-axis and cumulative genomic position in cM (centiMorgan) on x-axis. The vertical lines depict the boundaries of each chromosome. The maximum theoretical autosomal LOD score of 0.85 is achieved at 29 sites, while the maximum chromosome X LOD score of 0.30 is achieved at four regions. The red arrow indicates the location of *SPRTN*.
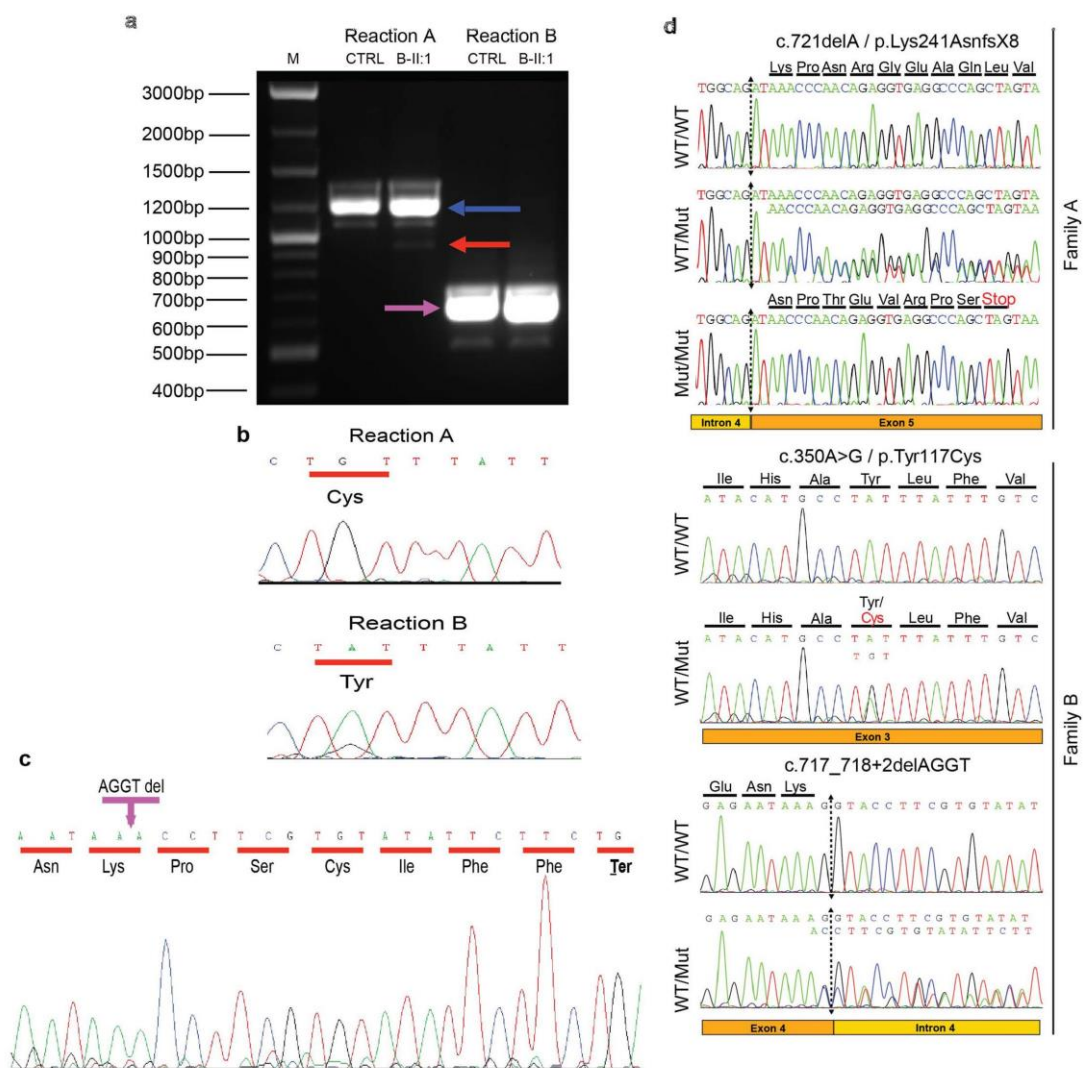
Supplementary Figure 2

RT-PCR analysis and Sanger sequencing.

(**a**) RT-PCR study of *SPRTN*. M indicates molecular marker. Reaction A, amplifying isoform 1, with primers in exon 2 and 5, revealed a full length allele of 1205bp (blue arrow) in both a healthy individual (CTRL) and B-

II:1. A very weak band (red arrow) corresponding to skipping of exon 4 (1205bp-268bp=937bp) is observed in B-II:1. Reaction B, amplifying isoform 2, with primers in exon 2 and intron 4 revealed a band at 640bp (pink arrow). (**b**) Sequence trace of the B-II:1. Reaction A amplified only the allele with the missense p.Tyr117Cys variant. Reaction B preferentially amplified the allele without the missense variant. (**c**) Sequencing of the reaction B in B-II:1 with reverse primer revealed the c.717_718+2delAGGT mutation, confirming that reaction B amplified only the allele including the 4bp deletion. Therefore the consequence of this deletion is mostly intron 4 inclusion causing p.Lys239LysfsX7. (**d**) Sequence chromatograms of all three identified mutations, after PCR amplification of genomic DNA. The amino acid translation is shown in the three-letter code above the chromatograms.
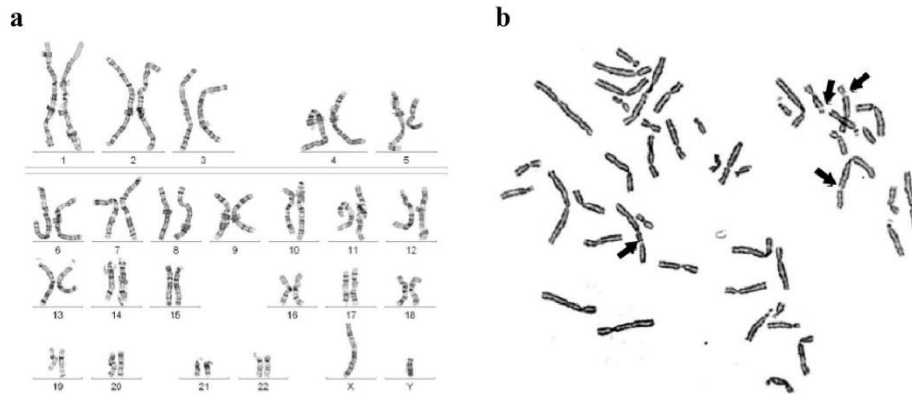
Representative images of peripheral blood metaphase spreads of B-II:4.

(**a**) G-banded analysis of lymphocyte cells showed random, spontaneous breaks and unbalanced rearrangements, including deletions, acentric fragments and marker chromosomes in 13 of 30 cells analyzed. The remaining cells showed an apparently normal male karyotype. A representative abnormal karyotype shows 46,XY,del(5)(?q31.3). (**b**) Examination of solid stained metaphase chromosomes showed an abnormal level of spontaneous chromosome breakage (arrows). There were 39 breaks in 45 analyzed cells, while the control sample showed 3 breaks in 45 cells. A similar level of spontaneous breakage was observed in the other proband (B-II:1). G-banded analysis of lymphocyte cells showed random, spontaneous breaks and rearrangements, including translocations and deletions, in 14 of 25 cells analyzed (data not shown).

45,XY,-21,del(6)(?q13)   46,XY,del(9)(?p21)

P15

P16
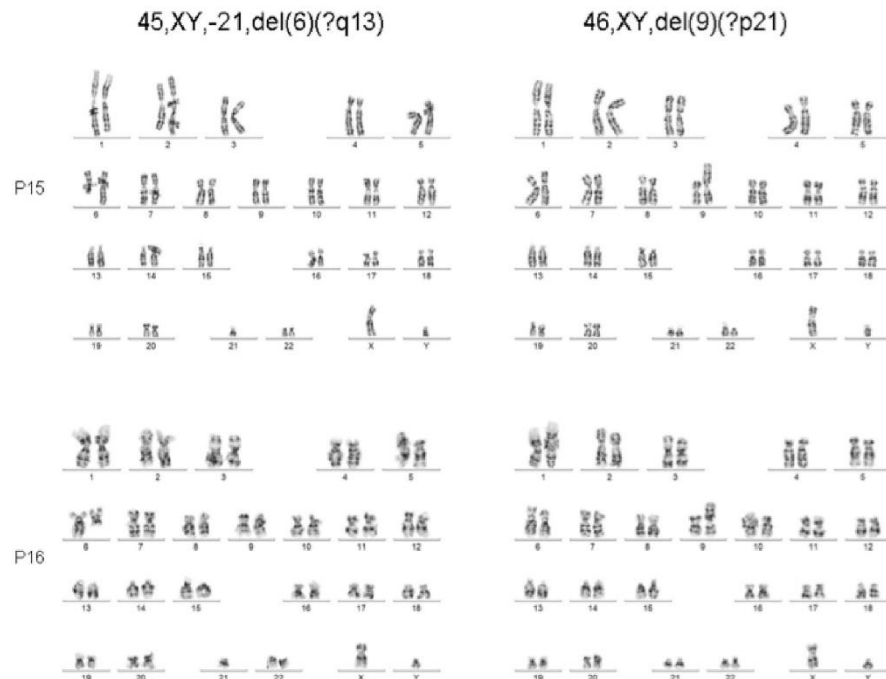
Supplementary Figure 4

Representative images of fibroblast metaphase spreads of B-II:1.

G-banded analysis of two subsequent B-II:1 fibroblast passages, 15 and 16, showed random, spontaneous breaks, balanced and unbalanced rearrangements, including deletions, acentric fragments and marker chromosomes in 9 of 30 cells analyzed from passage 15, and in 9 of 42 cells analyzed from passage 16. The remaining cells showed an apparently normal male karyotype. Depicted are two cytogenetically defined clones in both subsequent passages, 46,XY,del(9)(?p21) and 45,XY,-21,del(6)(?q13), the latter was identified in three metaphases of passage 16. Examination of solid stained metaphase chromosomes also showed an abnormal level of spontaneous chromosome breakage. There were 43 breaks in 47 analysed cells, while the control sample showed 1 break in 30 cells (data not shown).
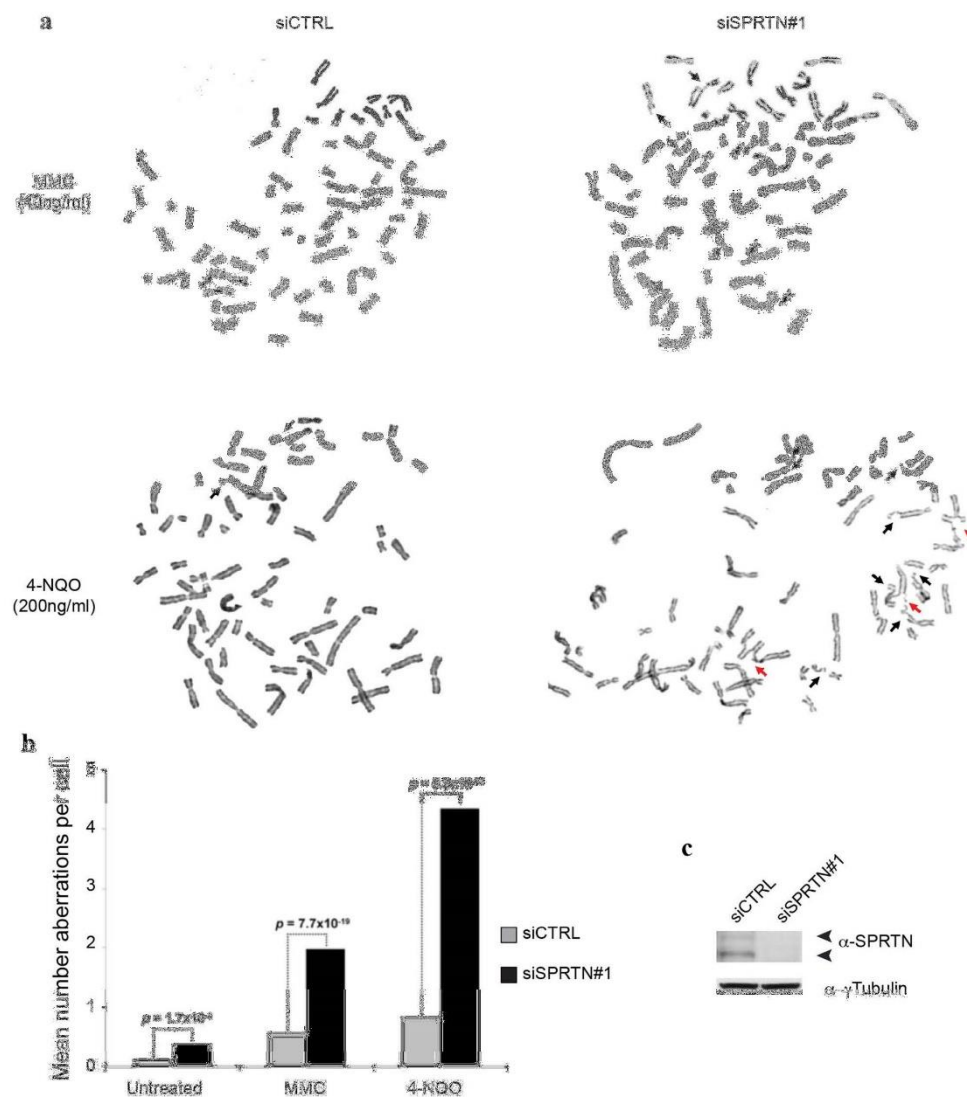
Supplementary Figure 5

Depletion of SPRTN by siRNA results in chromosomal instability.

(**a**) Representative images of metaphase spreads of siRNA transfected HEK293T cells. Black arrows indicate chromatid breaks. Red arrows indicate open multiradial figures each representing several chromatid breaks. (**b**)

Mean number of aberrations per cell observed in 100 metaphases of HEK293T cells transfected with siRNA alone or additionally treated either with 40ng/ml of MMC or 200ng/ml of 4-NQO. Bar graphs summarize three independent experiments. p-values are given above the graphs. (**c**) Depletion of SPRTN was confirmed by western blot. Tubulin was used as a loading control.

25
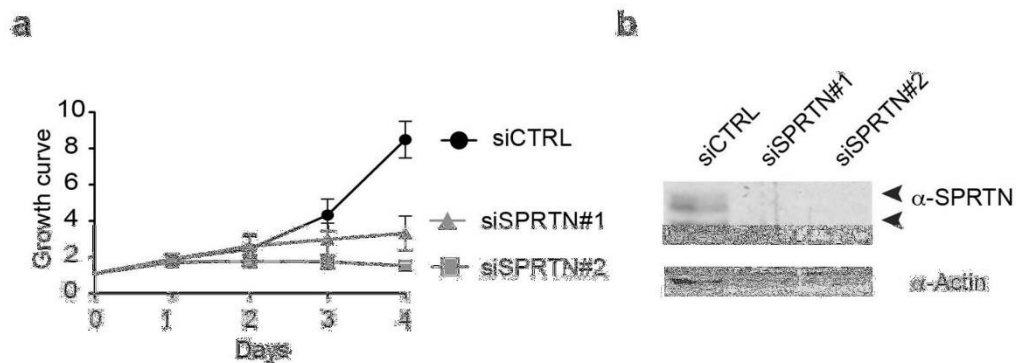
Supplementary Figure 6

SPRTN depletion suppresses cell proliferation.

(**a**) 50'000 of U2OS cells were seeded at day 0 and normalized to 1 (y-axis). Every 24 hours cells (x-axis) were washed, trypsinized, resuspended in 1mL medium and counted. The graph represents the mean +/- standard deviation of 3 independent experiments. Each experiment was performed in triplicate. (**b**) Efficacy of SPRTN depletion.
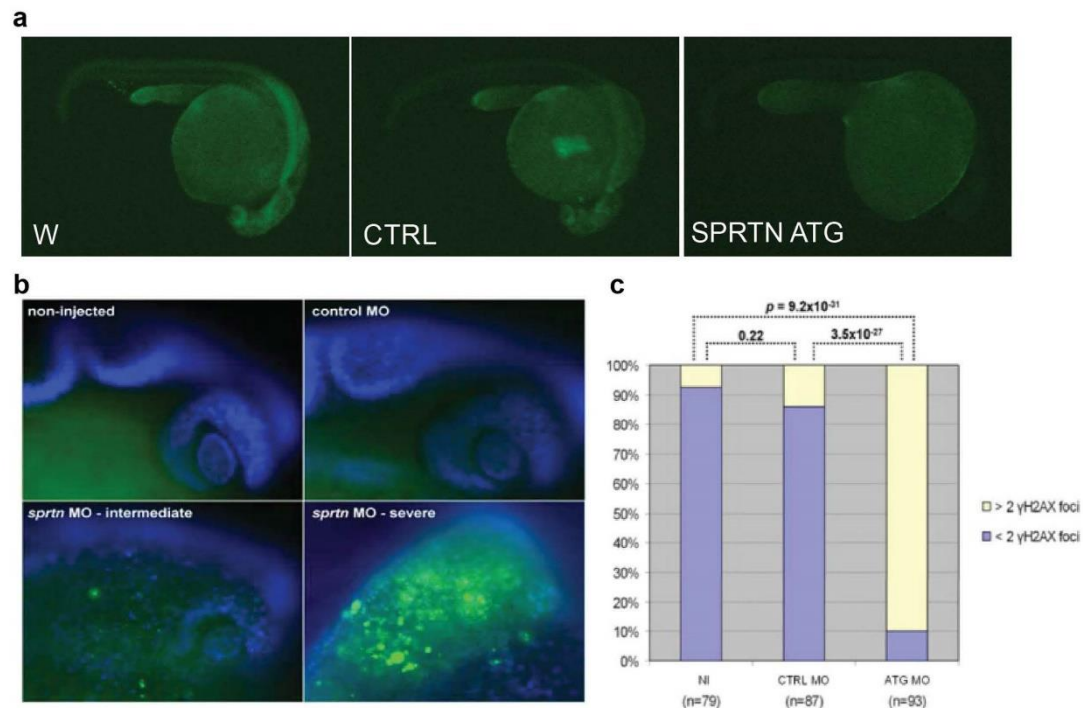
SPRTN has an evolutionary conserved role in the DNA damage response.

(**a**) Morpholino specificity and efficacy demonstrated by knockdown of GFP reporter expression. Co-injection of the translation blocking antisense MO targeted against the 5'-UTR inhibited all GFP fluorescence, while coinjection of a 5 bases mismatch control MO did not repress fluorescence. (**b**) Lateral view of the head region of 27 hpf zebrafish embryos stained with zebrafish anti γ-H2AX (FITC). Nuclei were counterstained with DAPI (blue). Knockdown of sprtn with 1.5ng ATG MO significantly increases the staining for γ-H2AX, indicating increased DDR. (**c**) Quantification of γ-H2AX foci after sprtn downregulation in zebrafish. Bar graphs summarize three independent experiments. Statistical significance was determined using Fisher's exact test, p-values are given above the graphs. NI = non injection.
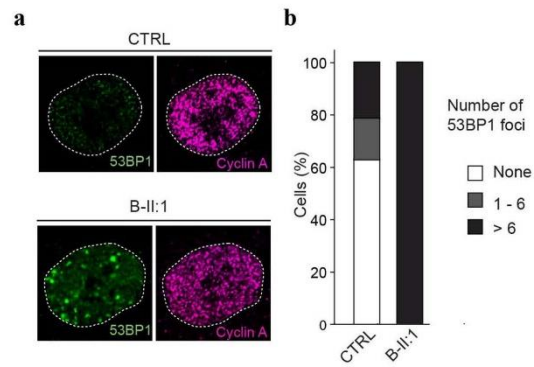
Supplementary Figure 8

Mutations in *SPRTN* cause elevated number of DNA double-strand breaks (DSBs) in S phase.

(**a**) Primary skin fibroblasts stained with the S-phase cell cycle marker (Cyclin A) and antibodies against 53BP1 (DNA double strand breaks marker). (**b**) The number of 53BP1 foci per cell in cyclin A positive cells was quantified in three independent experiments with greater than 100 cells scored per condition per experiment.
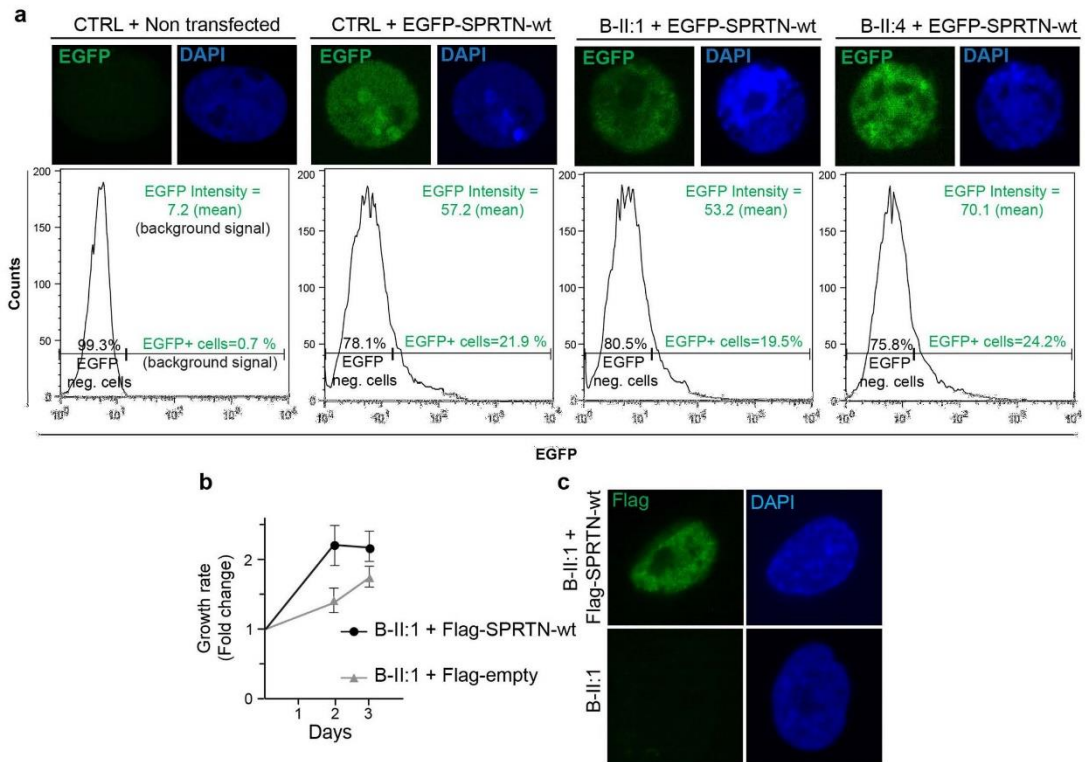
Supplementary Figure 9

Overexpression of WT SPRTN rescues DNA replication and proliferation phenotypes in patient LCLs and fibroblasts.

(**a**) The overexpression of EGFP-SPRTN-wt in stable transfected LCLs was confirmed by fluorescence microscopy (upper panel) and flow cytometry (lower panel). Note that only 20-24% of stable-transfected LCLs express EGFP-SPRTN. (**b**) Flag-SPRTN-wt or Flag-empty vector transiently transfected B-II:1 skin fibroblasts were seeded and growth curve was measured as indicated in Supplementary Fig. 6; three independent experiments, error bars; s.e.m. (**c**) Flag-SPRTN-wt expression in primary skin fibroblasts was confirmed by immunofluorescence analysis.
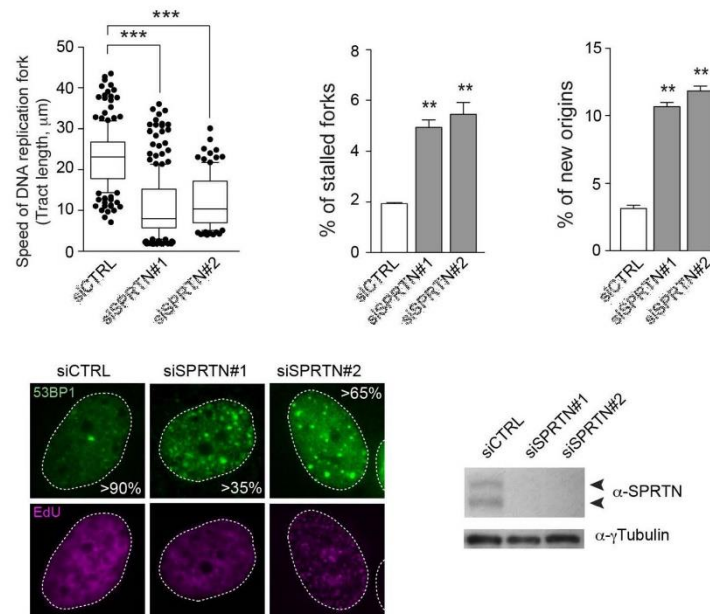
Supplementary Figure 10

Depletion of SPRTN causes DNA replication stress.

a) U2OS cells were treated with two independent siRNAs against SPRTN (siRNA-SPRTN#1 or siRNA-SPRTN#2) or control siRNA (siCTRL) and DNA replication forks were analyzed. The quantification from three independent experiments using the same methodology as in Figure 4 Panels a-d. (**b**) Representative cells with huge increase in the number of 53BP1 (markers of DSBs) foci in S-phase (EdU-positive; cells were grown in the presence of EdU for 30 min before fixation) of SPRTN-depleted U2OS cells. % of cells with depicted phenotypes when more than 100 cells were scored per condition in three independent experiments. (**c**) Efficacy of SPRTN depletion.
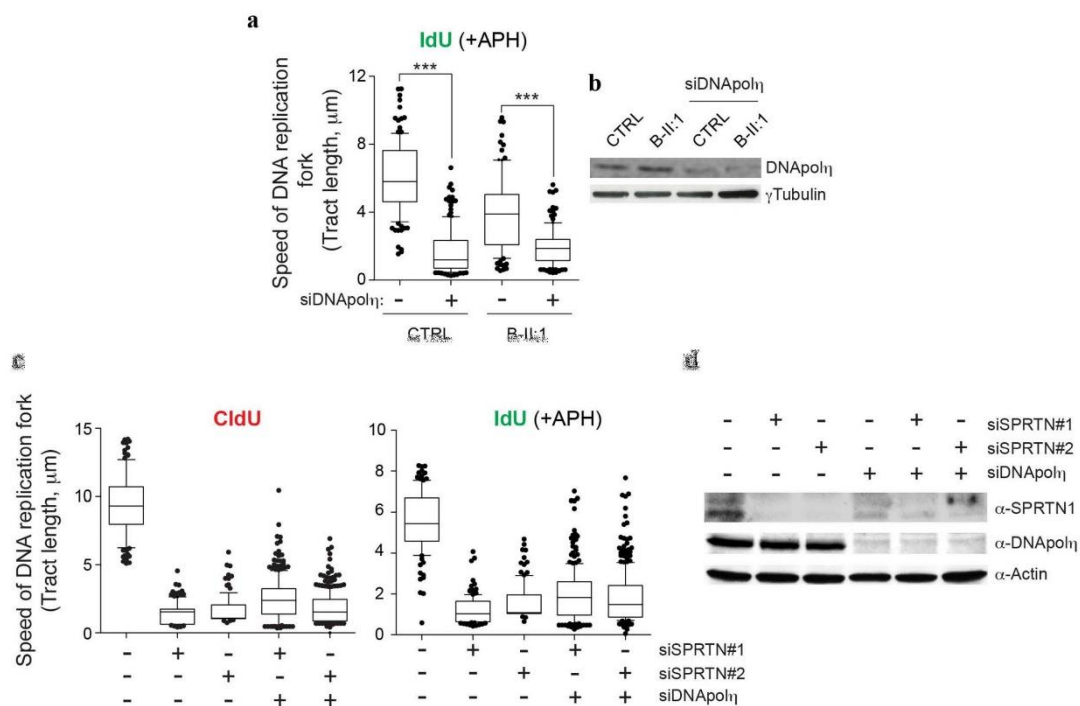
Supplementary Figure 11

Depletion of DNA polymerase η is unable to rescue the DNA replication defect in patient LCLs or SPRTN-depleted U2OS cells.

Analysis of DNA replication fork progression in patient cells or SPRTN-depleted U2OS cells +/- co-depletion of DNA polymerase η by DNA fiber assay as described earlier in the text. (**a**) DNA fiber analysis of patient LCLs in the presence of APH. (**b**) Efficacy of siRNA depletion as indicated. (**c**) DNA fiber analysis with (right panel) or without APH (left) in siRNA-depleted U2OS cells. Two independent experiments with 100 fibers per condition per experiment. (**d**) The efficacy of depletion

.

31
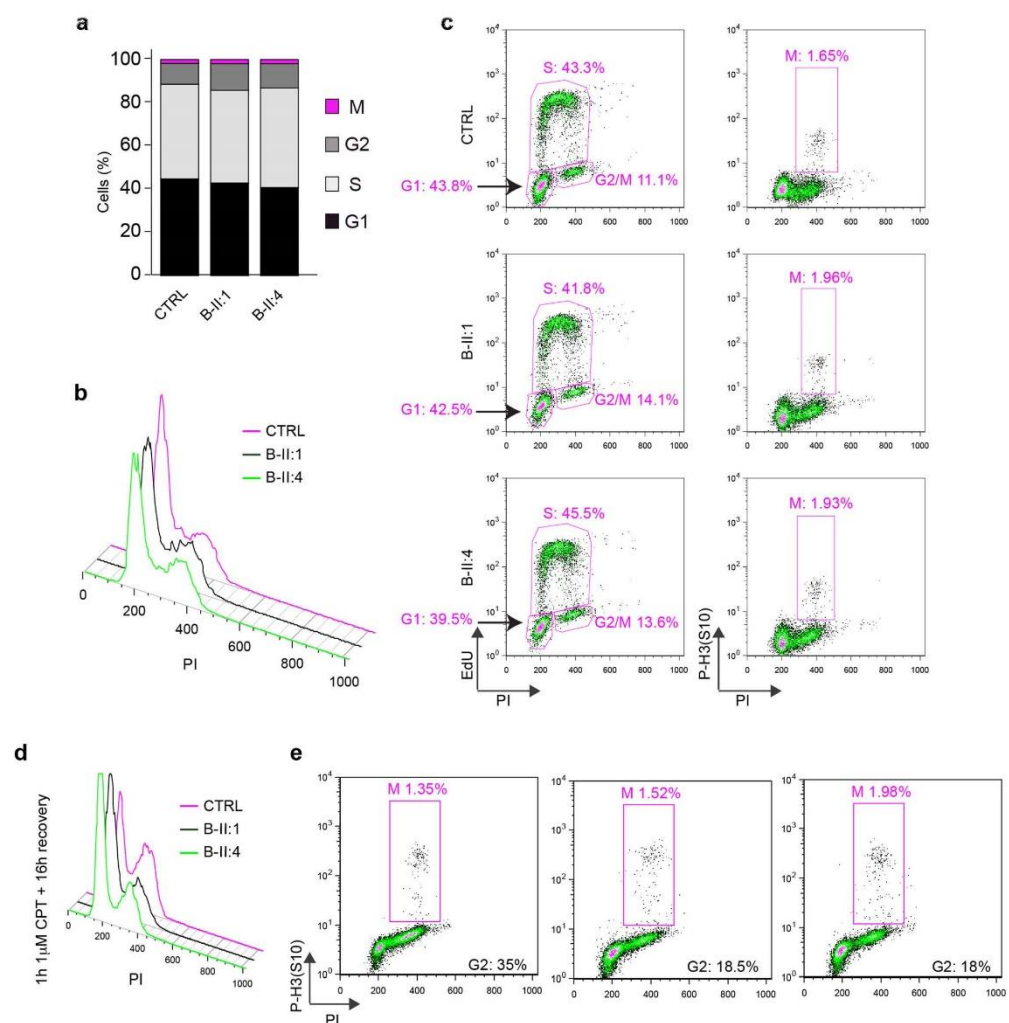
Cell cycle profile of unchallenged or CPT-challenged patients' LCL cells.

(**a**) Graphic representation of the cell cycle distribution in control and patient LCLs. G_1, S, G_2 and mitotic (M) cells were determinated by flow cytometry based on the triple staining with propidium iodide (PI: DNA content), EdU (S-phase) and phosph-Ser10 histone H3 (marker for mitotic cells).(**b**) Representative histograms

for DNA content (PI). The y-axis represents cell counts and the x-axis represents DNA area. The first peak indicates cells in G_1 and the second peak indicates cells in G_2-M. Cells between two indicated peaks represent S-phase. (**c**) Representative dotplot distribution of EdU (left graph) or phospho-Ser10 histone H3 (right graph) positive cells (y axis) versus DNA content (x axis). (**d**) Graphic representation of the cell cycle distribution following induction of replication-related DSB (1μM CPT treatment for 1 hour and recovery for 16 hours). (**e**) Representative dotplot distribution of mitotic cells detected by p-H3(S10) and depicted in pink rectangles (% of M cells).

.
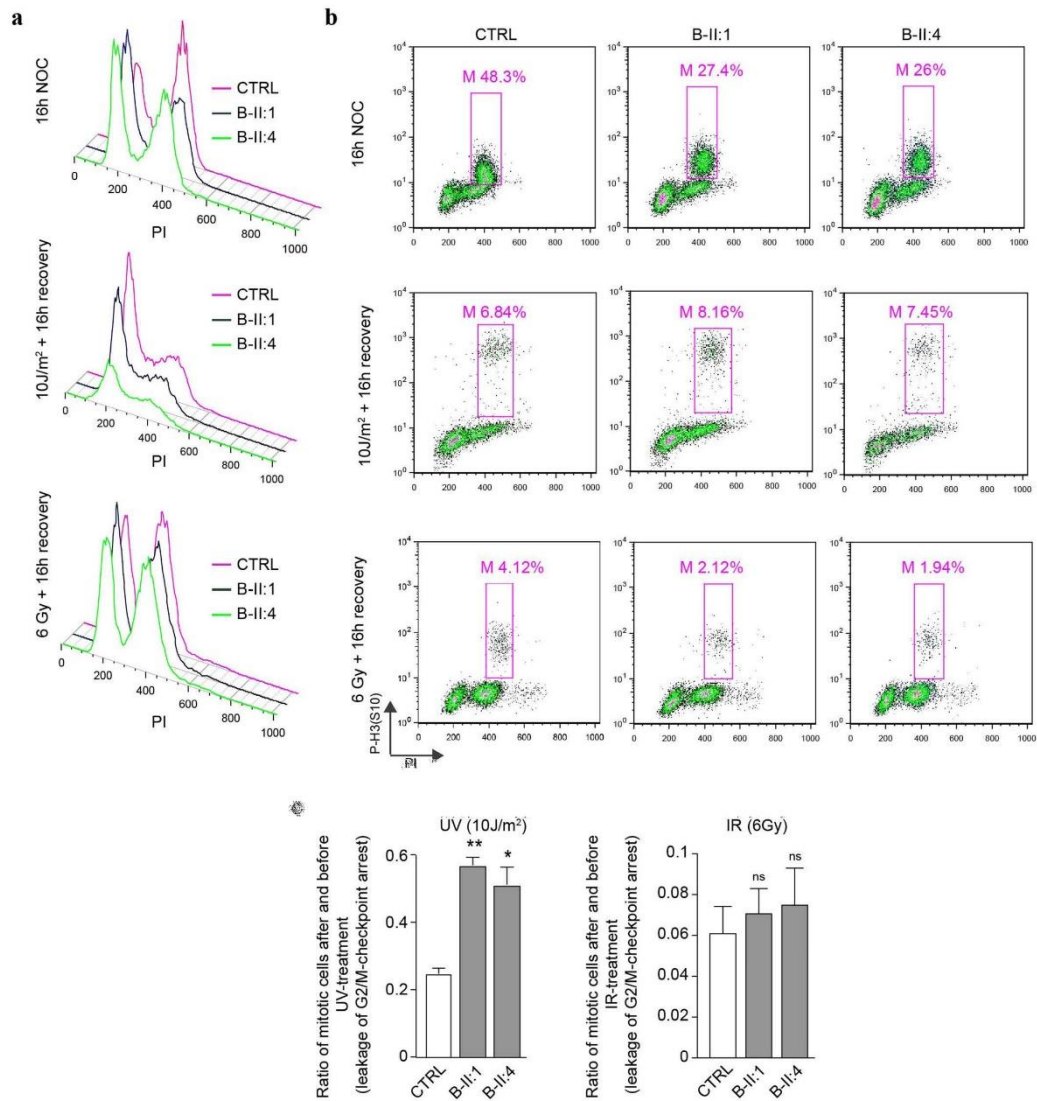
Supplementary Figure 13

G2/M checkpoint leakage following replication-related DSB but not ionizing radiation (IR)-induced DSB of patient LCLs.

(**a**) Cell cycle profile of patient cells before DNA damage or after UV-irradiation ($10J/m^2$) or IR (6 Gy)

treatment. The cells were allowed to recover for 16 hours in the presence of nocodazole and analysed by PI profile. (**b**) Representative dotplot distribution of phospho-Serine-10 histone H3 positive cells. (**c**) Due to proliferation defects observed in patient LCL's, G2-M checkpoint efficiency was expressed as the mitotic ratio between the number of mitotic cells after and before DNA damage. Note that G2/M-checkpoint is not properly functional in UV-treated patient LCLs (about 3-fold less mitotic cells after UV) when compared to control cells (7-fold less mitotic cells after UV). In contrary to UV, IR treatment (b and c) is equally efficient in both patient and control LCLs (about 12 fold).
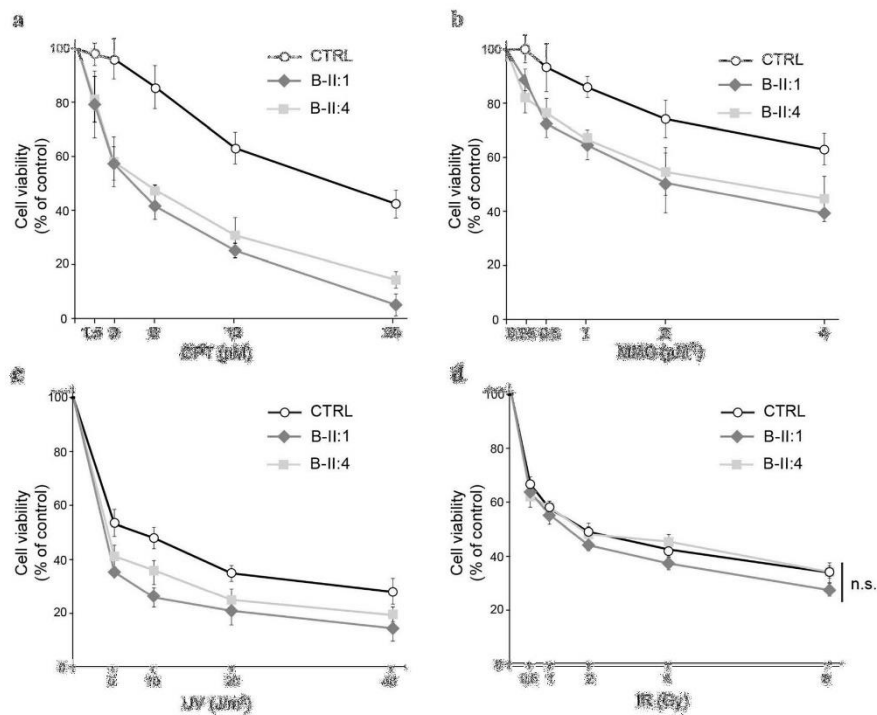
Supplementary Figure 14

Patient cells are hypersensitive to replication-related DNA damaging agents but not to IR.

Cell viability of control and patient LCL's after treatment with different DNA damaging agents: (**a**) Camptothecin (CPT), (**b**) Mitomycin C (MMC), (**c**) UV-radiation, and (**d**) ionizing radiation (IR), using a commercial MTT assay. The cells were treated for 48 hours with the indicated genotoxic agents and allowed to recover for 48 hours. (a-d) Three independent experiments, and each experiment was performed in triplicate. n.s. = not significant, unpaired t-test

.

a

NOC

UV + NOC

siCTRL
siChk1
siSPRTN#2
siSPRTN#1

DAPI

DAPI

b

α-SPRTN
α-Chk1
α-Actin

siCTRL   siSPRTN#1   siSPRTN#2   siChk1

c

siCTRL   siChk1   siSPRTN#1   siSPRTN#2

M: 20.7%   M: 4.49%   M: 10.1%   M: 15.2%   16h NOC

M 2.74%   M 1.05%   M 2.01%   M 6.03%   UV (10J/m²) + 16h NOC

P-H3(S10)

DAPI

d

Ratio of mitotic cells after and before UV-treatment (leakage of G2/M-checkpoint arrest)

siCTRL   siChk1   siSPRTN#1   siSPRTN#2
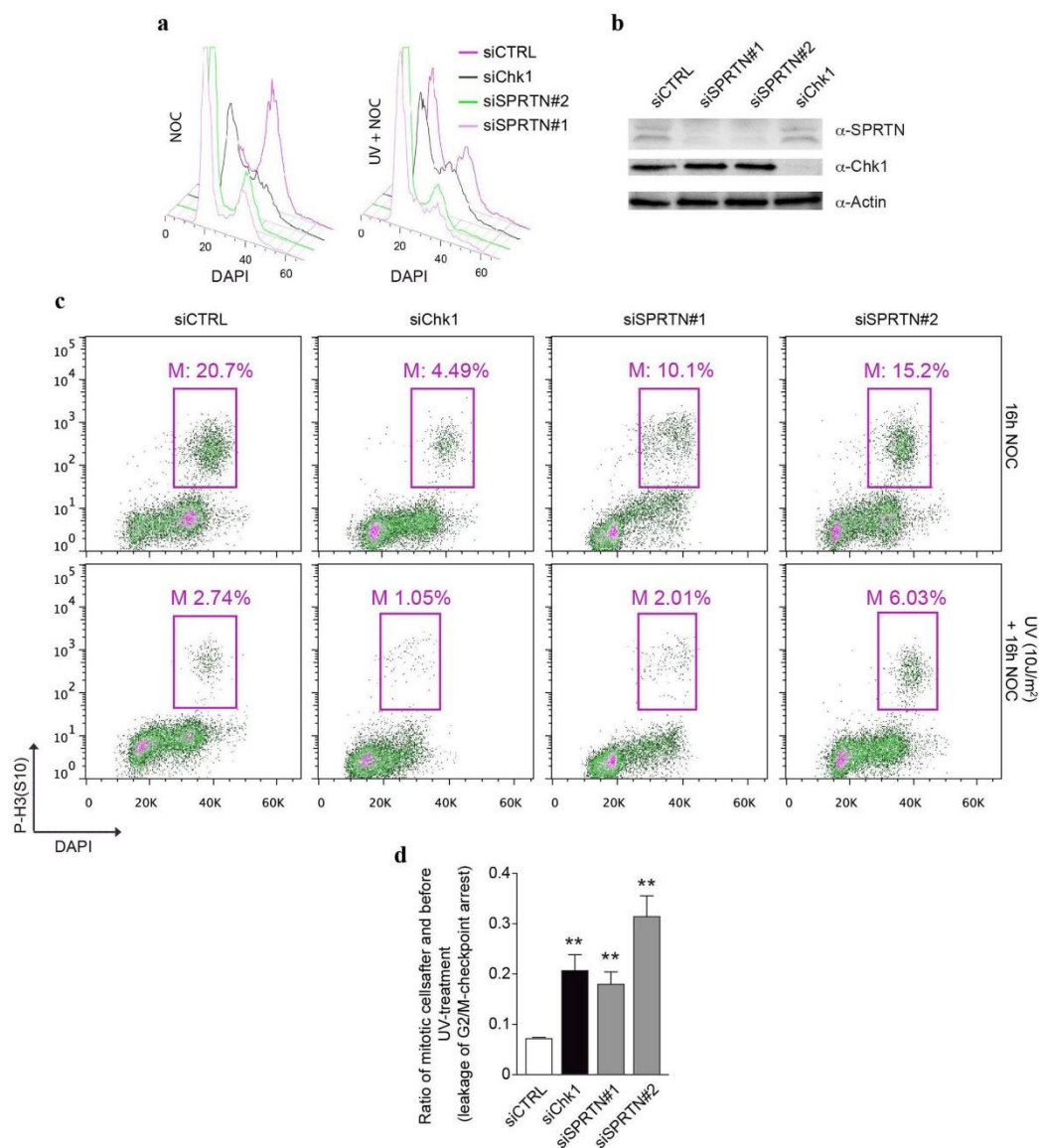
Supplementary Figure 15

Depletion of SPRTN causes G2/M-checkpoint leakage after UV in U2OS cells.

(**a**) Cell cycle profile analysed by DNA content (DAPI) of siRNA-depleted cells without or with UV-irradiation

37

in the presence of nocodazole (NOC). (**b**) Western blot analysis of siRNA-depletion efficacy. (**c**) A representative dotplot distribution of mitotic cells detected by p-H3(S10) and depicted in red rectangles (% of M cells). In control cells (siCTRL) there is approximately 8-fold less mitotic cells after UV comparing to unchallenged conditions (efficient G2/M-arrest), whereas in SPRTN-depleted cells there is only about 3-fold (SPRTN# 2) or 5-fold less (SPRTN#1). (**d**) To better visualize the G2/M-defect after UV-damage in DVC1-depleted cells mitotic cells were calculated and presented as a mitotic ratio after and before UV-treatment. Depletion of Chk1 was used as a positive control for G2/M leakage.

.

Supplementary Table 1a. Exome variant filtering in A-IV:1

Filter	Count
Total count of variations	425,316
Reaching minimal quality (>6 reads; Qual> 15)	118,166
Splice +/10bp or protein change, not in In-house DB, 1000genomes, MAF<0.01	525
Homozygous (Allele frequency >75%), MAF<0.01	73
Co-segregating in the family, MAF<0.01	11
Not in dbSNPv137	1
Protein truncating or splice site variant	1

Supplementary Table 1b. Exome variant filtering in B-II:4 under homozygous, hemizygous and compound heterozygous genetic models. AAF = alternate allele frequency.

Filter	No. variants
Total variants detected with quality $\geq$ 10	380,449
Variant quality$\geq$ 13	283,748
Located within one of 33 linkage intervals	33,176
Rare (AAF $\leq$1% in the 1000 Genomes and NHLBI ESP6500 data sets, and AAF $\leq$4% in the Complete Genomics 69 data set and 132 in-house exomes)	5,531
Within 2 bp of splice site, or predicted to affect protein sequence	210
Pairs of compound or phase unknown heterozygous variants (Table S2B)	65*
Homozygous variants (Table S2C)	7
Hemizygous variants (Table S2D)	3

* Located in nine genes, one of which was *SPRTN*.

1

Supplementary Table 2a. Homozygous variants with minor allele frequencies (MAF) < 0.01 showing co-segregation in the family A.

Gene	Chromosome	Quality	Total Depth	Allele Freq.	Protein Change	dbSNP v137
MRPL55	1	39	18	89	Arg25His	rs74140967
MRPL55	1	51	8	100	Gly39Ser	rs76046017
GUK1	1	40	15	93	Arg118Trp	rs56280722
OBSCN	1	199	57	100	Arg467Cys	rs74142685
OBSCN	1	255	184	100	Thr1513Met	rs74142695
OBSCN	1	51	8	100	Gly2813Arg	rs74142687
OBSCN	1	81	18	100	Arg5693Met	rs80298121
OBSCN	1	51	8	100	Tyr7735Phe	rs77969788
SPRTN	**1**	**496**	**166**	**98**	**Lys241AsnfsX8**	**no**
RGPD1	2	51	8	100	Pro20Leu	rs201509849
CFTR	7	192	68	97	Leu997Phe	rs1800111

2

Supplementary Table 2b. Candidate compound heterozygous variants in family B. See Supplementary Table 1b for criteria used to identify candidates.

Gene	Chr.	Quality	Total Depth	Alternate Depth	Protein Change	dbSNP v137
E2F2	1	30	8	2	Asp430Gly	no
E2F2	1	266	18	11	Gly205Arg	rs2229297
EPHA8	1	200	23	8	Gly45Ser	rs45498698
EPHA8	1	412	28	20	Pro607His	rs144329757
PRAMEF2	1	622	297	56	Leu105Ter	rs78738981
PRAMEF2	1	579	131	47	Leu310Val	no
SPRTN	**1**	**836**	**77**	**36**	**Tyr117Cys**	**no**
SPRTN	**1**	**1844**	**52**	**26**	**Frameshift (c.717_718+2delAGGT)**	**no**
DOCK5	8	65	37	10	Splicing (c.976+2T>G)	rs77327996
DOCK5	8	64	14	4	Cys956Phe	rs201180829

3

Supplementary Table 2c. Candidate homozygous variants in family B. See Supplementary Table 1b for criteria used to identify candidates.

Gene	Chr.	Quality	Total Depth	Alternate Depth	Protein Change	dbSNP v137
SLC45A1	1	15	1	1	Ala705Gly	no
AOAH	7	18	12	8	Leu640Profs*26	no
UBXN8	8	1802	67	64	Arg207Ser	rs77443237
AMER2	13	19	2	2	Lys168Asn	no
CES1	16	158	18	12	Splicing (c.1087-2dupT)	no
EXOC3L1	16	116	4	4	Tyr75Asn	rs117403380
PKD1L3	16	2998	50	47	Lys1233Asnfs*21	rs149635567

Supplementary Table 2d. Candidate hemizygous variants in family B. See Supplementary Table 1b for criteria used to identify candidates.

Gene	Chr.	Quality	Total Depth	Alternate Depth	Protein Change	dbSNP v137
MXRA5	X	378	12	12	Arg2734Gln	rs144024869
WDR13	X	19	2	2	Gln53Lys	no
MAGEC3	X	704	21	21	Val567Phe	rs143730187

4

42

Supplementary Table 3. Co-segregation at the *SPRTN* locus

Family A	
A-III:1	c.721delA / wt
A-III:2	c.721delA / wt
A-IV:1	c.721delA / c.721delA
A-IV:2	c.721delA / wt
Family B	
B-I:1	c.717_718+2delAGGT / wt
B-I:2	c.350A>G / wt
B-II:1	c.717_718+2delAGGT / c.350A>G
B-II:2	c.717_718+2delAGGT / wt
B-II:3	c.717_718+2delAGGT / wt
B-II:4	c.717_718+2delAGGT / c.350A>G

5

Supplementary Table 4. DNA primers used in this study.

SPRTN **primer for reverse transcription PCR:**
SPRTN-2F 5'-CCATCCGTCTCAGCGAACC-3'
SPRTN-5R 5'-CAAAAGCGAAGAAAGTCTTGA-3'
SPRTN-4R 5'-gagcaaagtctgttttcctaccatc-3'
Primer for amplification of zebrafish *SPRTN*:
Forward 5'- CGTTGACATCTTTAGCTCCACACT-3`
Reverse 5'-CGTCTTGAGACCATTTCCGCCTAT-3`
Zebrafish *SPRTN* 3'RACE PCR primer:
Forward 5'-CCACAGACAAGAAACGAGAGGAGGTCAGAA-3'
Reverse 5'-AGCAGGCAAACAATCCTCCAGCCCAAATCA-3'
Primers used for cloning of human *SPRTN* from pFLAG-CMV into pCRII-TOPO:
forward 5'-GGATCCATGGATGATGACTTGATGTTG-3'
reverse 5'-CTCGAGTCAAAGACTTTCTTCGCTTTTG-3'
Zebrafish mutagenesis primer:
c.721Adel forward 5'-CAGAGAATAAAGATAACCCAACAGAGGTGAGGC-3'
c.721Adel reverse 5'-GCCTCACCTCTGTTGGGTTATCTTTATTCTCTG-3'
c.350A>G forward 5'-CTGCATGAAATGATACATGCCTGTTTATTTGTCACTAATAACGAC-3'
c.350A>G reverse 5'-GTCGTTATTAGTGACAAATAAACAGGCATGTATCATTTCATGCAG-3'

6

44

Supplementary Table 5. Antisense morpholino oligonucleotides and siRNA.

Zebrafish *SPRTN* RNA antisense morpholino oligonucleotides (MO)
ATG MO 5'- GAAGATGATGGAGGATGAAGACTTT-3'
splice-site MO 5'- CACATCTGAGGAAGAGAAACATTGA-3'
CTRL MO 5'- GAACATCATGGACGATCAAGAGTTT -3'
siRNA sequences
siSPRTN#1 : 5`-UCAAGGAACCAGAGAAUUATT-3` (Microsynth)
siSPRTN#2: 5'-AAUACAGGUGGUACUUGAGACUUUG-3' (Microsynth)[1]
siCHK1: 5'-AAGCGUGCCGUAGACUGUCCATT-3' (Microsynth)
siPOLH: 5'CUGGUUGUGAGCAUUCGUGUATT-3' (Microsynth)[46]
siNS was obtained fromQiagen

7

45

Dysfunction of the MDM2/p53 axis is linked to premature aging

Davor Lessel,[1] Danyi Wu,[2] Carlos Trujillo,[3] Thomas Ramezani,[4] Ivana Lessel,[1] Mohammad K. Alwasiyah,[5] Bidisha Saha,[6] Fuki M. Hisama,[7] Katrin Rading,[1] Ingrid Goebel,[1] Petra Schütz,[8] Günter Speit,[8] Josef Högel,[8] Holger Thiele,[9] Gudrun Nürnberg,[9] Peter Nürnberg,[9,10,11] Matthias Hammerschmidt,[4,10,11] Yan Zhu,[2] David R. Tong,[2] Chen Katz,[2] George M. Martin,[6,12] Junko Oshima,[6,13] Carol Prives,[2] and Christian Kubisch[1,8]

[1]Institute of Human Genetics, University Medical Center Hamburg-Eppendorf, Hamburg, Germany. [2]Department of Biological Sciences, Columbia University, New York, New York, USA. [3]Genetics Unit, Dr. Erfan & Bagedo Hospital, Jeddah, Saudi Arabia. [4]Institute of Developmental Biology, University of Cologne, Cologne, Germany. [5]Aziziah Maternity and Children's Hospital, Ministry of Health, Jeddah, Saudi Arabia. [6]Department of Pathology, University of Washington, Seattle, Washington, USA. [7]Division of Medical Genetics, Department of Medicine, University of Washington, Seattle, Washington, USA. [8]Institute of Human Genetics, University of Ulm, Ulm, Germany. [9]Cologne Center for Genomics, [10]Center for Molecular Medicine Cologne, and [11]Cologne Excellence Cluster on Cellular Stress Responses in Aging-Associated Diseases, University of Cologne, Cologne, Germany. [12]Molecular Biology Institute, UCLA, Los Angeles, California, USA. [13]Department of Medicine, Chiba University, Chiba, Japan.

The tumor suppressor p53, a master regulator of the cellular response to stress, is tightly regulated by the E3 ubiquitin ligase MDM2 via an autoregulatory feedback loop. In addition to its well-established role in tumorigenesis, p53 has also been associated with aging in mice. Several mouse models with aberrantly increased p53 activity display signs of premature aging. However, the relationship between dysfunction of the MDM2/p53 axis and human aging remains elusive. Here, we have identified an antiterminating homozygous germline mutation in *MDM2* in a patient affected by a segmental progeroid syndrome. We show that this mutation abrogates MDM2 activity, thereby resulting in enhanced levels and stability of p53. Analysis of the patient's primary cells, genome-edited cells, and in vitro and in vivo analyses confirmed the MDM2 mutation's aberrant regulation of p53 activity. Functional data from a zebrafish model further demonstrated that mutant Mdm2 was unable to rescue a p53-induced apoptotic phenotype. Altogether, our findings indicate that mutant MDM2 is a likely driver of the observed segmental form of progeria.

Introduction

Two compelling lines of evidence establish p53 as a major tumor suppressor in humans. First, heterozygous germline mutations in the p53-encoding gene *TP53* cause Li-Fraumeni syndrome, an autosomal-dominant and highly penetrant early-onset cancer predisposition syndrome (1). Second, inactivating somatic *TP53* mutations have been identified in the majority of human tumors (2). The p53 protein is a DNA sequence–dependent transcriptional regulator of myriad genes whose products mediate diverse physiological pathways involved in cell-cycle progression, apoptosis, senescence, autophagy, genomic stability, fertility, stem cell differentiation, and cellular metabolism, many of which can be linked to tumor suppression (3, 4). Under basal conditions, p53 is maintained at very low cellular levels. However, in response to exogenous and endogenous stressors, p53 is rapidly stabilized and activated, leading to one or more of the above-mentioned cellular outcomes. Maintenance of low p53 levels or deactivation of p53 during recovery from stress is mostly attributable to the function of the E3 ubiquitin ligase MDM2 that binds primarily to a region within the p53 N-terminal transactivation domain. MDM2 controls cellular p53 levels and activity through at least 3 mechanisms: (a) direct binding and blockage of p53 transactivation ability; (b) monoubiquitylation leading to export of p53 out of the nucleus; and (c) polyubiquitylation leading to proteasomal degradation of p53 (5, 6). In fact, MDM2 is itself a direct transcriptional target of p53 and thereby forms an autoregulatory feedback loop, such that p53 and MDM2 tightly regulate each other's cellular levels and activities (7, 8).

While it is well established that p53 loss of function increases the risk for cancer, the relationship between the MDM2/p53 axis and human aging remains a matter of debate (9). This is an interesting question, especially in light of the envisaged therapeutic use of MDM2 inhibitors in oncology (10). For example, p53 protein levels accumulate in aged, "near-senescent" human fibroblasts (11), but decline in aged mouse populations (12). The p53 SNP p.Arg72Pro has been associated with increased longevity and survival (13), but paradoxically also confers reduced apoptotic potential (14, 15) and modest increases in cancer susceptibility (16). In addition, some human premature aging disorders (segmental forms of progeria) have been linked to p53 signaling and may yield insights into the broader aging phenomenon (17, 18).

The putative relevance of p53 action in aging is also reflected in mouse models that modulate the MDM2/p53 axis directly. Mice with N-terminal truncations of p53 in the presence of functional WT p53 (19, 20) and mice with N-terminal p53 mutations that mimic phosphorylation and are unable to be regulated by MDM2 have constitu-
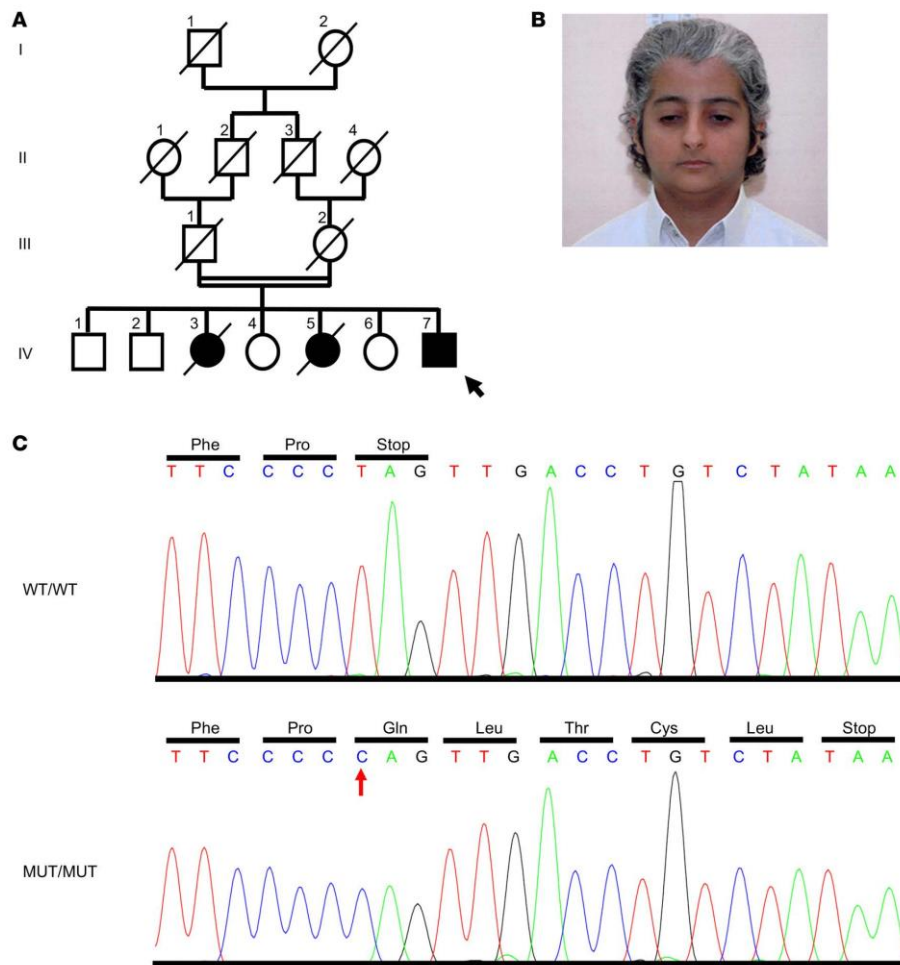
Figure 1. Identification of a causative mutation in *MDM2*. (A) Pedigree of a consanguineous family (black and white circles and squares denote affected and healthy individuals, respectively; arrow indicates the index patient; diagonal lines indicate deceased status; double line shows parental consanguinity). **(B)** Facial image of the index patient IV:7 at the age of 19 years. Note the patient's short stature (151 cm on the scale), prematurely gray hair, pinched facial features with a narrow nasal bridge, and small mouth. **(C)** Sequence chromatogram shows the c.1492T>C (p.*498Qext5) mutation (red arrow).

tively active p53 activity and display accelerated aging phenotypes (21). On the contrary, some mouse models with altered p53 or MDM2 expression, i.e., "super-p53" or hypomorphic MDM2 mice, display no signs of premature aging (22, 23), suggesting that simple elevation of p53 levels is insufficient to cause premature aging, as p53 is still tightly regulated in these cases. These seemingly conflicting results may be reconciled by positing that deregulating the MDM2-p53 feedback loop might be critical for abnormal aging processes.

Here, we present a patient affected by a segmental progeroid syndrome in whom we identified a homozygous germline *MDM2* mutation. This antiterminating *MDM2* mutation results in constitutive stabilization of p53 and MDM2, leading to altered p53 activity and dysfunction of the MDM2/p53 axis.

Results

Characteristics of the studied patient. We studied a patient who was referred to the International Registry of Werner Syndrome (www.wernersyndrome.org) with the putative diagnosis of a Werner syndrome–like segmental progeroid disorder. The index patient (IV:7, Figure 1, A and B) is the seventh child of unaffected, consanguineous parents of Saudi Arabian origin. At the age of 19 years, he presented with short stature (151 cm), pinched facial features, prematurely gray hair, scleroderma-like skin changes, high-pitched voice, hypogonadism, sparse pubic hair, small kidneys and consecutive kidney failure, followed by severe arterial hypertension (Figure 1B and Supplemental Table 1; supplemental material available online with this article; https://doi.org/10.1172/

47

A

B

C

D

E

48

Figure 2. The antiterminating MDM2 mutation is defective in its regulation of p53. (**A**) Protein levels of MDM2, p53, and actin in control and IV:7 fibroblasts treated with vehicle DMSO (–), Nutlin-3 (N, 10 μM), or daunorubicin (D, 0.1 mg/ml) for 24 hours. Immunoblot with the indicated antibodies. Graph shows the fold change of basal p53 levels over actin levels from 5 independent experiments. (**B**) Protein degradation rates of MDM2 and p53 in fibroblasts via CHX chase. Immunoblots show results of control 1 and IV:7 fibroblasts harvested at the indicated times (minutes) after CHX (100 μg/ml) treatment. Graphs show protein quantification (using ImageJ and GraphPad Prism software) and the half-lives of MDM2 (control 1: 62 min; IV:7: 92 min) and p53 (control 1: 45 min; IV:7: 82 min). (**C**) Effects of proteasome inhibition on MDM2 and p53 levels. Immunoblot of control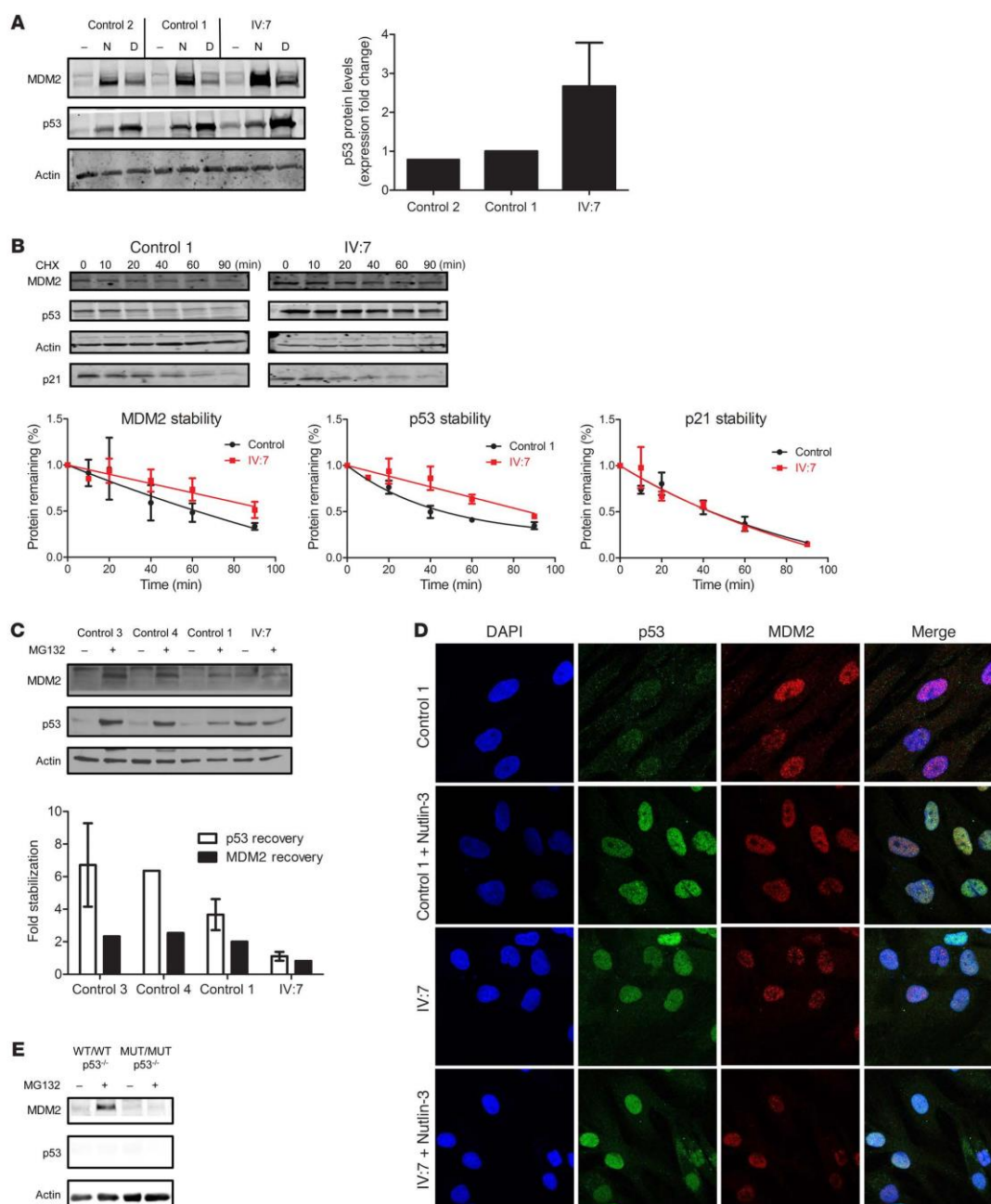 fibroblasts (controls 3, 4, and 1) and IV:7 fibroblasts treated with vehicle (DMSO) or MG132 (25 μM) for 6 hours. Graph shows protein quantification (using ImageJ) and normalization to actin. Fold recovery was calculated by comparing p53 or MDM2 values from treated cells with those of untreated cells. (**D**) Subcellular localization of MDM2 and p53 in control 1 and IV:7 fibroblasts treated with vehicle (DMSO) or Nutlin-3 (10 μM) for 24 hours. Original magnification, ×63. (**E**) U2OS genome-edited cells expressing WT/WT and MUT/MUT MDM2 with no p53 were treated with vehicle (DMSO) or the proteasome inhibitor MG132 (25 μM) for 6 hours before harvesting and immunoblotting. In **A** and **B**, error bars represent mean ± standard deviation. In **C**, error bars represent mean ± SEM.

JCI92171DS1). Two of his sisters, IV:3 and IV:5, were reported to have had similar clinical features. In more detail, individual IV:3 had short stature, prematurely gray hair, hypertension, and kidney failure and died at the age of 31 years from myocardial infarction. Individual IV:5 also had short stature and prematurely gray hair and died suddenly at the age of 23 years, possibly from an epileptic attack. Their parents, III:1 and III:2, died at an unknown age from myocardial infarction and respiratory infection, respectively. No DNA from the deceased individuals was available for genetic testing. Conventional Sanger sequencing revealed no mutation in the known disease genes for progeroid syndromes (24).

Identification of the causative mutation. To unravel the cause of this disorder with suspected autosomal-recessive inheritance, we first performed SNP array analysis of the index patient. In line with parental consanguinity, we identified 11 extended genomic regions of homozygosity with a maximum reachable LOD score (Supplemental Figure 1). We then performed whole-exome sequencing in patient IV:7. Bioinformatic filtering identified only a single homozygous variant not present in public databases that has a severe impact on protein structure in the above-mentioned putatively linked genomic regions (refer to the Supplemental text and Supplemental Table 2), namely, a homozygous antiterminating mutation, c.1492T>C, in *MDM2*. This mutation removes the physiological *MDM2* stop codon and is predicted to extend the protein for 5 further erroneous amino acids, p.*498Qext5 (amino acids: QLTCL, Figure 1C). Previous cell-based transfection studies have shown that the highly conserved extreme C-terminus of MDM2 is essential for its oligomerization and E3 ubiquitin ligase activity (25, 26). In addition, a more recent study showed that the same *MDM2* variant, when ectopically expressed, is unable to degrade coexpressed p53 in vitro (27).

Regulation of cellular p53 levels. To corroborate our genetic findings, we analyzed p53 levels in primary dermal fibroblasts from patient IV:7. When compared with fibroblasts from healthy control individuals, we observed both elevated basal p53 protein levels and pronounced induction of p53 protein in the patient's fibroblasts after treatment with 2 well-studied p53 inducers, i.e., Nutlin-3, a small-molecule inhibitor of MDM2-p53 interaction, and the anthracycline daunorubicin, a topoisomerase II inhibitor (Figure 2A). Markedly elevated p53 and MDM2 protein levels in lymphoblastoid cell lines (LCLs) from patient IV:7 as compared with LCLs from an unaffected individual confirmed these findings (Supplemental Figure 2A). Notably, p53 activation by Nutlin-3 treatment suggests that mutant MDM2 has residual p53 degradation activity. Taken together, these data indicate a compromised MDM2-p53 negative feedback loop as the likely pathogenic mechanism.

Consistent with the study mentioned above (27), we showed that ectopically expressed MDM2 with the antiterminating mutation is defective in its ability to degrade both ectopic and endogenous p53 in U2OS cells (Supplemental Figure 2, B and C). In fact, expression of mutant MDM2 led to increased levels of p53 protein in either case. Additionally, ectopic mutant MDM2 accumulated to markedly higher levels than did WT MDM2 when introduced into U2OS cells or H1299 cells (a p53-null cell line), indicating that its increased stability is an intrinsic property of the protein itself and not a result of p53 transcriptional activity (Supplemental Figure 2D). When conditions were calibrated such that mutant MDM2 and WT MDM2 were expressed at equivalent levels, mutant MDM2 still dramatically stabilized coexpressed p53 levels (Supplemental Figure 2E). These findings prompted us to further investigate MDM2-p53 homeostasis in fibroblasts from patient IV:7. Inhibition of protein synthesis by cycloheximide (CHX) revealed that both MDM2 and p53 were significantly stabilized compared with fibroblasts from an unaffected individual (Figure 2B), and the relative stabilities of transiently coexpressed mutant MDM2 and p53 were also markedly pronounced compared with WT MDM2 and p53 (Supplemental Figure 2F). Further, inhibition of the proteasome by MG132 confirmed the increased stability of p53 and MDM2 in the patient's fibroblasts, since their levels were just minimally increased after treatment as compared with levels in fibroblasts from unaffected individuals (Figure 2C). Together, these data indicate that the identified mutation leads to impaired MDM2 E3 ubiquitin ligase activity. This was confirmed by transient transfection experiments showing that p53 coexpressed with mutant MDM2 was underubiquitinated when compared with WT MDM2 (Supplemental Figure 2G) and, relatedly, that MG132 treatment only very modestly increased ectopic p53 levels in the presence of mutant MDM2 (Supplemental Figure 2H). Finally, immunocytochemistry revealed that the patient's untreated fibroblasts expressed relatively higher levels of nuclear p53, as was seen with fibroblasts from an unaffected individual treated with Nutlin-3 (Figure 2D). Transient transfection experiments again confirmed these observations, showing that p53 was found in both the nucleus and cytoplasm when coexpressed with WT MDM2 but was exclusively nuclear when coexpressed with mutant MDM2 (Supplemental Figure 2I).

In order to further analyze this mutation in a controlled background, we generated U2OS cell lines bearing 1 or 2 copies of mutant MDM2, heterozygous and homozygous, respectively, at its endogenous locus using TALENs. It is noteworthy that, despite the generation of multiple clones of other endogenous MDM2 mutations (data not shown), we were only able to obtain a single homozygous clone
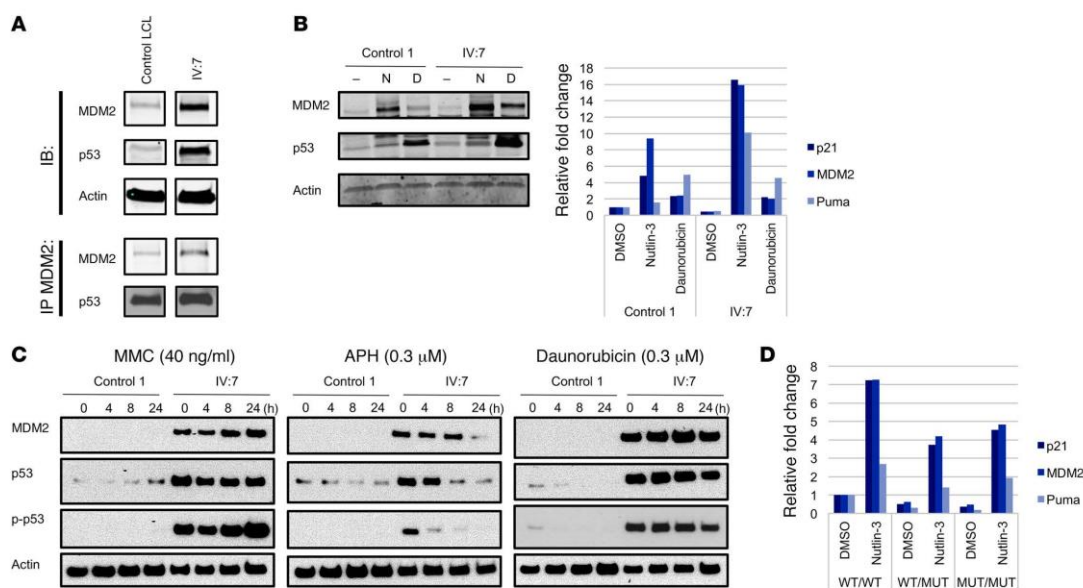
49

Figure 3. The antiterminating mutation results in abnormal p53 functional responses. (**A**) MDM2 and p53 could be coimmunoprecipitated. Proteins were harvested from control and IV:7 LCLs and detected after coimmunoprecipitation with anti-MDM2 antibody (H-221) and subsequent immunoblotting. All samples were run on the same gel but were noncontiguous. (**B**) Control 1 and IV:7 fibroblasts were treated for 24 hours with DMSO, Nutlin-3 and daunorubicin. Cells were harvested and used for protein or mRNA analysis. Cells were lysed and used for immunoblotting with the indicated antibodies. Quantitative reverse transcription PCR (qRT-PCR) analysis revealed relative mRNA levels of p53 target genes after treatment. Bar graph is representative of 3 independent experiments and shows no statistical significance. (**C**) Time course of p-p53, p53, and MDM2 protein levels after treatment with MMC, APH, and daunorubicin. Protein levels of p-p53 (Ser15), p53, and MDM2 in fibroblasts treated with MMC (40 ng/ml), APH (0.3 μM), or daunorubicin (0.1 μM). Fibroblasts from control 1 (lanes 1–4) and IV:7 (lanes 5–8) were treated for 24 hours with the indicated stressors. Cells were harvested either right after treatment (lanes 1 and 5), or were further cultured for 4 (lanes 2 and 6), 8 (lanes 3 and 7), or 24 hours (lanes 4 and 8) in stress-free medium. Cell lysates were used for immunoblotting with p-p53 (Ser15); p53 (AF1355); MDM2 (N20); and anti-actin. (**D**) qRT-PCR analysis showing relative mRNA levels of p53 target genes after treatment with DMSO or Nutlin-3 for 24 hours in WT/WT, WT/MUT, and MUT/MUT U2OS genome-edited cells. Bar graph is representative of 3 independent experiments and shows no statistical significance for Nutlin-3–treated p21 WT/MUT and MUT/MUT cell lines as compared with WT/WT cell lines.

expressing the antiterminating *MDM2* mutation, suggesting that cells expressing high levels of p53 could not be expanded during the selection process. In fact, basal and Nutlin-3–induced levels of p53 protein were similar among cells expressing WT/WT, WT/mutant (WT/MUT), and MUT/MUT MDM2 (Supplemental Figure 3), indicating that the genome-edited MUT/MUT MDM2 cells may have acquired a compensating mechanism to control basal p53 levels. To further determine the stability of mutant MDM2 in the absence of complications due to the presence of WT p53, we used CRISPR technology to generate p53-null versions in both parental and homozygous TALEN-generated cells (Figure 2E). Proteasome inhibition demonstrated that the MUT/MUT MDM2 could not be further stabilized when p53 was knocked out, suggesting that it is inherently more stable than its WT counterpart.

Cellular consequences of the MDM2 mutation. Since the primary sites of interaction between MDM2 and p53 are within their respective N-termini, we expected the mutant MDM2 to retain binding to p53. This was confirmed in the patient's LCLs (Figure 3A) and in cells ectopically expressing mutant MDM2 and p53 (Supplemental Figure 4). Therefore, it is likely that the mutant MDM2 still retains its ability to repress the transcriptional trans-

activation ability of p53 through direct binding (28), potentially explaining why this mutation does not lead to embryonic lethality in humans. However, we repeatedly observed that p53 in the patient's cells could still be highly activated by treatments that released p53 from MDM2 (Figure 2A), leading to a pronounced induction of the RNA expression levels of p53 target genes (p21, MDM2, NOXA, and PUMA) (Figure 3B). Notably, the mRNA induction of p53 target genes after Nutlin-3 treatment was markedly higher as compared with cells treated with daunorubicin. Although control and patient IV:7 fibroblasts expressed comparable total relative RNA levels upon daunorubicin treatment, the fold change upon daunorubicin induction varied between cell lines because of differing basal target gene expression. It is possible that the aging phenotype is mediated through pathways distinct from those activated by daunorubicin. Additionally, it is well known that the dynamic behavior of p53 varies on the basis of numerous factors such as the duration of the drug treatment and recovery period and the concentration of the drug used (29). In this experiment, we used a specific time point (24 hours) to investigate whether p53 could be activated in the patient's fibroblasts. To investigate this further, we used different stressors,
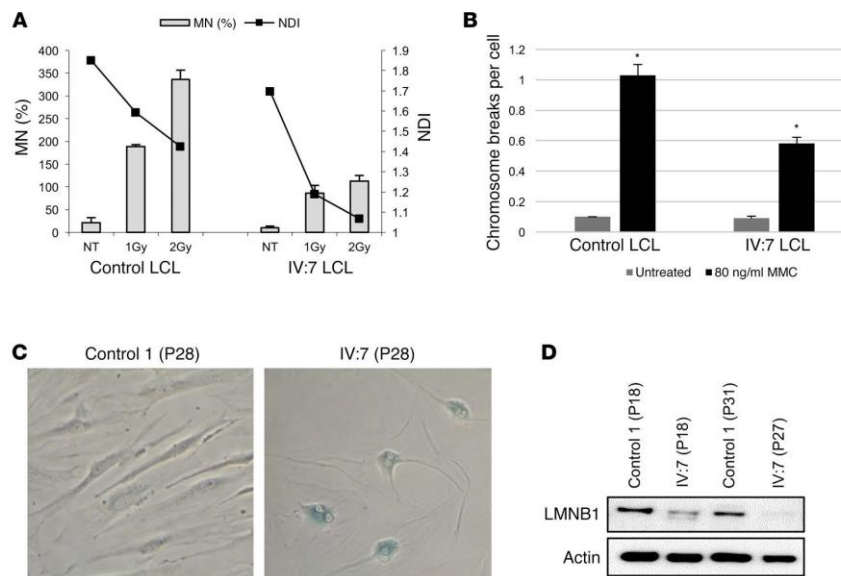
50

Figure 4. Functional consequences of the identified mutation in the patient's cells. (**A**) CBMN assays in LCLs. Effect of γ-irradiation (1 and 2 Gy) on the induction of micronuclei (MN) in control and IV:7 (left *y* axis) LCLs and on cell viability in the presence of CytB, indicated by the NDI (right *y* axis). Data represent 3 independent experiments. *P* = 0.2; 1 Gy: *P* = 0.0006; 2 Gy: *P* = 0.0001 (2-tailed Student's *t* test). NT, nontreated cells. (**B**) Chromosomal stability in LCLs. Graph shows the mean number of aberrations per cell observed in 100 metaphases of an unaffected individual (Control LCLs) and the index patient (IV:7 LCLs). LCLs were left untreated or treated with 80 ng/ml MMC for 48 hours. Data represent 2 independent experiments. *P* values are relative to control LCLs for each treatment. #*P* = 0.0002 (2-sample Poisson tests). (**C**) Senescence phenotype of IV:7 fibroblasts. Control 1 and IV:7 fibroblasts at passage 28 (P28) were stained for β-gal. Original magnification ×20. (**D**) Protein levels of LMNB1 and actin in primary fibroblasts from an unaffected individual (Control 1) and the index patient IV:7 at passages 18 (both), 31 (control 1), and 27 (index patient).

namely adriamycin, daunorubicin, mitomycin C (MMC), and aphidicolin (APH), and analyzed protein expression after different recovery periods (0, 4, 8, and 24 hours). Indeed, each treatment resulted in enhanced and prolonged p53 protein levels with concomitant p53 serine 15 phosphorylation in the patient's fibroblasts (Figure 3C and Supplemental Figure 5). Additionally, with the caveat that a single homozygous clone was used, our data with genome-edited cells also showed that p53 was hyperactivatable after Nutlin-3 treatment, as evidenced by a much greater fold increase over basal RNA levels expressed from a set of p53 target genes (Figure 3D). Also important, we found that basal expression of these p53 targets was markedly lower in homozygous MUT/MUT cells than in the parental cells, with mRNA expression in the heterozygous cells at intermediate levels (Figure 3D). Altogether, these data indicate that mutant MDM2 is able to bind and repress the transcriptional activity of basal p53, but upon stress leads to p53 hyperactivation.

These findings prompted us to perform chromosome breakage analysis and cytokinesis-block micronucleus (CBMN) assays, the latter of which enables simultaneous monitoring of genomic stability and cellular proliferation in LCLs under basal and stressed conditions. In contrast to many other segmental progeroid syndromes (30), LCLs from the index patient had no genomic instability but rather showed a certain level of protec-

tion against ionizing radiation and MMC, in accordance with the pronounced p53 stabilization after MMC treatment (Figure 4, A and B). This protection, however, seemed to occur at the cost of cell viability, as calculated by the nuclear division index (NDI) (Figure 4A), a finding compatible with a decreased regenerative capacity and the development of signs of accelerated aging on an organismal level. Additionally, the patient's fibroblasts had reduced replicative capacity and entered replicative senescence already at passage 28, whereas the control fibroblasts stopped replicating at passage 43, comparable to the findings in other progeroid syndromes (31). This was further confirmed by senescence-associated β-gal staining (Figure 4C) and loss of lamin B1 (LMNB1) (Figure 4D).

Impaired Mdm2 function in zebrafish. In order to confirm the impact of the identified *MDM2* mutation on cellular outcomes at a physiological level in vivo, we used an established zebrafish model. As expected from previous work (32), embryos either deficient in Mdm2 or overexpressing p53 displayed a severe apoptotic phenotype. This phenotype could be rescued upon coinjection of WT *mdm2* mRNA, but not by an equimolar amount of mutant *mdm2* mRNA bearing an extension of the 5 amino acids identified in the index patient (Figure 5). These findings confirmed the evolutionarily conserved role of the Mdm2 C-terminal tail and the pathogenic nature of the identified mutation.
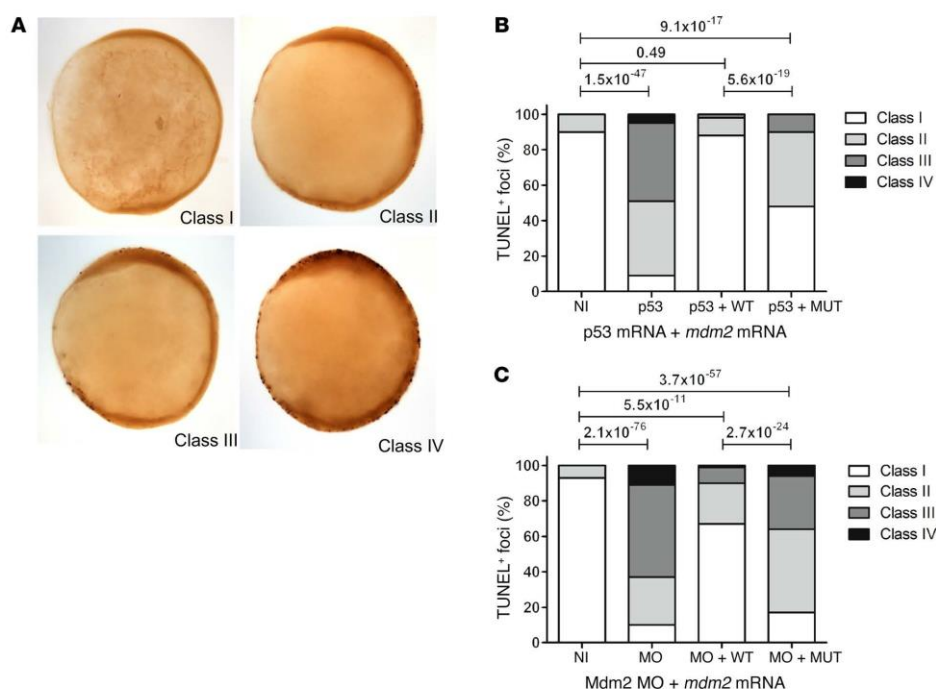
Figure 5. Impaired function of the antiterminating Mdm2 mutation in a zebrafish model. Complementation assay in 10 hpf zebrafish embryos (tailbud stage). (**A**) Representative images of the lateral view of 10 hpf zebrafish embryos stained with TUNEL. Embryos were classified by the number of TUNEL-positive foci as follows: class I (0–10); class II (10–20); class III (20–40); and class IV (>40). (**B** and **C**) Percentage of TUNEL-positive foci of various apoptosis classes of embryos injected with 3 ng Mdm2 morpholino and coinjections of 40 pg *mdm2* mRNAs and of embryos injected with p53 RNA and coinjections of 40 pg *mdm2* mRNAs (right panel). NI, noninjected embryos; MO, embryos injected with Mdm2 morpholino; p53, embryos injected with p53 mRNA; + WT, coinjection of *mdm2*-WT; + MUT, coinjection of *mdm2* bearing the antiterminating mutation. Data represent 3 independent experiments (2-sample Poisson tests).

Discussion

The human organism is under constant exposure to both endogenous and exogenous stressors, such as oxidative stress, environmental toxic substances, and UV light. If not dealt with, these threats can lead to DNA damage and cellular lesions that have the potential to harm the organism and limit survival. In order to cope with these pervasive threats, numerous cellular systems have evolved that can sensitively detect stressors and initiate adequate cellular responses to limit potential damage. In this respect, p53 plays an integrating and pivotal role in coordinating cellular reactions to stress signals, mainly by activating cell-cycle arrest, apoptosis, or senescence (2, 33). The beneficial role of p53 as a tumor suppressor and the consequences of loss of p53 activity in human cancers have been intensively studied. It therefore seems logical that upregulation of WT p53 could, in principle, represent an attractive therapeutic approach (34). Indeed, numerous studies report the identification of drugs that specifically target the MDM2/p53 axis for cancer therapy, with clinical trials already underway (35–37). Since the potential effects of increased p53 activation on an organismal level in humans are still unknown, the detailed elucidation of the possible effects of p53 activation on MDM2 inhibition is of growing biomedical importance. In this study, we have described the identification and characterization of a ger-

mline antiterminating *MDM2* mutation in a patient with a segmental progeroid syndrome. Although we describe a single patient and his family, the combination of (a) disease gene locus refinement by homozygosity mapping, (b) the systematic analysis of all homozygous variants by exome sequencing and, especially, (c) the demonstration of altered regulation of and by p53 in cells from this specific patient fulfill previously proposed criteria for identification of novel disease genes in single patients (38). Our studies indicate that dysfunctional regulation of p53 by MDM2 can lead to aberrant p53 activity that poses deleterious effects on human aging processes.

Until now, the strongest evidence linking aging and dysregulated p53 has come from engineered mouse models. Nonetheless, it is not a given that any genetic variant in mice will be phenocopied in humans. Two studies involving mice with N-terminal truncated p53 in the presence of functional WT p53 revealed accelerated aging phenotypes (19, 20). These mice appear to have aberrant MDM2 regulation of p53, and mouse embryonic fibroblasts from these mouse models express normal p53 protein levels but have constitutively active p53 (39). Further, mice with mutations in key N-terminal phosphorylation sites that can inhibit interaction with MDM2 also display an aging phenotype (40). Yet other studies have argued against a role for p53 in aging. In 1 case, super-p53–transgenic mice

52

harboring an extra copy of DNA spanning the p53 genomic locus appear to age normally (23). Similarly, mice that are hypomorphic for MDM2 have no signs of early aging (22), while other mice bearing extra copies of both p53 (super-p53) and ARF actually experience delayed onset of aging (41). Notably, the above-mentioned mice without signs of premature aging have intact p53/MDM2 circuitry, indicating that p53 in these mice is regulated by MDM2 normally. In contrast, the mutant p53 mice showing premature signs of aging collectively feature abnormal MDM2/p53 regulation due to mutant p53 alleles that cannot interact with MDM2. Relatedly, conditional mice with targeted deletion of *Mdm2* in the epidermis show characteristics of aging skin and have stable p53 (42).

Engineered mice with altered MDM2 have also greatly contributed to our understanding of the MDM2/p53 axis. Mice null for MDM2 expression or expressing a key MDM2 RING domain mutation that abrogates E3 ligase activity (p.Cys462Ala) display early embryonic lethal phenotypes unless the mice are generated in a p53-null background (43–45). These data indicate that MDM2 requires functional E3 ubiquitin ligase activity to restrain p53 for normal development. The extreme C-terminus of MDM2 plays a critical role in RING-RING interactions and is required for MDM2 oligomerization and E3 ligase activity in human cells (25, 26). Yet mice engineered with a mutation in the extreme C-terminus of MDM2 (p.Tyr487Ala) that also affects RING-RING interactions develop and age normally (46). Reports that defective E3 ligase activity due to mutations or extensions in the extreme C terminus of MDM2 can be partially rescued by coexpression of the MDM2 homolog MDMX could explain the viability of the Tyr487Ala mouse in comparison with the Cys462Ala mouse (25–27). However, since MDM2 variants with mutations in the last 5 amino acids of MDM2 share characteristic properties with those of antiterminating MDM2 mutations, it is surprising that the Tyr487Ala mouse does not display some segmental progeroid characteristics (25-27). We speculate that key differences between our index patient and Tyr487Ala mice could account for the different phenotypes. Specifically, the enhanced MDM2 stability, levels of basal p53 target genes, and hyperactivation of the p53 transcriptional program in the patient's cells differ from the reported characteristics of the Tyr487Ala mouse. Additionally, laboratory mice could be spared exposure to many naturally occurring stresses or environmental stimuli, which could be important cofactor(s) in the normal or pathological aging process.

We postulate that either the ability of p53 to be hyperactivated or its prolonged activation due to the impaired ability of the antiterminating mutant MDM2 in downregulating p53 after stress might be critical factors contributing to the observed clinical phenotype in the index patient. Thus, we hypothesize that in the index patient, certain everyday stresses generate a chronic condition, whereby pervasive and pronounced deleterious activation of p53 downstream targets induces a program of accelerated aging. Indeed, elevated levels of p53 with concomitant activation of the p53 pathway have been previously identified in several other segmental progeroid syndromes, such as ataxia telangiectasia, Hutchinson-Gilford progeria, and Cockayne syndrome (18, 21, 47). Further, we should consider the possibility that basally underexpressed p53 target genes in the patient-derived and engineered cells are also contributing to one or more of the characteristics of the patient, as basal p53 has been implicated in survival functions and regulation

of longevity-associated processes (3). In addition, p53 crosstalk with other pathways adds another layer of complexity to delineating the underlying mechanism(s) linking p53 and aging (48–50). Nor can we exclude the possibility that p53-independent activities of MDM2 might also contribute to the observed phenotype (6, 51).

Indeed, p53 activation is stressor dependent and may lead to abnormally enhanced levels of autophagy, cell-cycle arrest, apoptosis, or senescence that can ultimately cause tissue and organ dysfunction resulting in accelerated aging symptoms (52). Two common hallmarks in both segmental forms of progeria and physiological aging are genomic instability and cellular senescence (49, 53). However, unlike the situation in other progeroid syndromes that derive from defects in genome maintenance proteins and thus exhibit diminished genomic integrity, we observed increased chromosomal stability in the patient's cells. The latter is largely in accordance with prolonged p53 hyperactivation, which could potentially promote DNA repair mechanisms and enhance genome stability (3). On the other hand, we observed premature senescence in the patient's fibroblasts. Although we acknowledge that it is almost impossible to exactly define which of the numerous cellular outcomes contribute to the progeroid phenotype, as the p53 response is cell-, tissue-, and stress-type dependent, our data implicate senescence as playing a role in facilitating the aging symptoms in the patient.

In the family studied here, idiopathic, early-onset kidney failure followed by arterial hypertension and the family's predisposition to myocardial infarction seem to be the most malicious outcomes at the organismal level. Intriguingly, in addition to being essential for maintenance of the nephron progenitor niche (53), studies in mice have suggested that the MDM2/p53 axis specifically regulates kidney-specific cell healing, development, and the response to inflammation (54, 55). Our data, even though based on a single patient, may indicate a potentially increased risk of side effects for systemic, long-term therapies with MDM2 inhibitors. Special emphasis on the parameters of kidney function may therefore be advisable for the clinical trials already underway involving synthetic small molecules that interfere with MDM2-p53 interaction.

In summary, we report on a patient who developed — at a rather early age — several symptoms that are typically observed in the elderly, compatible with the diagnosis of a segmental progeroid syndrome (56). By combining up-to-date genetic approaches including genome-wide linkage mapping and massively parallel sequencing with in-depth functional characterization of patient-derived primary cell lines with complementary in vitro and in vivo analyses, we identified a homozygous germline antiterminating *MDM2* mutation as the genetic cause of his condition. Taken together, our evidence provides strong support for a role for functional disturbance of the MDM2/p53 axis in promoting a premature aging phenotype in humans.

Methods

Cell lines. EBV-transformed LCLs and primary dermal fibroblasts were established as previously described (57). Previously used LCLs from an unaffected individual, AG1010 (24), termed control LCLs, were used in all experiments. In experiments with primary dermal fibroblasts, a previously used cell line from a healthy individual, 82-6 (30), termed control fibroblasts 1, was used for all experiments. To corroborate the findings in some experiments, additional cell lines

from unaffected individuals (IMR-90, NHDF, and 1101-SK) were used and are termed control fibroblasts 2, 3, and 4, respectively. 88-1 normal fibroblasts were also used. Primary dermal fibroblasts were maintained in DMEM supplemented with 10% FBS. Human osteosarcoma (U2OS) and non–small-cell lung cancer (H1299) cell lines were also maintained in DMEM supplemented with 10% FBS. LCLs were maintained in RPMI medium supplemented with 10% FBS. Cell lines were obtained from Junko Oshima, Lyubomir Vassilev (Serono Research and Development Institute, Billerica, MA, USA), and ATCC. For replicative capacity studies, primary dermal fibroblasts from the index patient and control fibroblasts 1 were thawed at passage 6 and passaged at 80% confluency. Fibroblasts were not allowed to become fully confluent at any time in order to maintain maximal growth rates.

Homozygosity mapping and candidate gene sequencing. Genome-Wide Human SNP Array 6.0 (Affymetrix) was used to exclude the possibility of genomic rearrangements and map putative homozygous regions. Genome-wide homozygosity scores were produced by HomozygosityMapper, a Web-based approach to homozygosity mapping (58). Data handling, evaluation, and statistical analysis were previously described in detail (30). To confirm the homozygous antiterminating mutation, c.1492T>C, in *MDM2*, we designed primers, 5′- gagggcttt-gatgttcctga-′3 and 5′-ggagttggtgtaaaggatgagc-′3, and PCR amplified it by using genomic DNA from the affected individual. PCR products were sequenced on an ABI 3730 DNA Analyzer with BigDye Chemistry, version 3.1 (Applied Biosystems). Sequence traces were assembled, aligned, and analyzed with Seqman software (DNASTAR Lasergene).

Exome-sequencing analysis. Exome sequencing of the proband was performed on 2 lanes of an Illumina GAIIx Sequencer using a single-read 150-bp protocol after enrichment of exonic and splice-site sequences with the Agilent SureSelect Human All Exon 50 Mb Kit. More than 194 million reads were mapped to the hg19 human reference genome. Approximately 93% of target sequences had at least 10-fold coverage and 75% had 30-fold coverage, with a mean coverage of approximately 91. Data analysis of filter-passed reads was performed with the in-house pipeline V1.3 using BWA-short in combination with SAMTOOLS pileup 0.1.7 for the detection of SNPs and short insertions and deletions (indels). In-house-developed scripts were applied to detect protein changes, affected splice sites, and overlaps to known variations, with filtering against dbSNP build 138, the 1000 Genomes Project data build November 2014, ExAC Browser (status from April 2015), and the in-house database of exome variants (with data from >200 exomes of individuals affected by different disorders). The criteria for a variation to be taken into account were: more than 6 reads; a phred scaled quality score of greater than 15; a population allele frequency of less than 1% seen fewer than 10 times in our in-house database; and more than 15% of the reads supporting the allele.

Plasmids. Full-length zebrafish *mdm2* and p53 and human *MDM2* cDNAs were cloned into pCS2+ and pcDNA3.1 (Invitrogen, Thermo Fisher Scientific), respectively. Mutants were cloned using PCR amplification and restriction enzyme digestion and recombination. Site-directed mutagenesis was performed by PCR to introduce the desired mutations. The correctness of the DNA sequence was verified by sequencing.

Genome-edited cell lines. Two TALEN plasmids were designed to target nucleotides within the intron between exons 10 and 11 (**taccttag-acata**gcaaa[G]ttgctagcatt**cctgtgactgagcagtta**, where [G] indicates a TALEN cutting site, and the 2 TALEN binding sites are underlined bold), as recommended by ZiFiT Targeter software (http://zifit.partners.org/ZiFiT/TALZiFiTNuclease.aspx). A donor vector with two 1-kb homolo-

gous arms plus an FNF selection cassette (Frt-EM7- NeoR-Frt) was also constructed. The FNF selection cassette was inserted into the intron between exons 10 and 11 of the *mdm2* gene to facilitate clone selection as well as a unique HindIII site in exon 11. A *T* to *C* mutation was introduced into the donor vector at the stop codon TGA by site-directed mutagenesis. This resulted in an MDM2 variant with a 5–amino acid extension. The donor and TALEN plasmids were transfected into U2OS cells, followed by selection with G418 (800 µg/ml) for 2 to 3 weeks. The resistant clones were expanded and examined for FNF insertion on the *mdm2* locus by PCR. The corrected clones were confirmed by sequencing to ensure that the allele carrying the mutation was corrected. Both heterozygous and homozygous clones were obtained. To serve as controls, isogenic WT clones were also obtained through the same selection process.

Mutant MDM2-p53-KO cells were generated using CRISPR/Cas9 genome editing technology. Cells (7×10^5) were transfected with 2 µg p53 CRISPR/Cas9-KO plasmid (Santa Cruz Biotechnology Inc.). Two days later, cells were treated with Nutlin-3 (10 µM) for six days to inhibit the proliferation of cells with WT p53, thereby enriching for p53-KO cells. Single-cell clones were selected via limiting dilution, and p53-KO clones were confirmed by Western blotting using FL-393 (Santa Cruz Biotechnology Inc.) rabbit polyclonal antibody.

Immunoblotting. Whole-cell lysates were analyzed by standard immunoblotting procedures. Protein concentration was measured using the Bio-Rad protein assay (Life Science Research). Equal amounts of total protein were resolved on 8% or 12% polyacrylamide gels (for ectopic and fibroblast/LCL work, respectively), transferred to a nitrocellulose membrane, and then blocked for 30 minutes in PBS containing 0.1% Tween-20 (PBST) (Sigma-Aldrich) and 5% nonfat dry milk. The membrane was incubated overnight at 4°C with primary antibodies in 1% milk in PBST. The commercial primary antibodies used include: anti-FLAG (M2; Sigma-Aldrich); anti-HA (6B12; Covance); anti-p53 (AF1355; R&D Systems); anti-MDM2 (N20 or H-221; Santa Cruz Biotechnology Inc.); anti–phosphorylated p53 (anti-p-p53) (Ser15) (Cell Signaling Technology); anti-lamin B1 (S20; Santa Cruz Biotechnology Inc.); anti-p21 (C-19; Santa Cruz Biotechnology Inc.); anti-GFP (B2; Santa Cruz Biotechnology Inc.); anti–γ-tubulin (T5192; Sigma-Aldrich); and anti-actin (A2066; Sigma-Aldrich). The monoclonal antibodies used as in-house–produced hybridoma supernatants include: anti-p53 (1801/DO-1) and anti-MDM2 (2A9, 3G5, 4B11, and 5B10). After 3 washes with PBST, membranes were incubated with secondary antibodies in 1% milk in PBST for 30 minutes at room temperature (RT). The secondary antibodies used include goat anti-mouse or goat anti-rabbit conjugated to HRP (Sigma-Aldrich) or fluorescent green goat anti-mouse and fluorescent red donkey anti-rabbit (IRDye 800CW and IRDye 680LT; LI-COR Biosciences). Membranes were visualized using either ECL (GE Healthcare or Thermo Fisher Scientific) or the Odyssey Imaging System (LI-COR Biosciences).

Drugs. The following drugs were used: Nutlin-3 (a racemic mixture of active Nutlin-3a and inactive Nutlin-3b; Sigma-Aldrich); CHX (Calbiochem); daunorubicin (Sigma-Aldrich); MG132 (Calbiochem); MMC (Sigma-Aldrich); cytochalasin B (CtyB) (Sigma-Aldrich); APH (Sigma-Aldrich); and adriamycin (Sigma-Aldrich).

Immunofluorescence analyses. U2OS, control 1, and IV:7 primary fibroblasts were grown on coverslips in 35-mm Petri dishes. Cells were washed twice with PBS and fixed with 4% paraformaldehyde solution in PBS for 20 minutes at RT. Following 2 additional washes, fixed cells were permeabilized with 0.5% Triton X-100 in PBS at RT

54

for 1.5 minutes, washed twice, blocked with 0.5% BSA in PBS for 30 minutes at RT, incubated with primary antibodies at RT for 1 hour in blocking solution, washed thrice, incubated with a mixture of secondary antibodies conjugated with fluorescent dye (Alexa Fluor 488 and Alexa Fluor 594; Life Technologies, Thermo Fisher Scientific) at RT for 1 hour in the dark, washed thrice, and then mounted with VECTA-SHIELD mounting medium for fluorescence with DAPI (Vector Laboratories). The following primary antibodies were used: anti-MDM2 N20 (Santa Cruz Biotechnology Inc.); anti-p53 1801/DO-1 (produced in-house); anti-HA (16B12; Covance); and anti-FLAG (M2; Sigma-Aldrich). Images were taken on a Zeiss LSM 700 confocal microscope.

Quantitative reverse transcription PCR. RNA was isolated from cultured cells using the RNeasy Mini Kit (QIAGEN) and then converted into cDNA using the QuantiTect Reverse Transcription Kit (QIAGEN). PCR was performed using the StepOne Real-time PCR system with Power SYBR Green PCR Master Mix (Applied Biosystems). Relative mRNA levels were calculated by the $\Delta\Delta$Ct method and normalized against control *L32* mRNA levels.

Cytokinesis-block micronucleus assay. The CBMN assay was performed with cells from patient IV:7 and AG 1011 cells. Cells (2.5 million) were cultivated in 10 ml RPMI medium irradiated with 1 Gy or 2 Gy γ rays using a Cs-137 source (Gammacell 2000; Nuclear Data). After irradiation, CytB was added to the cultures at a final concentration of 2 μg/ml. Cultures were harvested 41 hours later by centrifugation, treated with a hypotonic solution (0.56% KCl), and fixed once with methanol/glacial acetic acid (5 + 1) mixed with an equal amount of 0.9% NaCl. Cells were then fixed 3 times with methanol/glacial acetic acid (5 + 1). Air-dried slides were stained with acridine orange (60 μg/ml in phosphate buffer). The frequency of micronucleated cells was determined by analyzing 1,000 binuclear cells from coded slides. Toxicity was measured using the nuclear division index (NDI), which was calculated from 500 cells according to the formula: NDI = $(M1 + 2M2 + 3M3 + 4M4 + 5M5)/N$, where M1 – M5 indicates the number of cells with 1 to 5 nuclei and N the total number of cells scored.

Chromosome analysis. Exponentially growing LCLs were reseeded into culture flasks at a density of 2×10^5/ml, left untreated for an additional 24 hours, or incubated with 80 ng/ml MMC for 48 hours. Cells were exposed to 100 ng/ml colcemid for 2 hours, treated with hypotonic solution (NaCl/sodium-citrate, 0.4 %) for 15 minutes, and fixed with 3:1 methanol/acetic acid. Slides were stained with Giemsa, and 100 metaphase spreads were scored for chromosomal aberrations in 2 independent experiments. Metaphase spreads were observed using a Leitz Laborlux S microscope and captured using CytoVision (Applied Imaging). Data for chromosomal breaks in LCLs were compared (untreated and MMC-treated) using Poisson regressions with log link functions, with the number of observed metaphases as an offset variable. AG1010 LCLs served as the reference. *P* values were not adjusted for multiple testing.

Detection of senescence-associated β-gal activity. Endogenous mammalian senescence-associated β-gal activity (SAβ-gal) was evaluated using the Senescence β-Galactosidase Staining Kit (Cell Signaling Technology) according to the manufacturer's guidelines.

Zebrafish maintenance and manipulation. WT Tupfel long fin (TL) zebrafish were maintained following standard protocols. *mdm2* RNA (3 ng) antisense morpholino oligonucleotides (MO) or 40 pg capped RNA, transcribed with the mMessage mMachine Kit (Ambion) from linearized plasmids, were injected into the blastodisc prior to the first cleavage. Embryos were kept at 28.5°C up to the tailbud stage (10 high-power

fields [hpf]) and analyzed and processed. Concentrations of injected MO and RNA were calculated, and volumes were adjusted in mineral oil for reproducible injection volumes prior to microinjections. RNA quality was analyzed prior to injections by using 1.5% agarose gel electrophoresis. Phenol red (0.5%) and rhodamine-dextrane (0.5%) were coinjected in order to monitor the equal distribution of the solution during injection. Six hours after injection, embryos were sorted for homogeneity of the injected solution using a fluorescence stereoscope. A previously established splice-site *mdm2* MO (5′-TGTTAAGAGATTCAGTACGCAC-CGC-3′) (59) was used to generate loss-of-function zebrafish. Detection of apoptotic cells by TUNEL staining at 10 hpf was performed using the In Situ Cell Death Detection Kit (Roche) as described previously (60).

Statistics. Statistical evaluation was performed depending on the experiment by using a 2-tailed Student's *t* test or 2-sample Poisson tests, as specifically indicated for each experiment in the figure legends. A *P* value of less than 0.05 was considered significant.

Study approval. All biological samples and photographs were obtained following written informed consent from the patient. The International Registry of Werner Syndrome has been recruiting patients suspected of Werner syndrome since 1988. The study has ongoing approval from the IRB of the University of Washington. This study was performed in accordance with Declaration of Helsinki protocols.

Author contributions

Acknowledgments

Address correspondence to: Christian Kubisch, Institute of Human Genetics, University Medical Center Hamburg-Eppendorf, Martinistrasse 52, 20246 Hamburg, Germany. Phone: 49.40.7410.52120; Email: c.kubisch@uke.de. Or to: Carol Prives, Department of Biological Sciences, Columbia University, 1212 Amsterdam Avenue, 816 Fairchild Building, New York, New York 10027, USA. Phone: 212.854.2557; Email: clp3@columbia.edu.

TR's present address is: MRC Centre for Inflammation Research, Queen's Medical Research Institute, University of Edinburgh, Edinburgh, United Kingdom.

YZ's present address is: Department of Biological Sciences, St. John's University, Queens, New York, USA.

1. Malkin D, et al. Germ line p53 mutations in a familial syndrome of breast cancer, sarcomas, and other neoplasms. *Science*. 1990;250(4985):1233–1238.
2. Vogelstein B, Lane D, Levine AJ. Surfing the p53 network. *Nature*. 2000;408(6810):307–310.
3. Vousden KH, Prives C. Blinded by the light: the growing complexity of p53. *Cell*. 2009;137(3):413–431.
4. Krizhanovsky V, Lowe SW. Stem cells: The promises and perils of p53. *Nature*. 2009;460(7259):1085–1086.
5. Lee JT, Gu W. The multiple levels of regulation by p53 ubiquitination. *Cell Death Differ*. 2010;17(1):86–92.
6. Wade M, Wang YV, Wahl GM. The p53 orchestra: Mdm2 and Mdmx set the tone. *Trends Cell Biol*. 2010;20(5):299–309.
7. Wu X, Bayle JH, Olson D, Levine AJ. The p53-mdm-2 autoregulatory feedback loop. *Genes Dev*. 1993;7(7A):1126–1132.
8. Barak Y, Juven T, Haffner R, Oren M. mdm2 expression is induced by wild type p53 activity. *EMBO J*. 1993;12(2):461–468.
9. Vousden KH, Lane DP. p53 in health and disease. *Nat Rev Mol Cell Biol*. 2007;8(4):275–283.
10. Zhang B, Golding BT, Hardcastle IR. Small-molecule MDM2-p53 inhibitors: recent advances. *Future Med Chem*. 2015;7(5):631–645.
11. Kulju KS, Lehman JM. Increased p53 protein associated with aging in human diploid fibroblasts. *Exp Cell Res*. 1995;217(2):336–345.
12. Feng Z, Hu W, Teresky AK, Hernando E, Cordon-Cardo C, Levine AJ. Declining p53 function in the aging process: a possible mechanism for the increased tumor incidence in older populations. *Proc Natl Acad Sci U S A*. 2007;104(42):16633–16638.
13. Ørsted DD, Bojesen SE, Tybjaerg-Hansen A, Nordestgaard BG. Tumor suppressor p53 Arg72Pro polymorphism and longevity, cancer survival, and risk of cancer in the general population. *J Exp Med*. 2007;204(6):1295–1301.
14. Bergamaschi D, et al. iASPP preferentially binds p53 proline-rich region and modulates apoptotic function of codon 72-polymorphic p53. *Nat Genet*. 2006;38(10):1133–1141.
15. Dumont P, Leu JI, Della Pietra AC, George DL, Murphy M. The codon 72 polymorphic variants of p53 have markedly different apoptotic potential. *Nat Genet*. 2003;33(3):357–365.
16. van Heemst D, et al. Variation in the human TP53 gene affects old age survival and cancer mortality. *Exp Gerontol*. 2005;40(1-2):11–15.
17. Scaffidi P, Misteli T. Lamin A-dependent nuclear defects in human aging. *Science*. 2006;312(5776):1059–1063.
18. Varela I, et al. Accelerated ageing in mice deficient in Zmpste24 protease is linked to p53 signalling activation. *Nature*. 2005;437(7058):564–568.
19. Tyner SD, et al. p53 mutant mice that display early ageing-associated phenotypes. *Nature*. 2002;415(6867):45–53.
20. Maier B, et al. Modulation of mammalian life span by the short isoform of p53. *Genes Dev*. 2004;18(3):306–319.
21. Liu D, et al. Puma is required for p53-induced depletion of adult stem cells. *Nat Cell Biol*. 2010;12(10):993–998.
22. Mendrysa SM, et al. Tumor suppression and normal aging in mice with constitutively high p53 activity. *Genes Dev*. 2006;20(1):16–21.
23. García-Cao I, et al. "Super p53" mice exhibit enhanced DNA damage response, are tumor resistant and age normally. *EMBO J*. 2002;21(22):6225–6235.
24. Lessel D, et al. POLD1 Germline Mutations in Patients Initially Diagnosed with Werner Syndrome. *Hum Mutat*. 2015;36(11):1070–1079.
25. Poyurovsky MV, et al. The Mdm2 RING domain C-terminus is required for supramolecular assembly and ubiquitin ligase activity. *EMBO J*. 2007;26(1):90–101.
26. Uldrijan S, Pannekoek WJ, Vousden KH. An essential function of the extreme C-terminus of MDM2 can be provided by MDMX. *EMBO J*. 2007;26(1):102–112.
27. Dolezelova P, Cetkovska K, Vousden KH, Uldrijan S. Mutational analysis of Mdm2 C-terminal tail suggests an evolutionarily conserved role of its length in Mdm2 activity toward p53 and indicates structural differences between Mdm2 homodimers and Mdm2/MdmX heterodimers. *Cell Cycle*. 2012;11(5):953–962.
28. Momand J, Zambetti GP, Olson DC, George D, Levine AJ. The mdm-2 oncogene product forms a complex with the p53 protein and inhibits p53-mediated transactivation. *Cell*. 1992;69(7):1237–1245.
29. Purvis JE, Karhohs KW, Mock C, Batchelor E, Loewer A, Lahav G. p53 dynamics control cell fate. *Science*. 2012;336(6087):1440–1444.
30. Lessel D, et al. Mutations in SPRTN cause early onset hepatocellular carcinoma, genomic instability and progeroid features. *Nat Genet*. 2014;46(11):1239–1244.
31. Tivey HS, Brook AJ, Rokicki MJ, Kipling D, Davis T. p38 (MAPK) stress signalling in replicative senescence in fibroblasts from progeroid and genomic instability syndromes. *Biogerontology*. 2013;14(1):47–62.
32. Langheinrich U, Hennen E, Stott G, Vacun G. Zebrafish as a model organism for the identification and characterization of drugs and genes affecting p53 signaling. *Curr Biol*. 2002;12(23):2023–2028.
33. Bieging KT, Mello SS, Attardi LD. Unravelling mechanisms of p53-mediated tumour suppression. *Nat Rev Cancer*. 2014;14(5):359–370.
34. Khoo KH, Hoe KK, Verma CS, Lane DP. Drugging the p53 pathway: understanding the route to clinical efficacy. *Nat Rev Drug Discov*. 2014;13(3):217–236.
35. Zhang Q, Zeng SX, Lu H. Targeting p53-MDM2-MDMX loop for cancer therapy. *Subcell Biochem*. 2014;85:281–319.
36. Andreeff M, et al. Results of the Phase I Trial of RG7112, a Small-Molecule MDM2 Antagonist in Leukemia. *Clin Cancer Res*. 2016;22(4):868–876.
37. Wagner AJ, et al. Phase I trial of the human double minute 2 inhibitor MK-8242 in patients with advanced solid tumors. *J Clin Oncol*. 2017;35(12):1304–1311.
38. Casanova JL, Conley ME, Seligman SJ, Abel L, Notarangelo LD. Guidelines for genetic studies in single patients: lessons from primary immunodeficiencies. *J Exp Med*. 2014;211(11):2137–2149.
39. Moore L, Lu X, Ghebranious N, Tyner S, Donehower LA. Aging-associated truncated form of p53 interacts with wild-type p53 and alters p53 stability, localization, and activity. *Mech Ageing Dev*. 2007;128(11-12):717–730.
40. Donehower LA. Using mice to examine p53 functions in cancer, aging, and longevity. *Cold Spring Harb Perspect Biol*. 2009;1(6):a001081.
41. Matheu A, et al. Delayed ageing through damage protection by the Arf/p53 pathway. *Nature*. 2007;448(7151):375–379.
42. Gannon HS, Donehower LA, Lyle S, Jones SN. Mdm2-p53 signaling regulates epidermal stem cell senescence and premature aging phenotypes in mouse skin. *Dev Biol*. 2011;353(1):1–9.
43. Itahana K, et al. Targeted inactivation of Mdm2 RING finger E3 ubiquitin ligase activity in the mouse reveals mechanistic insights into p53 regulation. *Cancer Cell*. 2007;12(4):355–366.
44. Jones SN, Roe AE, Donehower LA, Bradley A. Rescue of embryonic lethality in Mdm2-deficient mice by absence of p53. *Nature*. 1995;378(6553):206–208.
45. Montes de Oca Luna R, Wagner DS, Lozano G. Rescue of early embryonic lethality in mdm2-deficient mice by deletion of p53. *Nature*. 1995;378(6553):203–206.
46. Tollini LA, Jin A, Park J, Zhang Y. Regulation of p53 by Mdm2 E3 ligase function is dispensable in embryogenesis and development, but essential in response to DNA damage. *Cancer Cell*. 2014;26(2):235–247.
47. Latini P, et al. CSA and CSB proteins interact with p53 and regulate its Mdm2-dependent ubiquitination. *Cell Cycle*. 2011;10(21):3719–3730.
48. López-Otín C, Blasco MA, Partridge L, Serrano M, Kroemer G. The hallmarks of aging. *Cell*. 2013;153(6):1194–1217.
49. Poyurovsky MV, Prives C. P53 and aging: A fresh look at an old paradigm. *Aging (Albany NY)*. 2010;2(7):380–382.
50. Campisi J. Fragile fugue: p53 in aging, cancer and IGF signaling. *Nat Med*. 2004;10(3):231–232.
51. Li Q, Lozano G. Molecular pathways: targeting Mdm2 and Mdm4 in cancer therapy. *Clin Cancer Res*. 2013;19(1):34–41.
52. Horn HF, Vousden KH. Coping with stress: multiple ways to activate p53. *Oncogene*. 2007;26(9):1306–1316.
53. Hilliard SA, Yao X, El-Dahr SS. Mdm2 is required for maintenance of the nephrogenic niche. *Dev Biol*. 2014;387(1):1–14.
54. Mulay SR, Thomasova D, Ryu M, Anders HJ. MDM2 (murine double minute-2) links inflammation and tubular cell healing during acute kidney injury in mice. *Kidney Int*. 2012;81(12):1199–1211.
55. El-Dahr S, Hilliard S, Aboudehen K, Saifudeen Z. The MDM2-p53 pathway: multiple roles in kidney development. *Pediatr Nephrol*. 2014;29(4):621–627.
56. Martin GM. Genetic syndromes in man with potential relevance to the pathobiology of aging. *Birth Defects Orig Artic Ser*. 1978;14(1):5–39.
57. Huang S, et al. The spectrum of WRN mutations in Werner syndrome patients. *Hum Mutat*. 2006;27(6):558–567.
58. Seelow D, et al. HomozygosityMapper—an interactive approach to homozygosity mapping. *Nucleic Acids Res*. 2009;37(Suppl 2):W593–W599.
59. Parant JM, George SA, Holden JA, Yost HJ. Genetic modeling of Li-Fraumeni syndrome in zebrafish. *Dis Model Mech*. 2010;3(1-2):45–56.
60. Cole LK, Ross LS. Apoptosis in the developing zebrafish embryo. *Dev Biol*. 2001;240(1):123–142.

56

Supplemental Material for:

Constitutive dysfunction of the Mdm2-p53 axis is linked to premature signs of aging

Authors:
Davor Lessel[1*], Danyi Wu[2*], Carlos Trujillo[3], Thomas Ramezani[4#], Ivana Lessel[1], Mohammad K. Alwasiyah[5], Bidisha Saha[6], Fuki M. Hisama[7], Katrin Rading[1], Ingrid Goebel[1], Petra Schütz[8], Günter Speit[8], Josef Högel[8], Holger Thiele[9], Gudrun Nürnberg[9], Peter Nürnberg[9,10,11], Matthias Hammerschmidt[4,10,11], Yan Zhu[2], David Tong[2], Chen Katz[2], George M. Martin[6,12], Junko Oshima[6,13], Carol Prives[2$], Christian Kubisch[1,8$]

[*]These authors contributed equally to the work.

[$]Correspondence should be addressed to C.K. (c.kubisch@uke.de) or C.P. (clp3@columbia.edu)

1

Supplemental Text

Bioinformatic filtering of exome sequencing data

Due to the parental consanguinity, we searched for a gene harbouring a very rare or unique homozygous variant with a severe impact on protein structure within the putative linkage regions. We excluded a possible pathogenicity of missense variants in *TRIM45*, *CD48*, *PEX1*, *DGKA*, *INHBC* and *CACNA1G* due to their low evolutionary conservation and the fact that they were predicted benign by Polyphen2 (http://genetics.bwh.harvard.edu/pph2/index.shtml). Mutations in *MYO1A* were initially reported to cause an autosomal dominant form of hearing impairment (1) a symptom which is not present in the index patient. Recently, the pathogenicity of heterozygous *MYO1A* mutations was challenged and it was demonstrated that even homozygous loss of function mutations in *MYO1A* do not cause any overt phenotype (2) so that we also excluded the observed variant in this gene as potentially disease causing. *MCM6*, *TIMELESS* and *BRCA1* are involved in the maintenance of genomic stability and are thus predicted to lead to chromosomal instability if mutated, at least after treatment with replication-related stressors (3-5). We therefore also excluded variants in these genes as we did not observe genomic instability in primary cell lines of index patient but rather the contrary, i.e. protection against chromosomal instability. In addition, the identified variants in *BRCA1* seem to be rather common polymorphisms in Saudi Arabia (6). *GDE1* knock-out mice (MGI:1891827) are viable and do not display any overt abnormalities apart from reduced glycero-phospho-N-acyl ethanolamine (GP-NAE) phosphodiesterase activity in the brain. Moreover, these mice do not display any signs of premature aging (7). We therefore also excluded the possibility that the variant in *GDE1* may add to the phenotype observed in the index patient. *ARHGAP23* is a still uncharacterized, putative Rho GTPase activating protein of unknown function. Thus, we cannot fully exclude the possibility that the identified variant in this gene may contribute to the observed phenotype. However, the proven dysregulation of the Mdm2-p53 in patient cell lines and the additional functional data presented here strongly suggest that the anti-terminating *MDM2* mutation is responsible for most, if not all of the phenotypes observed in the index patient. Moreover, the *MDM2* mutation was the only alteration with a severe impact on protein structure.

2
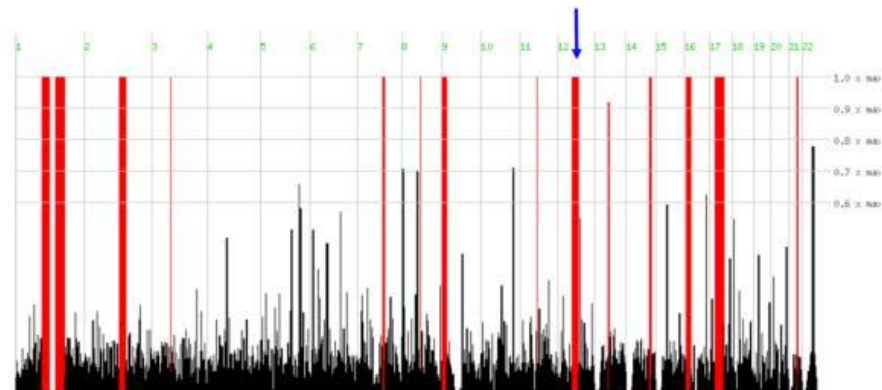
Supplemental Figure S1. Genome-wide homozygosity mapping. Shows the genome-wide homozygosity scores produced by HomozygosityMapper, using 867,266 selected SNP markers from the Affymetrix SNP Array 6.0. These are plotted against the physical position and as a bar chart with red bars indicating the most promising genomic regions. Note 13 extended genomic regions of maximal homozygosity scores. Blue arrow indicates position of MDM2, in one of the largest regions.

3
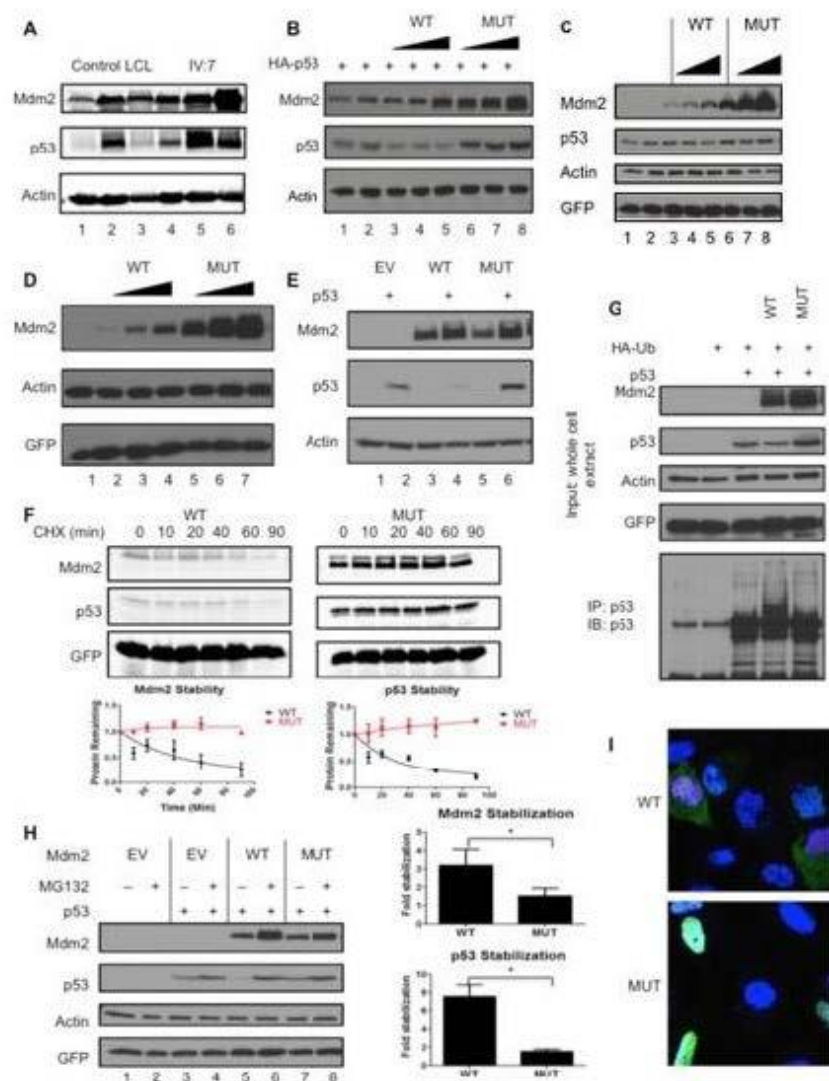
Supplemental Figure S2. Mutated Mdm2 is defective in its ability to regulate p53. (**A**) Levels of Mdm2, p53, and actin in LCLs of an unaffected individual (lanes 1-3: control LCL) and index patient (lanes 4-6: IV:7 LCL). Cell lines were treated with vehicle DMSO (-), Nutlin-3 (N, 10 μM), or daunorubicin (D, 0.1 mg/mL) for 24 hours before harvesting. Cell lysates were used for immunoblotting (IB) with the indicated antibodies (Mdm2: 2A9/3G5/4B11/5B10 mix, p53: MAbs 1801 and DO-1, anti-actin). (**B**) Degradation assay showing levels of ectopically expressed Mdm2 and p53 protein. U2OS cells were

transfected with increasing amounts of constructs expressing N-terminal FLAG-tagged wild-type (WT) and anti-termination mutant (MUT) Mdm2 as indicated (0.5-2 µg) and HA-tagged p53 (200 ng). Cells were harvested at 24 h. Cell lysates were used for immunoblotting (IB) with the indicated antibodies (Mdm2: FLAG; p53: HA, anti-actin). (**C**) Immunoblot showing levels of endogenously expressed p53 in presence of ectopically expressed WT or MUT Mdm2. U2OS cells were transfected with increasing amounts of N-terminal FLAG-tagged Mdm2 WT and MUT constructs as indicated (0.5-2 µg). Cells were harvested at 24h. A GFP construct (50ng) was included as a transfection and loading control. Cell lysates were used for immunoblotting (IB) with the indicated antibodies (Mdm2: FLAG, anti-actin, anti-GFP). (**D**) Levels of Mdm2 protein in a p53-null cell line. H1299 p53-null cells were transfected with increasing amounts of FLAG-tagged Mdm2 WT and MUT constructs as indicated (0.5-2 µg) and harvested at 24h. A GFP construct (50ng) was included as a transfection and loading control. Cell lysates were used for IB with the indicated antibodies (Mdm2: FLAG, anti-actin, anti-GFP). (**E**) Levels of ectopic p53 protein when WT and MUT Mdm2 proteins are expressed at similar levels. U2OS cells were transfected with N-terminal FLAG-tagged Mdm2 constructs calibrated to express equivalent levels of empty vector (EV, 2 µg), WT (2 µg) and MUT (0.4 µg) and HA-tagged p53 (200 ng) as indicated. Expression of GFP (50ng) was included as a transfection and loading control. (**F**) Protein degradation rate of co-expressed Mdm2 and p53 via cylcoheximide chase. U2OS cells were transfected with N-terminal FLAG-tagged Mdm2 WT and MUT constructs (2 µg) and HA-tagged p53 (200ng). 24 hours post-transfection, cells were treated with 100 µg/ml cycloheximide and harvested at the indicated time points. A GFP construct (50 ng) was included as a transfection and loading control. Cell lysates were used for immunoblotting with the indicated antibodies (Mdm2: FLAG, p53: HA, anti-GFP) and polypeptides were quantified using ImageJ software and normalized to GFP. Mdm2 and p53 half-lives were calculated through GraphPad Prism. (**G**) Shows relative ubiquitination of p53 by WT and MUT Mdm2 proteins. H1299 cells were transfected with constructs expressing N-terminal FLAG-tagged WT or MUT Mdm2 (2.6 µg), p53 (260ng), and HA-tagged ubiquitin (866 ng). After 24 h, cells were treated with MG132 (25 µM) for 4h before harvesting. Top panel: Aliquots of transfected cell lysates were subjected to immunoblotting with the indicated antibodies (Mdm2: FLAG, p53: FL-393, anti-GFP) to show input levels of the indicated proteins. Bottom panel: Extracts of cells were immunoprecipitated with anti-p53 antbodies (FL-393) and then probed with the anti-p53 polyclonal antibody (FL-393) to show higher molecular weight ubiquitinated p53 polypeptides. (**H**) Levels of ectopically-expressed Mdm2 and p53 after proteasome inhibition. U2OS cells were transfected with FLAG-tagged Mdm2 constructs calibrated to express equivalent levels of WT (2 µg) or MUT (0.4 µg) and HA-tagged p53 (200 ng). After 24 h, each set was either treated with MG132 (25 µM) for 4h or untreated with fresh media for 4h before harvesting. Left panel: Cell lysates were used for IB with the indicated antibodies. A GFP construct was included as a transfection and loading control. Right panel: Immunoblots were quantified using ImageJ software. Results shown are average of three experiments. Differences in fold of Mdm2 and p53 stabilization when WT or MUT Mdm2 was expressed has $p < 0.05$ significance. (**I**) shows the localization of ectopic p53 in cells expressing WT or MUT Mdm2. U2OS cells were transfected with N-terminal FLAG-tagged Mdm2 WT or MUT constructs (2 µg) and HA-tagged p53 (200 ng). Cells were fixed at 24 h and processed for immunofluorescence as described in Methods. The subcellular localization of p53 was determined using a mouse monoclonal antibody specific for the HA epitope.

5
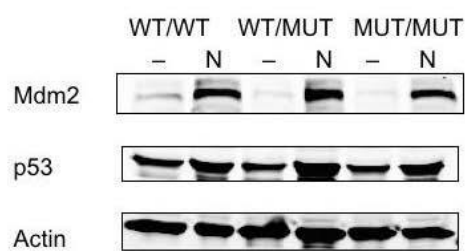
Supplemental Figure S3. **Mdm2 and p53 protein levels in U2OS genome-edited cells.** U2OS genome edited cells expressing WT/WT, WT/MUT, or MUT/MUT Mdm2 were treated with DMSO or Nutlin-3 for 24 hours before harvest and immunoblotting.

6
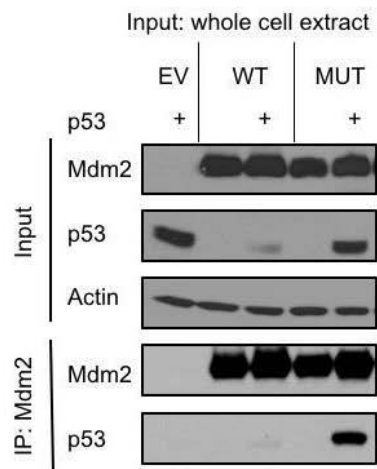
Supplemental Figure S4. Ectopically expressed mutant Mdm2 retains binding to p53. Shows that ectopic Mdm2 can bind to ectopic p53. U2OS cells were transfected with empty vector (EV, 2 μg) or N-terminal FLAG-tagged Mdm2 constructs calibrated to express equivalent levels of WT (2 μg) and MUT (0.35 μg) and harvested at 24 h. Left panel: Aliquots of transfected cell lysates were subjected to immunoblotting with the indicated antibodies (Mdm2: FLAG, p53: HA). Right panel: After co-immunoprecipitation with anti-FLAG antibody and subsequent IB, the proteins were detected using the same antibodies.
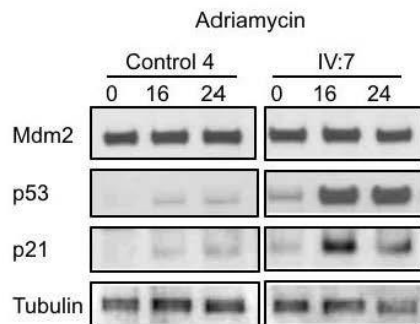
Supplemental Figure S5. Time course of Mdm2, p53 and p21 protein levels after treatment with Adriamycin. Shows protein levels of Mdm2, p53 and p21 of fibroblasts treated with adriamycin (3 µM). Control 88-1 (lanes 1-3) and IV:7 (lanes 4-6) fibroblasts were treated with adriamycin (3 µM) for 24 hours. Cells were harvested either right after treatment (lines 1 and 4), or were further cultured for 16 (lanes 2 and 5) or 24 hours (lanes 3 and 6) in adriamycin free medium. Cell lysates were used for immunoblotting (IB) with Mdm2 (N20), p53 (AF1355), p21 and γ-tubulin. Lanes were run on the same gel but were noncontiguous.

Clinical findings	Patient IV:7	Werner syndrome
Age at presentation	19	> 18
Bilateral cataracts	Absent	+*
Skin changes	+	+*
Pinched nasal bridge	+	+*
Short stature	+	+*
Prematurely gray/thinning hair	+	+*
Parental consanguinity	+	+*
Type 2 diabetes mellitus	-	+
Hypogonadism	+	+
Atherosclerosis	-	+
Neoplasms	-	+
High pitched voice	+	+
Renal failure	+	-

Supplemental Table 1. Clinical findings in the index patient presented here and in Werner syndrome. Skin changes include: scleroderma-like skin changes, tight, atrophic skin changes, hyperpigmentation, skin ulcers. * indicates a cardinal clinical feature for diagnosis of Werner syndrome.

9

Gene	Chr.	cDNA Change	Protein Change	dbSNP v138	ExAC Browser	Polyphen2
TRIM45	1	c.466C>T	His156Tyr	rs139632476	0/79/115732	benign
CD48	1	c.58T>C	Ser20Pro	rs375107070	0/5/121060	benign
MCM6	2	c.2428T>C	Tyr810His	rs55660827	0/26/121342	possibly damaging
PEX1	7	c.627G>A	Met209Ile	rs200752969	0/19/111150	benign
DGKA	12	c.512G>A	Gly171Asp	no	no	benign
TIMELESS	12	c.2578C>T	Arg860Cys	no	0/1/121406	probably damaging
MYO1A	12	c.1361A>G	Asp454Gly	rs201562120	0/6/117630	probably damaging
INHBC	12	c.361G>A	Asp121Asn	rs201463741	0/5/121140	benign
MDM2	**12**	**c.1492T>C**	**p.*498Qext5**	**no**	**no**	**-**
GDE1	16	c.242C>T	Thr81Met	no	0/1/107830	probably damaging
ARHGAP23	17	c.3047C>T	Thr1016Met	no	0/7/21948	possibly damaging
BRCA1	17	c.1648A>C	Asn550His	rs56012641	0/33/121032	probably damaging
BRCA1	17	c.1456T>C	Phe486Leu	rs55906931	0/36/121388	benign
BRCA1	17	c.536A>G	Tyr179Cys	rs56187033	0/33/121410	probably damaging
CACNA1G	17	c.6710C>A	Pro2237His	rs200141555	0/60/117720	benign

Supplemental Table 2. Homozygous variants with minor allele frequencies (MAF) < 0.01 within regions of homozygosity. All alterations were confirmed by Sanger sequencing.

10

Supplemental references:

1. Donaudy F, et al. Multiple mutations of MYO1A, a cochlear-expressed gene, in sensorineural hearing loss. *American journal of human genetics.* 2003;72(6):1571-7.
2. Eisenberger T, et al. Targeted and genomewide NGS data disqualify mutations in MYO1A, the "DFNA48 gene", as a cause of deafness. *Human mutation.* 2014;35(5):565-70.
3. Ishimi Y. A DNA helicase activity is associated with an MCM4, -6, and -7 protein complex. *The Journal of biological chemistry.* 1997;272(39):24508-13.
4. Urtishak KA, et al. Timeless Maintains Genomic Stability and Suppresses Sister Chromatid Exchange during Unperturbed DNA Replication. *The Journal of biological chemistry.* 2009;284(13):8777-85.
5. Miyoshi Y, et al. Acceleration of chromosomal instability by loss of BRCA1 expression and p53 abnormality in sporadic breast cancers. *Cancer letters.* 2000;159(2):211-6.
6. El-Harith el HA, et al. BRCA1 and BRCA2 mutations in breast cancer patients from Saudi Arabia. *Saudi medical journal.* 2002;23(6):700-4.
7. Simon GM, Cravatt BF. Characterization of mice lacking candidate N-acyl ethanolamine biosynthetic enzymes provides evidence for multiple pathways that contribute to endocannabinoid production in vivo. *Molecular bioSystems.* 2010;6(8):1411-8.

11

ORIGINAL INVESTIGATION

CrossMark

Analyses of *LMNA*-negative juvenile progeroid cases confirms biallelic *POLR3A* mutations in Wiedemann–Rautenstrauch-like syndrome and expands the phenotypic spectrum of *PYCR1* mutations

Davor Lessel[1] · Ayse Bilge Ozel[2] · Susan E. Campbell[3] · Abdelkrim Saadi[4] · Martin F. Arlt[2] ·
Keisha Melodi McSweeney[5] · Vasilica Plaiasu[6] · Katalin Szakszon[7] · Anna Szőllős[7] · Cristina Rusu[8] ·
Armando J. Rojas[9] · Jaime Lopez-Valdez[10] · Holger Thiele[11] · Peter Nürnberg[11,12,13] · Deborah A. Nickerson[14] ·
Michael J. Bamshad[14] · Jun Z. Li[2] · Christian Kubisch[1] · Thomas W. Glover[2] · Leslie B. Gordon[15,16]

Abstract

Juvenile segmental progeroid syndromes are rare, heterogeneous disorders characterized by signs of premature aging affecting more than one tissue or organ starting in childhood. Hutchinson–Gilford progeria syndrome (HGPS), caused by a recurrent de novo synonymous *LMNA* mutation resulting in aberrant splicing and generation of a mutant product called progerin, is a prototypical example of such disorders. Here, we performed a joint collaborative study using massively parallel sequencing and targeted Sanger sequencing, aimed at delineating the underlying genetic cause of 14 previously undiagnosed, clinically heterogeneous, non-*LMNA*-associated juvenile progeroid patients. The molecular diagnosis was achieved in 11 of 14 cases (~79%). Furthermore, we firmly establish biallelic mutations in *POLR3A* as the genetic cause of a recognizable, neonatal, Wiedemann–Rautenstrauch-like progeroid syndrome. Thus, we suggest that *POLR3A* mutations are causal for a portion of under-diagnosed early-onset segmental progeroid syndromes. We additionally expand the clinical spectrum associated with *PYCR1* mutations by showing that they can somewhat resemble HGPS in the first year of life. Moreover, our results lead to clinical reclassification in one single case. Our data emphasize the complex genetic and clinical heterogeneity underlying progeroid disorders.

Keywords Juvenile segmental progeroid syndrome · Hutchinson–Gilford progeria syndrome · Wiedemann–Rautenstrauch progeroid syndrome · *POLR3A* · *PYCR1*

Introduction

Segmental progeroid syndromes are defined as a heterogeneous group of rare monogenic disorders which prematurely mimic physiological aging by simultaneously affecting multiple organs and tissues (Martin 1978). The best known form with onset in early childhood is Hutchinson–Gilford progeria syndrome (HGPS). HGPS is caused by a recurrent de novo synonymous alteration c.1824C > T, p.Gly608Gly, in exon 11 of *LMNA* (De Sandre-Giovannoli et al. 2003; Eriksson et al. 2003). Around 10% of similarly affected individuals, referred to as atypical HGPS, bear de no*vo LMNA* mutations in the spliceosome recognition site of intron 11 (Gordon et al. 1993). These mutations result in increased usage of cryptic splice sites leading to an in-frame deletion of 150 nucleotides, and generation of a lamin A precursor lacking 50 amino acids at its C-terminus, termed prelamin A∆50

🖄 Springer

or "progerin" (Eriksson et al. 2003). In addition to HGPS, other mutations in *LMNA* have been identified in a number of cases affected by a variety of progeroid symptoms (Chen et al. 2003; Garg et al. 2009; Saha et al. 2010; Soria-Valles et al. 2016), including cases of late-onset segmental progeroid syndromes bearing heterozygous mutations at the junction of exon 11 and intron 11. Notably, these latter mutations also result in aberrant splicing and production of progerin, however to a lower extent than observed in HGPS (Hisama et al. 2011).

Mutations in several other genes have also been connected with early-onset segmental progeroid syndromes sharing overlapping phenotypic features with HGPS such as growth retardation, sparse scalp hair, mandibular underdevelopment, thin-appearing and transparent skin with prominent veins, and lipodystrophy. Examples include Cutis Laxa Type IIB with progeroid features caused by biallelic mutations in *PYCR1* (Reversade et al. 2009), Nestor–Guillermo progeria syndrome caused by biallelic mutations in *BANF1* (Puente et al. 2011), *ZMPSTE24*-related progeroid cases (Navarro et al. 2014), Berardinelli–Seip congenital lipodystrophy (Van Maldergem 1993), mandibular hypoplasia, deafness, progeroid features, and lipodystrophy syndrome (Lessel et al. 2015; Nicolas et al. 2016; Weedon et al. 2013), marfanoid–progeroid–lipodystrophy syndrome caused by *de novo* mutations in *FBN1* (Graul-Neumann et al. 2010; Passarge et al. 2016) as well as single cases bearing likely causative mutations in *CAV1* (Schrauwen et al. 2015) and *POLR3A* (Jay et al. 2016).

Here, we describe results from systematic genetic analysis, including massively parallel sequencing and targeted Sanger sequencing, of 14 children referred either to The Progeria Research Foundation (PRF) or to the Institute of Human Genetics at the University Medical Center Hamburg-Eppendorf, with clinical diagnosis of an early-onset segmental progeroid syndrome in whom direct sequencing of *LMNA* and *ZMPSTE24* gave normal results.

Materials and methods

Human subjects

We investigated 14 individuals who had been referred either to The Progeria Research Foundation (PRF, http://www.progeriaresearch.org) or to the Institute of Human Genetics at the University Medical Center Hamburg-Eppendorf, with clinical diagnosis of a HGPS-like segmental progeroid syndrome, and in whom *LMNA* and *ZMPSTE24* mutations were first excluded. All biological samples and images were obtained following written informed consent from affected individuals or their legal representatives. Lymphoblastoid cell lines (LCLs) of individual 4 and her parents

were generated by standard procedures after an informed consent. The study has ongoing approval from the Hasbro Children's Hospital and the University Medical Center Hamburg-Eppendorf Institutional Review Boards. The study was performed in accordance with the Declaration of Helsinki protocols.

Genetic analyses

DNA samples from whole blood were isolated by standard procedures. For candidate gene analysis, namely *LMNA, ZMPSTE24, PYCR1 and POLR3A*, we performed direct Sanger sequencing. Trio-whole exome sequencing experiments with DNA samples of both healthy parents and the index patients were performed in three different centers with slightly different procedures that have essentially been previously described. In more detail, in families 1–5 exome sequencing targeting ~44 Mb of the genome of proband DNAs was performed on exons captured by Roche Nimblegen SeqCap EZ Human Exome Library v2.0 and sequenced using the Illumina HiSeq2500/4000 in the University of Michigan Sequencing Core. Individual DNAs were each run on a single lane using 100-bp paired-end sequencing. The average coverage ranged from 158× to 276×. Exome sequencing of parental DNA samples was performed at the University of Washington Center for Mammalian Genomics on exons captured by Roche Nimblegen SeqCap EZ Human Exome Library v2.0 and sequenced using the Illumina HiSeq2500/4000 as previously described (Chong et al. 2015). The average coverage ranged from 46× to 57×. In families 6–10, exome sequencing was performed at the Cologne Center for Genomics on two lanes of an Illumina GAIIx Sequencer using a single-read 150-bp protocol after enrichment of exonic and splice-site sequences with the Agilent SureSelect Human All Exon 50 Mb kit as previously described (Lessel et al. 2017). In families 11–14, only direct sequencing of candidate genes, i.e. *PYCR1* or *POLR3A*, was performed.

Bioinformatic analysis

Variant annotation and bioinformatic filtering was performed using three independent in-house annotation pipelines.

For families 1–5, the exome sequencing data were included in a 734-exome joint call in GATK. After removing variants of low quality [GATK's VQSR, Genotype Quality (GQ) < 20, Read Depth (RD) < 10], we annotated the remaining on-target variants by ANNOVAR. Further filtering was applied to keep (1) the splicing-altering sites, frameshift, nonsense and missense mutations predicted as damaging by Polyphen2 and SIFT, (2) those that are not common (MAF < 1%) in the European subset ($n = 514$) of the 1000 Genomes Project or in the Exome Sequencing

Project ($n = 4,300$), and (3) not present in more than 5% of the in-house controls ($N > 500$). These variants were analyzed with a recessive model and a de novo model, with the top candidate genes further filtered to remove those with previous associations with human diseases and/or without OMIM annotations.

For families 6–10, in-house-developed scripts were applied to detect protein changes, affected splice sites and overlaps to known variations, with filtering against dbSNP build 138, the 1000 Genomes Project data build November 2014, ExAC Browser (status from August 2018) and the in-house database of exome variants (with data from > 200 exomes of individuals affected by different disorders). The criteria for a variation to be taken into account were: >6 reads, Phred scaled quality score > 15, population allele frequency < 1%, < 10 times seen in our in-house database and > 15% of the reads supporting the allele.

Candidate variants were validated by Sanger sequencing. For families 11–14, candidate genes, *PYCR1* or *POLR3A*, were analyzed by Sanger sequencing. All primer pairs are available upon request.

RT-PCR analysis

Total RNA was extracted from LCLs of individual 4 and her parents using a Qiagen RNeasy Mini Kit. First-strand cDNA synthesis was carried out using the High-Capacity cDNA Reverse Transcription Kit (ThermoFisher Scientific), primed with an oligo in exon 31 of POLR3A (5′-TGTGAGCTGCAC CCTATCAG-3′) following the manufacturer's protocol. The POLR3A cDNA was PCR amplified using primers in POLR3A exons 25 (5′-GATCATCAACGCTTCCAAGG-3′) and 27 (5′-CCTTGGGGAGATCCTCTTTC-3′). Resulting products were electrophoresed, revealing bands of two sizes (287 bp, 380 bp), which were gel extracted, and subjected to Sanger sequencing. The larger band (380 bp) corresponded to the wild-type POLR3A sequence from exons 25 to 27, including exon 26. The smaller band (287 bp), found only in the proband and the father, corresponded to POLR3A mRNA lacking exon 26.

Results

Case reports

Individual 1

This male proband is the first child of healthy unrelated parents. He has three unaffected siblings. He was born after an uneventful pregnancy at 40 weeks of gestation. His birth weight was 1930 g (− 3.84 SD) with length of 40.5 cm (− 5.22 SD). This boy showed wrist contractures, kyphosis and poor feeding since birth, three natal teeth, and a generalized lipodystrophy. He further had thin-appearing and translucent skin with prominent veins, triangular face with midface retraction, frontal bossing, deep set and closely spaced eyes, low set ears and mandibular underdevelopment. However, he did not have sparse scalp hair (Fig. 1a; Table 1). Milestones of motor development and language development were unremarkable. Kyphosis improved by the age of 4 years. At clinical evaluation at the age 10 years, a small jaw and low set ears were observed. He had a weight of 25.4 kg (− 1.84 SD) and height of 128.3 cm (− 1.98 SD), still having severe feeding difficulties. His hair was sparse and thin. He had only five teeth. Further, he had global lipodystrophy, prominent veins and a nasal high-pitched voice.

Individual 2

This male proband is the only child of healthy unrelated parents. Pregnancy was complicated by oligohydramnios and frank breech position leading to birth by cesarean section at 32 weeks of gestation with APGAR scores of 7 at 1 min and 9 at 5 min. His birth weight was 935 g (− 2.38 SD), length 36.5 cm (− 2.16 SD), and a borderline occipitofrontal head circumference (OFC) of 26 cm (− 2.32 SD). A patent foramen ovale and large patent ductus arteriosis were observed after birth. In addition, due to pulmonary hypoplasia he received endotracheal intubation and ventilator support during the first few weeks of life. At the clinical evaluation at the age of 1 year and 5 months, he had a triangular face, sparse scalp hair, thin-appearing and translucent skin with prominent veins, frontal bossing, deep set eyes, somewhat low set ears and a mandibular underdevelopment. Moreover, he had bilateral corneal opacities, strabismus and nystagmus, global lipodystrophy, joint hypermobility, and had developed an inguinal hernia (Fig. 2a; Table 2). All milestones of motor development were delayed: rolling over at 12 months, sitting at 24 months, and walking at 3 years. Language development was significantly delayed as he spoke his first words at the age of 4 years. Clinical evaluation at the age of 3 years revealed the following facial dysmorphisms: frontal bossing, dolichocephaly, prominent occiput, mandibular prognathism (anterior open bite and mandibular overjet), mildly low set ears with right avulsion of pinna, short philtrum and deep set eyes. He had brittle teeth, requiring multiple dental restorations at age 4 years, and some secondary teeth were absent. He developed seizures at the age of 3 years (petit mal and grand mal). A brain MRI, performed at the age of 5 years, revealed mild enlargement of occipital horns with thinning of periventricular white matter. At the age of 6 years, an intracerebral abscess of the frontal lobe was observed. In addition, this boy had thin-appearing, transparent and wrinkled skin with easily visible vasculature. Several eye anomalies including mild optic nerve hypoplasia, small

Fig. 1 Clinical characteristics of *POLR3A*-mutated individuals. Facial images of individual 1 at age 4 months, 1.5 years and 2 years and 10 months (**a**), individual 4 at the age of 1 year and 7 months, and 3 years (**b**), and individual 11 from the birth till 11 months (**c**)

optic nerves, optic atrophy, nystagmus, strabismus, myopia, and dissociated vertical deviation (DVD) were present. He had muscular hypotonia with decreased muscle mass for age, and frequent myalgias. Further, severe pectus excavatum, osteoporosis, arthritis of the left leg, scoliosis, pes planus, advanced bone age, hyperflexibility in limbs and especially small joints (fingers), prominent interphalangeal (IP) joints in the hands, and hallux valgus deformity were documented.

At the age of 8 years, a mildly prolapsed mitral valve was observed. In addition, he had conductive hearing loss and eustachian tube dysfunction (ETD), for which he received pressure equalization (PE) tubes. Moreover, he displayed global lipodystrophy, mild excessive posterior nuchal skin, widely spaced and underdeveloped nipples, and hypoplastic nails.

71

Table 1 Comparison of clinical characteristics of Wiedemann–Rautenstrauch-like, *POLR3A*-mutated patients presented here, the *POLR3A*-patient from the previous study (Jay et al. 2016), and patients from the literature with suggestive diagnosis of Wiedemann–Rautenstrauch syndrome (Paolacci et al.)

	Individual 1	Individual 4	Individual 11	Previous study, Jay et al.	WRS, Paolacci et al.
Sex	Male	Female	Female	Female	11 female 7 male
Age	10 years	12 years 9 months	11 months	Deceased at 7 months of age	n.d
Ethnicity	European	European	Latino	European	Various
Intrauterine growth retardation	+	+	+	+	9/16
Triangular face	+	+	+	+	18/18
Sparse scalp hair	−	+	+	+	17/18
Thin/translucent skin	+	+	+	+	15/15
Prominent scalp veins	+	+	+	+	17/18
Frontal bossing	+	+	+	+	n.d
Closely spaced eyes	+	+	+	+	n.d
Midface retraction	+	+	+	+	n.d
Low set ears	+	+	+	+	n.d
Natal teeth	+	−	−	+	17/18
Mandibular underdevelopment	+	+	+	+	n.d
Joint contractures	+	+	−	+	n.d
Motor development delay	−	+	?	?	n.d
Impaired speech development	−	+	?	?	n.d
Delayed dentition/oligodontia	+	+	?	?	8/16
Lipodystrophy	+	+	+	+	18/18
Cardiac anomalies	−	+	+	-	n.d
Short stature	+	+	?	?	6/7
Kyphosis	+	−	−	−	n.d
Congenital respiratory complications	−	+	+	+	n.d
Brain anomalies US/MRI	n.d	n.d	Agenesis of corpus callosum	−	2/7
POLR3A mutation					
Paternal	c.3337-5T>A	c.3337-5T>A	p.M1I	c.1909+18G>A	n.d
Maternal	c.3337-1G>A	p.R254*	Not identified	p.R873*	n.d

+ present, − absent, ? due to young age not applicable, *n.d.* not done, *WRS* Wiedemann–Rautenstrauch syndrome

Individual 3

This male proband is the first child of healthy unrelated parents. He has a younger unaffected sibling. He was born at 38 weeks of gestation by caesarean section due to in utero cracked ribs, broken femur and wide fontanelles. His birth weight was 2275 g (− 2.37 SD), length was 48 cm (− 1.35 SD) and OFC was 33.7 cm (− 0.86 SD). At birth, he displayed wrist and ankle contractures (bilateral talipes equinovarus/club feet) that were surgically corrected soon after birth resulting in continued normal range of movement. In addition, the boy had no scalp hair, frontal bossing, prominent veins, poor ossification of the calvarium with open fontanelles and wide sutures. Further, he had a blepharophimosis-type appearance with telecanthus and epicanthus inversus with epiblepharon, unusual supraorbital rims that appeared hypoplastic and sloping (Fig. 3a). Muscular hypotonia characterized the postnatal period. X-ray at 4 months revealed poor ossification of the calvarium with widened sutures and fontanelles. Evidence of an old healed fracture at the junction of the proximal/mid left femoral diaphysis was seen. He underwent surgery for undescended testes at age 12 months. Milestones of motor development were delayed: he sat unaided at 12 months, exhibited bottom shuffling but no crawling at 18 months, and walked at around 2.5 years. Language development was significantly delayed; however, the speech dramatically improved after insertion of ventilation tubes at the age of 3 years. He had a high-pitched voice. First teeth erupted at the age of 18 months. He suffered from osteopenia and recurrent fractures: small fractures in
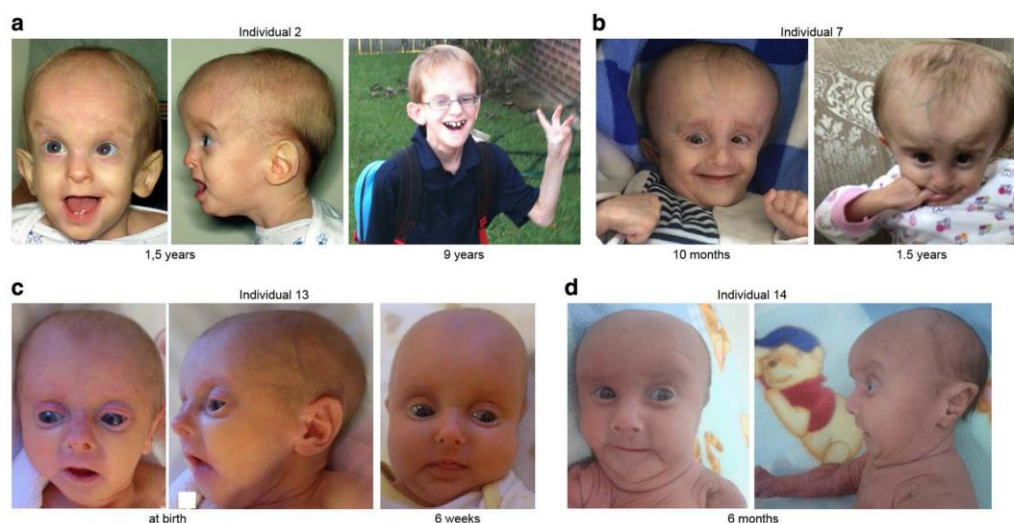
Fig. 2 Clinical characteristics of *PYCR1*-mutated individuals. Facial images of individual 2 at 1.5 years and 9 years (**a**), individual 7 at the age of 10 months and 1.5 years (**b**), individual 13 at birth and 6 weeks (**c**), and individual 14 at 6 months (**d**)

right elbow at age 6 years and C2 vertebrae at age 8 years. At clinical evaluation at the age of 9 years, epiblepharon, astigmatism, light sensitivity, blue sclerae, and mandibular underdevelopment with dental crowding were observed. He had a weight of 13.7 kg (− 7.60 SD), a height of 104 cm (− 5.25 SD) and an OFC of 51 cm (− 1.68 SD). He had thin hair, global lipodystrophy, and muscular hypotonia.

Individual 4

This female proband is the second child of healthy unrelated parents. She was born at 34 weeks of gestation by cesarean section for intrauterine growth retardation and non-reassuring fetal heart tracing. Her birth weight was 1160 g (− 2.58 SD), length was 41.5 cm (− 1.41 SD) and OFC was 27.5 cm (− 2.47 SD). Apgars were 7 at 1 min and 8 at 5 min. At delivery, she presented with poor respiratory effort initially that improved after continuous positive airway pressure (CPAP) therapy. In addition, a large patent ductus arteriosus (PDA), mild aortic insufficiency and mild tricuspid valve incompetency were observed. She had a feeding tube placed during the first year of life. At the age of 1 year and 7 months, she had a triangular face, sparse and thin hair, prominent scalp veins, frontal bossing, closely spaced eyes, midface retraction, malformed and low set ears, and mandibular underdevelopment, somewhat mimicking Wiedemann–Rautenstrauch syndrome (Fig. 1b; Table 1). She had severe knee flexion

contracture and less severe bilateral hip flexion contractures that impeded her walking independently in the earlier years. She was walking independently at the age of 5 years wearing a left knee brace. She had speech therapy in pre-school. Cardiac evaluation revealed a mildly eccentric aortic valve and mild left ventricular hypertrophy. She had a Chiari malformation, and received a ventriculoperitoneal shunt for intracranial hypertension. At the age of 5 years she had a weight of 8.3 kg (− 8.32 SD), a height of 87.6 cm (− 5.03 SD) and an OFC of 50.3 cm (− 1.06 SD). At the age of 12 years and 9 months, she exhibited a prematurely aged facial appearance. She still had partial alopecia, severe frontal bossing, a triangular face, small and deep set eyes, an entropion, a beaked nose, dental dysplasia with missing teeth, and mandibular underdevelopment. She had global lipodystrophy, thin arms and legs, and contractures of elbows and knees.

Individual 5

This female proband was referred at the age of 10 months due to a triangular face, sparse scalp hair, thin-appearing and translucent skin with prominent veins, frontal bossing, deep set eyes, somewhat low set ears and mandibular underdevelopment. In addition, she had a generalized lipodystrophy and joint hand contractures (Table 2). Unfortunately, the contact with the family and the referring physician was later lost.

Table 2 Clinical characteristics of *PYCR1*-mutated patients presented here

Individual	2	5	6	7	10	12	13	14
Sex	Male	Female	Male	Male	Male	Male	Female	male
Age	9 years	10 months	4 years	3.5 years	2 years 9 months	2 years 2 months	13 months	9 months
Ethnicity	European	European	African	Arabian	European	European	European	Latino
Intrauterine growth retardation	+	d.u	+	+	+	+	+	+
Postnatal growth retardation	+	d.u	+	+	−	−	?	?
Triangular face	+	+	+	+	+	+	+	+
Sparse scalp hair	+	+	+	+	+	+	+	+
Thin/translucent skin	+	+	+	+	+	+	+	+
Prominent scalp veins	+	+	+	+	+	+	+	+
Frontal bossing	+	+	−	+	+	+	−	−
Deep set eyes	−	+	+	+	−	−	+	+
Low set ears	+	+	−		−	−	−	−
Mandibular underdevelopment	+	+	+	+	+	+	+	+
Joint hypermobility	+	d.u	−	−	+	+	+	+
Joint contractures	−	+	−	−	−	−	+	−
Motor development delay	+	d.u	+	+	+	+	+	?
Muscular hypotonia	+	d.u	+	+	+	+	+	+
Impaired speech development	+	d.u	+	+	+	+	?	?
Dental anomalies	+	d.u	−	−	−	−	−	−
Cataract/corneal opacities	+	d.u	−	−	−	−	−	−
Strabismus	+	d.u	−	−	−	−	−	−
Myopia	+	d.u			+			+
Osteopenia/osteoporosis	+	d.u	−	−	−	−	−	−
Lipodystrophy	+	+	+	+	+	+	+	+
Cardiac anomalies	+	d.u	−	−	−	−	−	+
Wrinkled skin	> 6 years	d.u	> 2.5 years	−	> 2.5 years	> 2 years	> 1 years	since birth
Microcephaly	+	d.u	+	+	+	+	+	+
Congenital respiratory problems	+	d.u	−	+	−	−	−	+
Hernias	+	d.u	−	−	−	+	−	+
Hearing loss	+	d.u	−	−	−	−	−	−

74

Table 2 (continued)

Individual	2	5	6	7	10	12	13	14
Brain anomalies US/MRI	White matter abnormalities	d.u	Agenesis of corpus callosum	Agenesis of corpus callosum	Cysts and micro-calcifications	n.d	Agenesis of corpus callosum	Agenesis of corpus callosum
PYCR1 mutation								
Paternal	c.633 + 1G > C	p.K71N*fs**10	p.R119C	p.I74T*fs** 10	p.I74T*fs** 10	p.I74T*fs** 10	c.797 + 2_5 delTGGG	p.A257T
Maternal	p.A179T	p.R119H	p.R119C	p.I74T*fs** 10	p.R313L	p.V258L	c.540 + 1G > A	p.A257T

+ present, − absent, d.u. data unavailable, ? due to young age not yet applicable, *n.d.* not done

Fig. 3 Clinical characteristics of *COL1A1*-mutated individual and the two unclassified juvenile progeroid individuals. Facial images of individual 3 bearing the de novo *COL1A1* mutation at age 8 months and 1 year (**a**), individual 8 at the age of 1 year and 3 years (**b**), and individual 9 at 13.5 years (**c**)

Individual 6

This male proband is the second child of healthy consanguineous parents who are first cousins. His older brother is unaffected. He was born after an uneventful pregnancy at 40 weeks of gestation. Birth weight was 2550 g (− 2.44 SD), head circumference was 33 cm (− 2.00 SD), and length was not available. The neonatal period was notable for muscular hypotonia, hip dislocation, gastrointestinal reflux and mild jaundice. He had a triangular face, sparse scalp hair, thin-appearing and translucent skin with prominent veins and mandibular underdevelopment. All milestones of motor

75

development were delayed: he sat unaided at 10 months, walked by age 1.5 years, verbal expression was restricted to a few words, and he understood only basic verbal commands. At the clinical evaluation at the age of 2 years and 7 months, he had microcephaly (OFC was 46.5 cm; − 2.50 SD), height of 90 cm (0.54 SD) and weight of 10 kg (− 1.73 SD). He had a triangular face with a progeroid appearance, sparse hair, prognathism, open mouth appearance and large ears. His skin was wrinkled on the dorsum of his hands and feet with visible subcutaneous veins. He had long fingers and flat feet. X-rays revealed atrophy of left femoral head. Osteopenia was not detected. Routine laboratory findings including lactates, creatine kinases (CK), and thyroid hormone were all within the normal range. ECG, echo Doppler cardiography, and abdominal ultrasound were normal. At the clinical visit at the age of 4 years, his growth parameters improved: OFC was 48.5 cm (− 2.12 SD), height was 103 cm (− 0.26 SD), and weight was 15 kg (− 0.89). He had developed agitation, impaired concentration and gestural stereotypies. MRI of the brain demonstrated agenesis of the corpus callosum (Table 2).

Individual 7

This male proband is the second child of healthy consanguineous parents who are first cousins. His older sibling was unaffected. He was born at 34 weeks of gestation with a birth weight of 900 g (− 3.39 SD), length of 37 cm (− 3.17 SD) and OFC of 26 cm (− 3.65 SD). He had respiratory problems in the first weeks of life and suffered from poor feeding since birth. Brain MRI, performed at the age of 8 months, revealed a prominent supratentorial ventricular system and agenesis of the corpus callosum. At the age of 1 year, he had a triangular face with a broad appearing cranium, midface retraction and relatively small facial bones, sparse scalp hair, thin-appearing and translucent skin with prominent veins, frontal bossing, deep set eyes, low set ears, a small mandible and lipoatrophy (Fig. 2b; Table 2). He started walking independently at age 3 years and spoke his first words by age 3.5 years. At 3.5 years of age he still suffered from a poor growth with a weight of 11 kg (− 2.52 SD) and height of 90 cm (− 2.49 SD), despite nutritional supplements (PediaSure®).

Individual 8

This male proband is the second child of healthy unrelated parents. His younger sibling is unaffected. He was born after an uneventful pregnancy at 40 weeks of gestation. His birth weight was 2800 g (− 1.87 SD) and length was 50 cm (− 1.09 SD). At birth, he presented with prominent scalp veins, prominent ears, small facial bones, generalized skin mottling and lipodystrophy. In addition, he had two ulcers

on the scalp at birth. At the age of 9 months X-ray showed advanced bone age of 1.8 years. Chest ultrasound showed a patent foramen ovale. His psychomotor development was normal. By the age of 2 years he developed bilateral cataracts. At the age of 3 years, he had a triangular face with sparse scalp hair and prominent scalp veins, and mandibular underdevelopment. He still had generalized skin mottling, lipodystrophy, and poor weight gain (Fig. 3b). His weight was 10 kg (− 2.98 SD) and height was 87 cm (− 2.45 SD).

Individual 9

This proband is the first child of healthy unrelated parents. He was born after an uneventful pregnancy at 39 weeks of gestation. His birth weight was 3000 g (− 1.17 SD) and length was 48 cm (− 1.7 SD). His early development was unremarkable. He developed scleroderma-like skin changes by the age of 1 year. At the examination at 13 years and 7 months he had a height of 161 cm (+ 0.51 SD), weight of 38 kg (− 1.4 SD) and OFC of 54.3 cm (− 0.46 SD). He had hypertelorism, delimited nose wings, mandibular underdevelopment, scoliosis, delayed bone age, multiple muscle contractures (elbow, hands and feet), and generalized progressive muscular atrophy (Fig. 3c). CK was normal. X-ray of his calf revealed diminished muscles with multiple calcifications. Muscle biopsy showed phagocytosis with inflammation of some muscle fibers, unequal muscle fibers, and blood vessels with slightly thick walls, likely due to fibrosis in the perimysium. His skin was tight and he still had scleroderma-like skin changes. In addition, he had generalized lipodystrophy. Total blood cholesterol was 150 mg/dL, while he had low HDL of 24 mg/dL and high triglycerides of 370 mg/dL. Glucidic metabolism and glycated hemoglobin were normal. Moreover, acanthosis nigricans in the axillar and inguinal area, as well as on the flexion surface of the elbow and knee was observed. In addition, the skin was very thick in the axillar and inguinal area.

Individual 10

This male proband is the first child of healthy unrelated parents. Pregnancy was complicated by oligohydramnios and intrauterine growth retardation starting at 30 weeks of gestation. He was born after 38 weeks of gestation. His birth weight was 2300 g (− 2.32 SD), length was 43 cm (− 3.52 SD) and OFC was 32 cm (− 2.07 SD). At birth, he presented with plagiocephaly, frontal bossing, a sharp nasal tip, anteverted nostrils, micrognathia, generalized lipoatrophy, and transparent skin with prominent veins. At the clinical evaluation at 9 months of age, his weight was 7 kg (− 1.89 SD), height was 70 cm (− 0.95 SD) and OFC was 42 cm (− 3.14 SD). He still had craniofacial abnormalities, generalized lipoatrophy, with tight and transparent skin

76

and prominent veins. Cranial ultrasound revealed a choroid plexus cyst, a subependymal cyst and microcalcifications in the thalamo-caudate region. Extensive metabolic analyses gave normal results, apart from low HDL (32 mg/dL) and high total triglycerides (162.6 mg/dL). Several milestones were normal: he sat at age of 6 months, crawled at 9 months, and walked independently at age 1 year 3 months. However, at the clinical examination at 2 years, he had an intellectual disability with no speech, and a hyperkinetic movement disorder. His weight was 11 kg (− 0.69 SD), height was 86 cm (0.08 SD) and OFC was 47 cm (− 1.72 SD). He had a triangular facial gestalt, tight skin, sparse scalp hair, generalized lipoatrophy, muscular atrophy and joint hypermobility. At the last available clinical evaluation at 2 years and 9 months of age, his weight was 11.7 kg (− 1.39 SD) and OFC was 48.5 cm (− 1.61 SD). He had transparent, lax and thin-appearing skin, with visible veins especially on his head and extremities. In addition, he had wrinkled skin on his hands. Moreover, he had joint hypermobility which affected his movements, and generalized lipodystrophy (Table 2). His gait was unsteady, with external rotated legs for better stability, and with flat feet. He had myopia. He spoke only single short syllables. Movements were hyperkinetic, and he displayed hand automatisms, taking objects to his mouth and touching them with his tongue.

Individual 11

This female proband is the only child of healthy unrelated parents. Prenatal ultrasound gave normal results in the first and second trimesters. However, ultrasound in the last trimester revealed a Dandy–Walker malformation, brachycephaly, a nasal bridge hypoplasia, and severe intrauterine growth retardation. Prenatal karyotype after amniocentesis at 28 weeks gave normal results, 46, XX. She was born at 37 weeks of gestation. Her weight was 1460 g (− 3.48 SD) and length was 43 cm (− 2.71). At birth, she had a triangular face, sparse scalp hair, frontal bossing, thin-appearing skin with prominent scalp veins, closely spaced eyes, midface retraction, low set ears, mandibular underdevelopment and generalized lipoatrophy (Fig. 1c; Table 1). In addition, she had a patent ductus arteriosus and mild renal pelvic ectasia. Due to low birth weight and severe tachypnea, she remained hospitalized for 6 weeks. She had a slow weight gain despite hyper-caloric nutritional supplements. All early milestones of motor development were unremarkable: rolling over at 6 months, sitting at 8 months, crawling at 9 months. She started babbling at 11 months. Brain MRI revealed agenesis of corpus callosum. At the clinical examination at 11 months of age, her weight was 3.6 kg (− 6.22 SD), height was 57 cm (− 5.99 SD) and OFC was 40 cm (− 5.11). She had trigonocephaly and brachycephaly, sparse scalp hair, low set ears with dysplastic auricular pavilions with bilateral grade

1 microtia, hypertelorism, marked enophthalmos, lagophthalmos and bilateral ectropion with blepharospasm resulting in incomplete closure of the eyes, midface retraction, a depressed and wide nasal bridge, hypoplastic nasal wings, mandibular underdevelopment, and a short neck. In addition, she had hypoplastic nipples, a small umbilical hernia, and generalized muscular atrophy.

Individual 12

This male proband is the only child of healthy unrelated parents. He was born at 38 weeks of gestation. His birth weight was 2300 g (− 2.32 SD) and length was 47 cm (− 1.78 SD). At birth, he presented with an inguinal hernia that was remedied by surgery. In addition, he presented with frontal bossing, a sharp nasal tip, anteverted nostrils, micrognathia, generalized lipodystrophy, and transparent skin with prominent veins. He sat independently at age 6 months, crawled at age 7 months, walked independently at age 1 year 9 months. At the clinical evaluation at 1 year and 8 months of age, his weight was 9.1 kg (− 2.04 SD), height was 79 cm (− 1.76 SD) and OFC was 46.5 cm (− 1.99 SD). He had a triangular facial gestalt, tight skin, sparse scalp hair, generalized lipodystrophy, muscular atrophy and joint hypermobility. At the last available clinical evaluation at 2 years and 2 months of age, his weight was 12 kg (− 0.52 SD), height 85 cm (− 1.35 SD) and OFC of 48.5 cm (− 1.12 SD). He still had thin-appearing and transparent skin, especially on the extremities, and developed wrinkled skin on his abdomen and hands (Table 2). He displayed a retraction of the sternum due to thoracic laxity that was accentuated by respiratory movements. He spoke only a few words but understood orders well. In addition, he is a hyperkinetic child.

Individual 13

This female proband is the only child of unrelated parents. Pregnancy was complicated by oligohydramnios and intra-uterine growth retardation. She was born at 32 weeks of gestation. Her weight was 1400 g (− 0.98 SD), length was 42 cm (− 0.18 SD) and OFC was 28 cm (− 0.95 SD). She remained hospitalized until she reached 2000 g. She had an aged appearance with a triangular facial gestalt, sparse hair, pinched nose, hypoplastic alae nasi, sunken in eyes with lack of periorbital fat tissue, mandibular underdevelopment, thin-appearing and transparent skin with prominent veins, thin limbs distally, and the fat pads on her gluteal region and thighs were spared but saggy. Fingers exhibited mild contracture, with the thumbs overlapping the palms, and the 2nd and 5th digits overlapping the 3rd. Brain MRI revealed agenesis of the corpus callosum. Upon last available clinical evaluation at 13 months of age, her weight was 6 kg (− 3.79 SD), height was 75 cm (− 0.95 SD) and OFC was 42 cm

(− 4.50 SD). She had a triangular face with broad forehead, protruding ears, and hypotelorism. Her skin was thin-appearing, atrophic, transparent, and wrinkled on distal extremities with sparse, thin scalp hair (Fig. 2c; Table 2). The muscles were atrophic and the joint hypermobile. Extensive metabolic analyses gave normal results. Her mother died following breast cancer, thus a maternal DNA sample was unavailable for genetic testing.

Individual 14

This male proband is the fourth child of healthy consanguineous parents who are second cousins. Pregnancy was complicated by breech presentation and premature rupture of membranes. He was born at 34 weeks of gestation. His weight was 1700 g (− 1.51 SD), length was 36.5 cm (− 3.34 SD) and OFC was 30 cm (− 1.29 SD). He remained hospitalized for 8 days due low birth weight, hyperbilirubinemia, mild renal pyelectasis, umbilical hernia and an inguinoscrotal hernia. At last available clinical evaluation at 9 months of age, his weight was 4.3 kg (− 5.04 SD), height was 56 cm (− 6.03 SD) and OFC was 38 cm (− 6.94 SD). He had muscular hypotonia and an overall aged appearance with triangular face, sparse and fine hair, sunken in eyes, posteriorly rotated and low ears, thin lips, micrognathia, joint hypermobility and generalized lipodystrophy. His skin was thin appearing and transparent with prominent veins, wrinkled on the neck, trunk and especially pronounced on extremities (Fig. 2d; Table 2). Moreover, he had a linear sclerodermatous plaque skin over the proximal right thigh. His thumbs overlapped his palms, and his 3rd and 5th digits overlapped his 4th digit. His scrotum was hypoplasic. Moreover, brain MRI revealed agenesis of corpus callosum. Ultrasound further revealed mild aortic and pulmonary artery dilatation, and bilateral dysplasia of the hip. He suffered from poor feeding, and had moderate myopia (− 5.5 D).

Genetic analyses

Identification of biallelic *PYCR1* mutations

Trio-whole exome sequencing (trio-WES), followed by bioinformatic filtering for biallelic variants in genes previously connected to well-established progeroid syndromes, identified in more than one individual, revealed likely pathogenic biallelic mutations in *PYCR1* in five individuals. In individual 2, we identified compound heterozygosity for a paternally inherited splice donor alteration c.633 + 1G > C, and maternally inherited c.535G > A, p.(Ala179Thr). Individual 5 bears a paternally inherited c.213_214delGC, leading to a frameshift mutation p.(Lys71Asn*fs**10), and maternally inherited c.356G > A, resulting in a missense alteration p.(Arg119His). Individual

6 bears homozygosity for c.355C > T, resulting in a missense alteration affecting the identical amino acid as in individual 5, p.(Arg119Cys). Individual 7 bears a homozygous 2-bp insertion c.219_220insAC, resulting in a frameshift mutation p.(Ile74Thr*fs**10). Finally, individual 10 bears compound heterozygosity for the paternally inherited 2-bp insertion c.219_220insAC, resulting in a frameshift mutation p.(Ile74Thr*fs**10), identical to the insertion identified in individual 7, and a maternally inherited c.938G > T, resulting in a missense alteration p.(Arg313Leu). Notably, the majority of these mutations have already been described in *PYCR1*-associated pathologies (p.(Arg119His), p.(Arg119Cys), c.633 + 1G > C and p.(Ala179Thr)) (Dimopoulou et al. 2013; Reversade et al. 2009), or result in a recurrent frameshift mutation (c.219_220insAC, p.(Ile74Thr*fs**10)). Thus, there is a strong evidence for the pathogenicity of these mutations. The pathogenicity is not that clear for the missense alteration (p.(Arg313Leu)) that has not been found in dbSNP, 1000 Genomes, the ExAC or the gnomAD browser, is predicted to result in decreased PYCR1 stability (Table 4) and affects only a single *PYCR1* isoform (ENST00000337943.9). We have, therefore, further evaluated all rare variants identified in individual 10 by trio-WES that was performed with sufficient coverage. Approximately, 94% of target sequences were covered at least 20-fold with a mean coverage of about 100×. Bioinformatic filtering for a rare candidate variant (minor allele frequency MAF < 0.02) did not identify any de novo variants nor variants following the X-linked recessive mode of inheritance, but only compound heterozygosity for two variants in *DNER*, a gene so far not connected to a human disease; namely a paternally inherited c.762T > A, resulting in missense alteration p.Asp254Glu, and a maternally inherited c.121C > T, resulting in missense alteration p.Pro41Ser (Supplementary Table 1). However, as both *DNER* variants have been deposited in the gnomAD browser in a homozygous state, we highly doubt their causality.

Identification of biallelic mutations in *POLR3A* in two individuals

In a further step, we searched for alterations in genes that have been previously connected to progeroid syndromes in single cases. This strategy revealed biallelic mutations in *POLR3A* (Jay et al. 2016) in individuals 1 and 4. Individual 1 bears compound heterozygosity for two variants within the splice acceptor site of intron 25, a paternally inherited c.3337-5T > A and a maternally inherited c.3337-1G > A. Individual 4 also bears compound heterozygosity, namely a maternally inherited c.760C > T, resulting in a nonsense mutation p.(Arg254*) and a paternally inherited c.3337-5T > A; the latter is notably the identical variant as also identified in individual 1. None of these variants were found in dbSNP, 1000 Genomes, the ExAC or the gnomAD browser

in the homozygous state and the heterozygous carriers were extremely rare (Table 4). The p.(Arg254*) is predicted to lead to a premature termination codon likely activating non-sense-mediated mRNA decay. On the other hand, c.3337-1G > A and c.3337-5T > A most probably affect splicing as predicted by the *Splice Site Prediction by Neural Network* (Berkeley Drosophila Genome Project; http://www.fruitfly. org/seq_tools/splice.html); namely this prediction tool suggests that the c.3337-1G > A completely abolishes the splice acceptor site, whereas c.3337-5T > A results in a weaker splice acceptor site with a score of 0.32 compared to a score of 0.79 that is assigned to the wild-type sequence. To test for the predicted splicing defect for the variant c.3337-5T > A, we performed RT-PCR analysis and Sanger sequencing with RNA obtained from LCLs of the individual 4 and his parents. This analysis revealed that the c.3337-5T > A indeed resulted in an alternate splice form in which *POLR3A* exon 26 was skipped. The mutation and exon skipping was found in both the proband and his father, but was absent in his mother (Fig. 4).

Other mutations and genetic heterogeneity of juvenile progeroid syndromes

Given that analysis of trio-WES data revealed no likely pathogenic variant in known progeroid genes in four individuals, we searched for rare candidate variants (minor allele frequency MAF < 0.005) following an autosomal recessive or X-linked recessive mode of inheritance, as well as those that might have arisen at de novo.

Individual 3 was found to have a de novo heterozygous mutation in *COL1A1* c.64G > C, p.(Gly22Arg). Mutations

in this gene are well known to cause osteogenesis imperfecta (OI) (Byers 1989) and some cases of Ehlers–Danlos syndrome (EDSARTH1) (Byers et al. 1997). The variant in individual 3 has been reported twice in the OI mutation database (http://www.le.ac.uk/genetics/collagen/). Both reports are from infants with OI type II, one of which was previously reported in the literature (Pollitt et al. 2006).

In individual 8, no de novo variant nor variants following autosomal recessive or X-linked mode of inheritance were identified.

In individual 9, bioinformatic filtering did not detect rare candidate variants following an autosomal recessive or X-linked recessive mode of inheritance. However, we identified a single non-annotated, de novo sequence change c.2763A > C, resulting in a missense alteration p.(Lys921Asn) in *SMC2*. To the best of our knowledge, mutations in *SMC2* have so far not been connected to any human disease. Given the previous link between genomic instability and segmental progeroid syndromes (Lessel et al. 2014; Yamagata et al. 1998), *SMC2* constitutes an interesting candidate gene for this progeroid disorder. However, as the identified amino acid substitution has a rather low Phred scaled CADD (v1.3) score of 16.95 (for de novo mutations), and is predicted to be "benign" by PolyPhen-2 and tolerated by SIFT (Table 4), we were reluctant at this point to perform functional analysis without identifying an additional patient with similar genotype and phenotype to elucidate the causality of this variant.
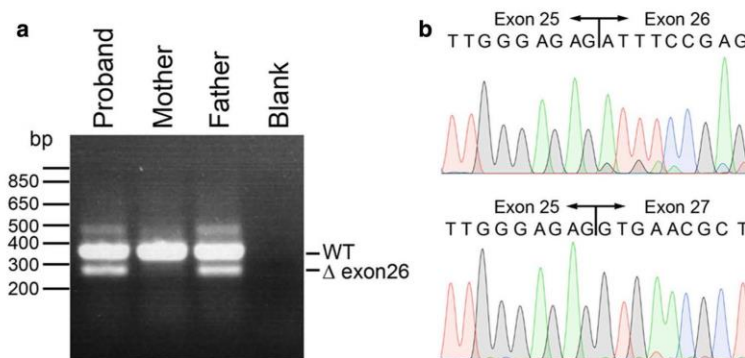
Fig. 4 *POLR3A* splicing defect caused by c.3337-5T > A mutation results in skipping of exon 26. Agarose gel electrophoresis of *POLR3A* RT-PCR products. The proband and father both carry the c.3337-5T > A mutation, resulting in a smaller band of ~ 287 bp corresponding to a cDNA missing exon 26 compared to the size of the wild-type band of ~ 380 bp (**a**). Sanger sequence traces of gel-extracted *POLR3A* RT-PCR products, demonstrating wild-type sequence of the larger band (top) and exon 26 skipping, both from individual 4 (bottom) (**b**)

Identification of additional *POLR3A* and *PYCR1* cases

After performing trio-WES analyses in the above-mentioned ten cases, four additional cases were referred with the putative clinical diagnosis of a juvenile progeroid syndrome. One of these cases, proband 11, highly resembled both probands 1 and 4 (Fig. 1), and the previously published Wiedemann–Rautenstrauch-like case (Jay et al. 2016). For this reason, we performed Sanger sequencing of all coding exons and the exon–intron boundaries of *POLR3A* using genomic DNA of the affected individual and her parents. However, we were only able to identify a single heterozygous alteration in this proband, namely a start loss mutation, c.3G > T, p.(Met1Ile), that was transmitted from the father. Due to the remarkable clinical similarities to the other two patients bearing biallelic mutations in *POLR3A*, we speculate that the second, maternal mutation, is either a deep intronic one, a copy-number variant (CNV), a balanced translocation or even affects a regulatory region of *POLR3A*.

The other three individuals, 12, 13 and 14, all presented with intrauterine growth retardation, triangular facial gestalt, sparse scalp hair, mandibular underdevelopment, thin-appearing and transparent skin with prominent veins, generalized lipodystrophy and joint hypermobility in the first year of life. Thus, we hypothesized that they may bear pathogenic *PYCR1* mutations. Indeed, this was confirmed by Sanger sequencing. Individual 12 bears a paternally inherited c.219_220insAC, p.(Ile74Thrfs*10). Notably, this is the identical frameshift mutation that we identified in individuals 7 and 10. In addition, he bears a maternally inherited c.772G > C, p.Val258Leu, that has been reported previously (Dimopoulou et al. 2013). Individual 13 bears a paternally inherited c.797 + 2_5delTGGG, and a likely maternally inherited c.540 + 1G > A, both of which have been reported previously (Dimopoulou et al. 2013; Reversade et al. 2009). We were unable to confirm that the second mutation was maternally inherited, as the mother deceased; however, this alteration was not identified in paternal DNA. Individual 14 bears a homozygous alteration c.769G > A, resulting in a missense mutation p.(Ala257Thr), and each of the parents is a heterozygous carrier. Again, the identical mutation has already been connected to *PYCR1* pathologies before (Reversade et al. 2009).

Discussion

Juvenile progeroid syndromes constitute a group of diseases characterized by clinical signs of premature aging starting in childhood. The best known and most extensively studied example of such diseases is Hutchinson–Gilford progeria syndrome (HGPS) (De Sandre-Giovannoli et al. 2003; Eriksson et al. 2003; Gordon et al. 1993). Next-generation

sequencing (NGS) is a powerful tool for delineating the genetic basis of monogenic diseases, including both the identification of novel disease genes and revealing the heterogeneous nature of Mendelian conditions. Given the rarity of these conditions, concerted efforts of open sharing NGS data from multiple groups are of utmost importance to dissect their genetic nature. Moreover, NGS-based studies have revealed several novel progeroid genes (Lessel et al. 2014, 2017; Puente et al. 2011). However, a full understanding of the genetic and clinical heterogeneity of juvenile progeroid syndromes is still lacking and the genetic cause of some of these syndromes, such as Wiedemann–Rautenstrauch syndrome (WRS), still remain largely unknown. Here, we present our joint collaborative efforts in the form of an extensive study of previously unclassified children affected by progeroid syndromes aimed at dissecting the genetic bases of their conditions. We, however, note that although all 14 studied cases were affected by an early-onset progeroid syndrome there was a considerable degree of clinical heterogeneity between them (Supplementary Table 2).

WRS, first described in 1977 by Rautenstrauch and Snigula (Rautenstrauch and Snigula 1977), has been suggested to constitute a syndrome characterized by neonatal progeroid features, including intrauterine growth retardation with subsequent failure to thrive, characteristic progeroid facial features, lipodystrophy and global developmental delay. Since the first description of two affected sisters which pointed to an autosomal recessive inheritance of the underlying genetic cause, more than 50 individuals have been clinically classified as WRS although with a huge phenotypic variability, as recently reviewed by Paolacci et al. (Paolacci et al. 2017). Despite tremendous progress in unravelling the genetics of several Mendelian disorders, which is mostly attributable to the rapid development of new technologies, the underlying genetic cause of WRS has still not been established yet. The latter is likely due to remarkable clinical heterogeneity of the documented cases. However, a recent study identified compound heterozygosity for two null mutations in *POLR3A* in a single WRS-like individual (Jay et al. 2016). Here, we identified two patients (individuals 1 and 4) with strikingly similar clinical characteristics and facial features to the published case which also bear compound heterozygosity for two *POLR3A* null mutations. Moreover, we report on another patient with comparable clinical characteristics and a remarkably similar facial gestalt. In this patient (individual 11), using direct Sanger sequencing of all coding exons and the exon–intron boundaries of *POLR3A*, only a single, paternally inherited, heterozygous mutation was identified. However, due to the remarkable similarities both to the previously published patient (Jay et al. 2016) and individuals 1 and 4 (Fig. 1; Table 1), we conjecture that the second, maternally inherited mutation, lies either within deep intronic or even regulatory regions of *POLR3A*,

80

or might be a copy-number variant comprising more than a single exon or even a balanced translocation. Notably, the other WRS-like patients bear a pathogenic intronic variant at positions that do not commonly lead to aberrant splicing, namely c.1909 + 18G > A and c.3337-5T > A. Thus, deep intronic and regulatory variants that are usually not covered by WES analysis might explain why POLR3A has not previously been established as the underlying genetic cause of some WRS-like conditions. From the clinical perspective, the previously reported WRS-like POLR3A patient died at 7 months of age following respiratory complications (Jay et al. 2016). Noteworthy, two of the WRS-like patients presented here (4 and 11) also had severe respiratory problems, especially in the perinatal period. However, they both survived beyond the first year of life, and individual 4 actually reached 13 years of age at study closure, suggesting that this is not a uniformly early lethal condition. Notably, while this manuscript was under review a further study independently confirmed biallelic POLR3A mutations, most of which were intronic ones, as the cause of the WRS-like condition (Paolacci et al. 2018). Taken together, POLR3A mutations following an autosomal recessive mode of inheritance are now firmly established as the genetic cause of a recognizable WRS-like syndrome.

Notably, biallelic mutations in POLR3A are known to cause the 4H leukodystrophy syndrome (hypomyelination, hypogonadotropic hypogonadism and hypodontia). The condition is characterized by early-onset ataxia, delayed dentition, hypomyelination, and hypogonadotropic hypogonadism (Bernard et al. 2011). However, concerning the age of onset and progression of neurologic symptoms, 4H leukodystrophy is characterized by both high inter- and intra-familial variability (Wolf et al. 2014). Compared to the POLR3A-associated WRS-like condition, none of the 4H leukodystrophy patients bear biallelic truncating mutations, e.g. all bear at least one missense mutation (Jay et al. 2016; Wolf et al. 2014). The latter may explain both the earlier, neonatal onset of the WRS-like condition as well as the more pronounced growth retardation and lipodystrophy, distinct facial anomalies and congenital respiratory complications, as previously suggested (Jay et al. 2016; Paolacci et al. 2017). On the other hand, given that both entities are characterized by neurologic dysfunction and dental anomalies, POLR3A-associated WRS-like condition may be regarded as the extreme form of the 4H leukodystrophy.

Recessive mutations in PYCR1 were initially associated with Cutis Laxa Type IIB with progeroid features (Reversade et al. 2009). However, further descriptions of patients bearing biallelic PYCR1 mutations in a large genotype–phenotype correlation study revealed a remarkable clinical heterogeneity and phenotypic continuum ranging from isolated wrinkly skin syndromes, gerodermia osteodysplastica, De Barsy syndrome to even patients classified as Hallermann–Streiff-like neonatal progeroid syndromes (Dimopoulou et al. 2013). Our initial trio-WES analysis of ten patients clinically classified as having a HGPS-like juvenile progeroid syndrome unexpectedly revealed biallelic PYCR1 mutations in 50% of probands (five cases). Notably, all of these cases did share some clinical characteristics with HGPS, albeit only in the first few years of life; namely all displayed triangular facial gestalt, sparse scalp hair, thin-appearing and translucent skin with prominent veins, mandibular underdevelopment and lipodystrophy. However, in contrast to HGPS, they displayed intrauterine growth retardation and later developed mild to moderate global developmental delay (GDD), and had various brain anomalies (Table 1). Importantly, in comparison with HGPS cases, which have a progressive and early fatal course of disease, progeroid and neurodevelopmental features of PYCR1, patients actually improve with time. This important clinical finding has already been documented in the literature (Dimopoulou et al. 2013).

It was previously reported that PYCR1-related disorders are difficult to diagnose based on the huge clinical heterogeneity. However, the findings in these five patients suggested that in some cases PYCR1 mutations might result in a clinically recognizable progeroid syndrome. This hypothesis is further supported by findings in three further patients (individuals 12, 13 and 14) in whom, based on the above-mentioned clinical findings, we speculated the existence of biallelic PYCR1 mutations as their underlying genetic cause and then confirmed this by direct Sanger sequencing. Although the clinical manifestations in the eight PYCR1-mutated individuals presented here are highly similar to the previous studies (Table 3), it is somewhat striking that only 14% of patients presented here developed wrinkled skin before 1 year of age, and one individual (individual 7) actually never presented this clinical sign. This is in contrast to both the findings in the initial PYCR1 mutation description leading to the classification of the disease as autosomal recessive cutis laxa (ARCL) (Reversade et al. 2009) and the large genotype–phenotype study (Dimopoulou et al. 2013), in whom all of the 68 presented patients had wrinkled skin. Notably, these data suggest that the genetic analysis of PYCR1 should be extended to all patients with unclassified juvenile segmental progeroid syndromes even if wrinkled skin is not present.

Regarding the spectrum of PYCR1 mutations, we identified two individuals bearing amino acid substitutions of the arginine at the position 119, p.(Arg119His) and p.(Arg119Cys). As substitutions of this arginine have previously been described in eight individuals (Dimopoulou et al. 2013; Reversade et al. 2009), including p.(Arg119Gly), our data further suggest that this arginine is a hot spot PYCR1 amino acid. Moreover, we identified a recurrent 2-bp insertion c.219_220insAC, resulting in a frameshift mutation

Table 3 Comparison of clinical findings in *PYCR1*-mutated patients presented here and patients from previous studies as summarized before (Dimopoulou et al. 2013)

	Our study	Previous studies Dimopoulou et al. (%)
Wrinkled skin	86% (6/7)	~100
Joint hypermobility	71% (5/7)	~100
Typical facial gestalt	100% (8/8)	~100
Intrauterine growth retardation	100% (7/7)	~90
Psychomotor retardation	100% (6/6)	~90
Osteopenia	14% (1/7)	~75
Thin/translucent skin	100% (8/8)	~75
Microcephaly	100% (7/7)	~75
Postnatal growth retardation	60% (3/5)	~75
Muscular hypotonia	100% (7/7)	~70
Contractures	25% (2/8)	~50
Hernias	43% (3/7)	~35
Blue sclera	0% (0/7)	~30
Strabismus	14% (1/7)	~30
Cataract/corneal opacities	14% (1/7)	~10

p.(Ile74Thr*fs**10) in three individuals. Interestingly, proband 7 bearing this frameshift mutation in the homozygous state was the most severely affected *PYCR1* patient in our case series. However, the exact *PYCR1* genotype–phenotype correlation still remains unknown (Dimopoulou et al. 2013). One explanation could be that some of the individuals documented in the literature, in addition to mutations in *PYCR1*, bear a further distinct genetic factor, likely in the genome region that is not covered by WES, which results in the somewhat different clinical outcome.

Interestingly, our trio-WES analysis identified a de novo mutation in *COL1A1* in individual 3. The identical mutation was previously documented in the OI mutation database in two further infants with OI type II, a commonly perinatal lethal syndrome (Marini and Smith 2000; Van Dijk and Sillence 2014). Although, detailed clinical data on these two infants are not available, it is worth noting that individual 3 in our study survived beyond the ninth birthday. Moreover, in addition to common OI features such as intrauterine growth retardation, multiple prenatal and postnatal fractures, and blue sclerae, he additionally displayed several features not commonly observed in OI type II. The latter include multiple contractures of the large joints, global developmental delay, global lipodystrophy, blepharophimosis, sparse and thin hair, and mandibular underdevelopment (Van Dijk and

Table 4 Population frequencies and bioinformatic predictions of the rare variants identified in this study

	ExAC	gnomAD	Polyphen-2	SIFT	I-Mutant	CADD	BDGP
POLR3A							
p.M1I	0/0/121360	0/1/246230	Probably damaging	Damaging	Decreased stability	33	–
p.R254*	0/3/121300	0/9/277188	–	–	–	37	–
c.3337-5T>A	0/1/108818	0/1/242920	–	–	–	8.67	0.79–>0.32
c.3337-1G>A	0/0/108818	0/0/242920	–	–	–	3.95	0.79–>0
PYCR1							
p.K71N*fs**10	0/0/113986	0/1/30918	–	–	–	33	–
p.I74T*fs**10	0/0/113986	0/0/245176	–	–	–	32	–
p.R119C	0/10/114118	0/34/273316	Probably damaging	Damaging	Decreased stability	28.8	–
p.R119H	0/3/114566	0/3/242550	Probably damaging	Damaging	Decreased stability	28.9	–
p.A179T	0/3/113196	0/5/272934	Probably damaging	Damaging	Decreased stability	33	–
c.540+1G>A	0/3/112300	0/5/242262	–	–	–	25.8	0.98–>0
c.633+1G>C	0/2/21260	0/6/199450	–	–	–	31	0.49–>0
p.A257T	0/5/109454	0/9/274864	Probably damaging	Damaging	Decreased stability	30	–
p.V258L	0/0/109454	0/0/274864	Probably damaging	Damaging	Decreased stability	29.5	–
c.797+2_5delTGGG	0/0/107108	0/0/243200	–	–	–	24.2	0.30–>0
p.R313L	0/0/120196	0/0/245668	Benign	Tolerated	Decreased stability	2.5	–
COL1A1							
p.G22R	0/0/118552	0/0/245568	Probably damaging	Tolerated	Decreased stability	23.9	–
SMC2							
p.K921N	0/0/120326	0/0/274588	Benign	Tolerated	Decreased stability	16.95	–

ExAC Exome Aggregation Consortium, *gnomAD* genome aggregation database, *Polyphen2* polymorphism phenotyping v2, *SIFT* sorting intolerant from tolerant, *I-Mutant* neural network-based predictor of protein stability, *CADD* combined annotation-dependent depletion, *BDGP* splice site prediction by neural network

82

Table 5 Comparison of clinical characteristics of individuals 8 and 9 to mandibular hypoplasia, deafness, progeroid features, and lipodystrophy syndrome (MDPL, Lessel et al. 2015), marfanoid–prog- eroid–lipodystrophy syndrome (MPLS, Passarge et al. 2016) and Berardinelli–Seip congenital lipodystrophy (BSCL, Van Maldergem L. 2016)

	Individual 8	Individual 9	MDPL Lessel et al.	MPLS Passarge et al.	BSCL Van Maldergem L.
Sex	Male	Male	7 female and 6 male	6 female and 1 male	Female and male
Age	10 years	12 years 9 months	10–62 years	3.5–27 years	Various
Ethnicity	European	European	Various	Various	Various
Intrauterine growth retardation	+	+	0/13	7/7	Rare
Triangular face	+	−	0/13	0/7	−
Sparse scalp hair	+	−	0/13	0/7	−
Greying or loss of hair	−	−	3/13	0/7	−
Prominent scalp veins	+	−	0/13	0/7	−
Dental crowding/irregular teeth	−	−	10/13	0/7	−
Myopia	−	−	0/13	6/7	−
Cataracts	+	−	0/13	0/7	−
Hearing impairment	−	−	10/13	0/7	−
Joint contractures	−	+	5/13		−
Hyperextensible joints	−	−	0/13	5/7	−
Arachnodactyly	−	−	0/13	7/7	−
Bone age	Advanced	Delayed	n.r	n.r	Advanced
Osteopenia	−	−	6/13	n.r	−
Scoliosis	−	+	0/13	2/6	−
Osteopenia	−	−	6/13		−
Congenital lipodystrophy	+	−	0/13	7/7	+
Lipodystrophy	+	+	13/13	7/7	+
Stature	Short	−	Short: 8/13	tall	−
Acromegaly	−	−	0/13	n.r	+
Muscle wasting	−	+	11/13	n.r	−
Abnormal cognitive function	−	−	1/13	0/7	Mild to moderate
Cardiac problems	−	−	0/13	Aortic root dilatation 3/7 Mitral valve prolapse 3/7	Hypertrophic cardiomyopathy

+ present, − absent, *n.r.* not reported

Sillence 2014). Therefore, we cannot completely exclude the possibility that individual 3, in addition to the mutation in *COL1A1*, bears a further distinct genetic or epigenetic factor resulting in a somewhat different clinical outcome from the previously documented individuals. A further intriguing possibility is that individual 3 is actually a mosaic for the *COL1A1* mutation. However, as further tissues from this individual were not available we were not able to further investigate this possibility.

Importantly, even using trio-WES analysis performed according to high standards, sufficient coverage and expert bioinformatic analysis, the study did not lead to a definitive molecular diagnosis in two individuals (individuals 8 and 9). In individual 8, we did not identify a single candidate rare variant, whereas in individual 9 a potential novel candidate gene, *SMC2*, was identified. However, bioinformatic predictions do not provide evidence for the pathogenicity of

the latter (Table 4). Interestingly, both individuals, although not displaying identical clinical signs and symptoms, are affected by a progeroid lipodystrophy somewhat mimicking mandibular hypoplasia, deafness, progeroid features, and lipodystrophy syndrome, marfanoid–progeroid–lipodystrophy syndrome and Berardinelli–Seip congenital lipodystrophy (Table 5). Taken together, these data further emphasize genetic heterogeneity of progeroid syndromes suggesting the existence of further, yet uncovered, progeroid loci. Moreover, these data underscore the utility of whole-genome sequencing to delineate the underlying genetic cause of some progeroid cases. Thus, elucidation of the genetic cause in these two patients as well as delineating novel progeroid loci will require further work and will be the main focus of our future studies.

In conclusion, due to our joint collaborative efforts a molecular diagnosis was achieved in 11/14 (~79%) of

previously undiagnosed progeroid patients. Our data confirm biallelic mutations in *POLR3A* as the genetic cause of a recognizable, neonatal, Wiedemann–Rautenstrauch-like progeroid syndrome, and suggest that the genetic analysis of *POLR3A* should be performed in WRS-like patients. Furthermore, our data further expand the clinical spectrum associated with *PYCR1* mutations and suggest the clinical criteria for early diagnosis of this condition. Last but not least, speculation based on our data suggests the existence of further genetic loci for early-onset progeroid conditions that may be solved by application of whole-genome sequencing.

Compliance with ethical standards

Conflict of interest The authors declare that they have no conflict of interest.

Research involving human participants The study has ongoing approval from the Hasbro Children's Hospital and the University Medical Center Hamburg-Eppendorf Institutional Review Boards. The study was performed in accordance with the Declaration of Helsinki protocols.

Informed consent All biological samples were obtained following written informed consent from studied individuals or their legal representatives.

References

Bernard G, Chouery E, Putorti ML, Tetreault M, Takanohashi A, Carosso G, Clement I, Boespflug-Tanguy O, Rodriguez D, Delague V, Abou Ghoch J, Jalkh N, Dorboz I, Fribourg S, Teichmann M, Megarbane A, Schiffmann R, Vanderver A, Brais B (2011) Mutations of POLR3A encoding a catalytic subunit of RNA polymerase Pol III cause a recessive hypomyelinating leukodystrophy. Am J Hum Genet 89:415–423. https://doi.org/10.1016/j.ajhg.2011.07.014

Byers PH (1989) Inherited disorders of collagen gene structure and expression. Am J Med Genet 34:72–80. https://doi.org/10.1002/ajmg.1320340114

Byers PH, Duvic M, Atkinson M, Robinow M, Smith LT, Krane SM, Greally MT, Ludman M, Matalon R, Pauker S, Quanbeck D, Schwarze U (1997) Ehlers-Danlos syndrome type VIIA and VIIB result from splice-junction mutations or genomic deletions that involve exon 6 in the COL1A1 and COL1A2 genes of type I collagen. Am J Med Genet 72:94–105

Chen L, Lee L, Kudlow BA, Dos Santos HG, Sletvold O, Shafeghati Y, Botha EG, Garg A, Hanson NB, Martin GM, Mian IS, Kennedy BK, Oshima J (2003) LMNA mutations in atypical Werner's syndrome. Lancet 362:440–445. https://doi.org/10.1016/S0140-6736(03)14069-X

Chong JX, McMillin MJ, Shively KM, Beck AE, Marvin CT, Armenteros JR, Buckingham KJ, Nkinsi NT, Boyle EA, Berry MN, Bocian M, Foulds N, Uzielli ML, Haldeman-Englert C, Hennekam RC, Kaplan P, Kline AD, Mercer CL, Nowaczyk MJ, Klein Wassink-Ruiter JS, McPherson EW, Moreno RA, Scheuerle AE, Shashi V, Stevens CA, Carey JC, Monteil A, Lory P, Tabor HK, Smith JD, Shendure J, Nickerson DA, Bamshad MJ, University of Washington Center for Mendelian G (2015) De novo mutations in NALCN cause a syndrome characterized by congenital contractures of the limbs and face, hypotonia, and developmental delay. Am J Hum Genet 96:462–473. https://doi.org/10.1016/j.ajhg.2015.01.003

De Sandre-Giovannoli A, Bernard R, Cau P, Navarro C, Amiel J, Boccaccio I, Lyonnet S, Stewart CL, Munnich A, Le Merrer M, Levy N (2003) Lamin a truncation in Hutchinson-Gilford progeria. Science 300: 2055. https://doi.org/10.1126/science.1084125

Dimopoulou A, Fischer B, Gardeitchik T, Schroter P, Kayserili H, Schlack C, Li Y, Brum JM, Barisic I, Castori M, Spaich C, Fletcher E, Mahayri Z, Bhat M, Girisha KM, Lachlan K, Johnson D, Phadke S, Gupta N, Simandlova M, Kabra M, David A, Nijtmans L, Chitayat D, Tuysuz B, Brancati F, Mundlos S, Van Maldergem L, Morava E, Wollnik B, Kornak U (2013) Genotype-phenotype spectrum of PYCR1-related autosomal recessive cutis laxa. Mol Genet Metab 110:352–361. https://doi.org/10.1016/j.ymgme.2013.08.009

Eriksson M, Brown WT, Gordon LB, Glynn MW, Singer J, Scott L, Erdos MR, Robbins CM, Moses TY, Berglund P, Dutra A, Pak E, Durkin S, Csoka AB, Boehnke M, Glover TW, Collins FS (2003) Recurrent de novo point mutations in lamin A cause Hutchinson-Gilford progeria syndrome. Nature 423:293–298. https://doi.org/10.1038/nature01629

Garg A, Subramanyam L, Agarwal AK, Simha V, Levine B, D'Apice MR, Novelli G, Crow Y (2009) Atypical progeroid syndrome due to heterozygous missense LMNA mutations. J Clin Endocrinol Metab 94:4971–4983. https://doi.org/10.1210/jc.2009-0472

Gordon LB, Brown WT, Collins FS (1993) Hutchinson–Gilford progeria syndrome. In: Adam MP, Ardinger HH, Pagon RA, Wallace SE, Bean LJH, Stephens K, Amemiya A (eds) GeneReviews((R)), Seattle

Graul-Neumann LM, Kienitz T, Robinson PN, Baasanjav S, Karow B, Gillessen-Kaesbach G, Fahsold R, Schmidt H, Hoffmann K, Passarge E (2010) Marfan syndrome with neonatal progeroid syndrome-like lipodystrophy associated with a novel frameshift mutation at the 3' terminus of the FBN1-gene. Am J Med Genet A 152A:2749–2755. https://doi.org/10.1002/ajmg.a.33690

Hisama FM, Lessel D, Leistritz D, Friedrich K, McBride KL, Pastore MT, Gottesman GS, Saha B, Martin GM, Kubisch C, Oshima J (2011) Coronary artery disease in a Werner syndrome-like form of progeria characterized by low levels of progerin, a splice variant of lamin A. Am J Med Genet A 155A:3002–3006. https://doi.org/10.1002/ajmg.a.34336

Jay AM, Conway RL, Thiffault I, Saunders C, Farrow E, Adams J, Toriello HV (2016) Neonatal progeroid syndrome associated with biallelic truncating variants in POLR3A. Am J Med Genet A 170:3343–3346. https://doi.org/10.1002/ajmg.a.37960

Lessel D, Vaz B, Halder S, Lockhart PJ, Marinovic-Terzic I, Lopez-Mosqueda J, Philipp M, Sim JC, Smith KR, Oehler J, Cabrera E, Freire R, Pope K, Nahid A, Norris F, Leventer RJ, Delatycki MB, Barbi G, von Ameln S, Hogel J, Degoricija M, Fertig R, Burkhalter MD, Hofmann K, Thiele H, Altmuller J, Nurnberg G, Nurnberg P, Bahlo M, Martin GM, Aalfs CM, Oshima J, Terzic

J, Amor DJ, Dikic I, Ramadan K, Kubisch C (2014) Mutations in SPRTN cause early onset hepatocellular carcinoma, genomic instability and progeroid features. Nat Genet 46:1239–1244. https://doi.org/10.1038/ng.3103

Lessel D, Hisama FM, Szakszon K, Saha B, Sanjuanelo AB, Salbert BA, Steele PD, Baldwin J, Brown WT, Piussan C, Plauchu H, Szilvassy J, Horkay E, Hogel J, Martin GM, Herr AJ, Oshima J, Kubisch C (2015) POLD1 germline mutations in patients initially diagnosed with werner syndrome. Hum Mutat 36:1070–1079. https://doi.org/10.1002/humu.22833

Lessel D, Wu D, Trujillo C, Ramezani T, Lessel I, Alwasiyah MK, Saha B, Hisama FM, Rading K, Goebel I, Schutz P, Speit G, Hogel J, Thiele H, Nurnberg G, Nurnberg P, Hammerschmidt M, Zhu Y, Tong DR, Katz C, Martin GM, Oshima J, Prives C, Kubisch C (2017) Dysfunction of the MDM2/p53 axis is linked to premature aging. J Clin Invest 127:3598–3608. https://doi.org/10.1172/JCI92171

Marini J, Smith SM (2000) Osteogenesis imperfecta. In: De Groot LJ, Chrousos G, Dungan K, Feingold KR, Grossman A, Hershman JM, Koch C, Korbonits M, McLachlan R, New M, Purnell J, Rebar R, Singer F, Vinik A (eds) Endotext, South Dartmouth

Martin GM (1978) Genetic syndromes in man with potential relevance to the pathobiology of aging. Birth Defects Orig Artic Ser 14:5–39

Navarro CL, Esteves-Vieira V, Courrier S, Boyer A, Duong Nguyen T, Huong le TT, Meinke P, Schroder W, Cormier-Daire V, Sznajer Y, Amor DJ, Lagerstedt K, Biervliet M, van den Akker PC, Cau P, Roll P, Levy N, Badens C, Wehnert M, De Sandre-Giovannoli A (2014) New ZMPSTE24 (FACE1) mutations in patients affected with restrictive dermopathy or related progeroid syndromes and mutation update. Eur J Hum Genet 22:1002–1011. https://doi.org/10.1038/ejhg.2013.258

Nicolas E, Golemis EA, Arora S (2016) POLD1: Central mediator of DNA replication and repair, and implication in cancer and other pathologies. Gene 590:128–141. https://doi.org/10.1016/j.gene.2016.06.031

Paolacci S, Bertola D, Franco J, Mohammed S, Tartaglia M, Wollnik B, Hennekam RC (2017) Wiedemann-rautenstrauch syndrome: a phenotype analysis. Am J Med Genet A. https://doi.org/10.1002/ajmg.a.38246

Paolacci S, Li Y, Agolini E, Bellacchio E, Arboleda-Bustos CE, Carrero D, Bertola D, Al-Gazali L, Alders M, Altmuller J, Arboleda G, Beleggia F, Bruselles A, Ciolfi A, Gillessen-Kaesbach G, Krieg T, Mohammed S, Muller C, Novelli A, Ortega J, Sandoval A, Velasco G, Yigit G, Arboleda H, Lopez-Otin C, Wollnik B, Tartaglia M, Hennekam RC (2018) Specific combinations of biallelic POLR3A variants cause Wiedemann-Rautenstrauch syndrome. J Med Genet. https://doi.org/10.1136/jmedgenet-2018-105528

Passarge E, Robinson PN, Graul-Neumann LM (2016) Marfanoid-progeroid-lipodystrophy syndrome: a newly recognized fibrillinopathy. Eur J Hum Genet 24:1244–1247. https://doi.org/10.1038/ejhg.2016.6

Pollitt R, McMahon R, Nunn J, Bamford R, Afifi A, Bishop N, Dalton A (2006) Mutation analysis of COL1A1 and COL1A2 in patients diagnosed with osteogenesis imperfecta type I-IV. Hum Mutat 27:716. https://doi.org/10.1002/humu.9430

Puente XS, Quesada V, Osorio FG, Cabanillas R, Cadinanos J, Fraile JM, Ordonez GR, Puente DA, Gutierrez-Fernandez A, Fanjul-Fernandez M, Levy N, Freije JM, Lopez-Otin C (2011) Exome sequencing and functional analysis identifies BANF1 mutation as the cause of a hereditary progeroid syndrome. Am J Hum Genet 88:650–656. https://doi.org/10.1016/j.ajhg.2011.04.010

Rautenstrauch T, Snigula F (1977) Progeria: a cell culture study and clinical report of familial incidence. Eur J Pediatr 124:101–111

Reversade B, Escande-Beillard N, Dimopoulou A, Fischer B, Chng SC, Li Y, Shboul M, Tham PY, Kayserili H, Al-Gazali L, Shahwan M, Brancati F, Lee H, O'Connor BD, Schmidt-von Kegler M, Merriman B, Nelson SF, Masri A, Alkazaleh F, Guerra D, Ferrari P, Nanda A, Rajab A, Markie D, Gray M, Nelson J, Grix A, Sommer A, Savarirayan R, Janecke AR, Steichen E, Sillence D, Hausser I, Budde B, Nurnberg G, Nurnberg P, Seemann P, Kunkel D, Zambruno G, Dallapiccola B, Schuelke M, Robertson S, Hamamy H, Wollnik B, Van Maldergem L, Mundlos S, Kornak U (2009) Mutations in PYCR1 cause cutis laxa with progeroid features. Nat Genet 41:1016–1021. https://doi.org/10.1038/ng.413

Saha B, Lessel D, Hisama FM, Leistritz DF, Friedrich K, Martin GM, Kubisch C, Oshima J (2010) A novel LMNA mutation causes altered nuclear morphology and symptoms of familial partial lipodystrophy (Dunnigan variety) with progeroid features. Mol Syndromol 1:127–132. https://doi.org/10.1159/000320166

Schrauwen I, Szelinger S, Siniard AL, Kurdoglu A, Corneveaux JJ, Malenica I, Richholt R, Van Camp G, De Both M, Swaminathan S, Turk M, Ramsey K, Craig DW, Narayanan V, Huentelman MJ (2015) A frame-shift mutation in CAV1 is associated with a severe neonatal progeroid and lipodystrophy syndrome. PLoS One 10:e0131797. https://doi.org/10.1371/journal.pone.0131797

Soria-Valles C, Carrero D, Gabau E, Velasco G, Quesada V, Barcena C, Moens M, Fieggen K, Mohrcken S, Owens M, Puente DA, Asensio O, Loeys B, Perez A, Benoit Y, Wuyts W, Levy N, Hennekam RC, De Sandre-Giovannoli A, Lopez-Otin C (2016) Novel LMNA mutations cause an aggressive atypical neonatal progeria without progerin accumulation. J Med Genet. https://doi.org/10.1136/jmedgenet-2015-103695

Van Maldergem L (1993) Berardinelli-seip congenital lipodystrophy. In: Adam MP, Ardinger HH, Pagon RA, Wallace SE, Bean LJH, Stephens K, Amemiya A (eds) GeneReviews((R)), Seattle

Van Dijk FS, Sillence DO (2014) Osteogenesis imperfecta: clinical diagnosis, nomenclature and severity assessment. Am J Med Genet A 164A:1470–1481. https://doi.org/10.1002/ajmg.a.36545

Wambach JA, Wegner DJ, Patni N, Kircher M, Willing MC, Baldridge D, Xing C, Agarwal AK, Vergano SAS, Patel C, Grange DK, Kenney A, Najaf T, Nickerson DA, Bamshad MJ, Cole FS, Garg A (2018) Bi-allelic POLR3A loss-of-function variants cause autosomal-recessive Wiedemann–Rautenstrauch syndrome. Am J Hum Genet. https://doi.org/10.1016/j.ajhg.2018.10.010

Weedon MN, Ellard S, Prindle MJ, Caswell R, Allen HL, Oram R, Godbole K, Yajnik CS, Sbraccia P, Novelli G, Turnpenny P, McCann E, Goh KJ, Wang Y, Fulford J, McCulloch LJ, Savage DB, O'Rahilly S, Kos K, Loeb LA, Semple RK, Hattersley AT (2013) An in-frame deletion at the polymerase active site of POLD1 causes a multisystem disorder with lipodystrophy. Nat Genet 45:947–950. https://doi.org/10.1038/ng.2670

Wolf NI, Vanderver A, van Spaendonk RM, Schiffmann R, Brais B, Bugiani M, Sistermans E, Catsman-Berrevoets C, Kros JM, Pinto PS, Pohl D, Tirupathi S, Stromme P, de Grauw T, Fribourg S, Demos M, Pizzino A, Naidu S, Guerrero K, van der Knaap MS, Bernard G, Group HR (2014) Clinical spectrum of 4H leukodystrophy caused by POLR3A and POLR3B mutations. Neurology 83:1898–1905. https://doi.org/10.1212/WNL.0000000000001002

Yamagata K, Kato J, Shimamoto A, Goto M, Furuichi Y, Ikeda H (1998) Bloom's and Werner's syndrome genes suppress hyperrecombination in yeast sgs1 mutant: implication for genomic instability in human diseases. Proc Natl Acad Sci USA 95:8733–8738

85

Affiliations

Davor Lessel[1] · Ayse Bilge Ozel[2] · Susan E. Campbell[3] · Abdelkrim Saadi[4] · Martin F. Arlt[2] ·
Keisha Melodi McSweeney[5] · Vasilica Plaiasu[6] · Katalin Szakszon[7] · Anna Szőllős[7] · Cristina Rusu[8] ·
Armando J. Rojas[9] · Jaime Lopez-Valdez[10] · Holger Thiele[11] · Peter Nürnberg[11,12,13] · Deborah A. Nickerson[14] ·
Michael J. Bamshad[14] · Jun Z. Li[2] · Christian Kubisch[1] · Thomas W. Glover[2] · Leslie B. Gordon[15,16]

1   Institute of Human Genetics, University Medical Center
Hamburg-Eppendorf, Martinistrasse 52, 20246 Hamburg,
Germany

2   Department of Human Genetics, University of Michigan,
Ann Arbor, MI, USA

3   Center for Gerontology and Healthcare Research, Brown
University, Providence, RI, USA

4   Service de neurologie, CHU Ben Aknoun Alger, 2 route des
deux Bassins, BenAknoun,, Algers, Algeria

5   Oak Ridge Institute for Science and Education, Office
of Biotechnology Products, Center for Drug Evaluation
and Research, Food and Drug Administration,
20993 Silver Spring, MD, USA

6   Regional Center of Medical Genetics,
Alessandrescu-Rusescu INSMC, Bucharest, Romania

7   Department of Pediatrics, University of Debrecen, Debrecen,
Hungary

8   Department of Genetics, University Hospital Iasi, Iasi,
Romania

9   Instituto de Genética Humana, Facultad de Medicina,
Pontificia Universidad Javeriana, Bogotá, Colombia

10   Department of Genetics, Centenario Hospital Miguel
Hidalgo, Aguascalientes, Mexico

11   Cologne Center for Genomics, University of Cologne,
Cologne, Germany

12   Center for Molecular Medicine Cologne, University
of Cologne, Cologne, Germany

13   Cologne Excellence Cluster on Cellular Stress Responses
in Aging-Associated Diseases, University of Cologne,
Cologne, Germany

14   Department of Genome Sciences, University of Washington,
Seattle, USA

15   Warren Alpert Medical School of Brown University,
Providence, RI, USA

16   Department of Pediatrics, Division of Genetics, Hasbro
Children's Hospital, Providence, RI, USA

86

Supplementary material for:

Analyses of *LMNA*-negative juvenile progeroid cases confirms biallelic

***POLR3A* mutations in Wiedemann-Rautenstrauch-like syndrome and expands**

the phenotypic spectrum of *PYCR1* mutations

Davor Lessel[1,#], Ayse Bilge Ozel[2], Susan E. Campbell[3], Abdelkrim Saadi[4], Martin F Arlt[2], Keisha Melodi McSweeney[5], Vasilica Plaiasu[6], Katalin Szakszon[7], Anna Szőllős[7], Cristina Rusu[8], Armando J. Rojas[9], Jaime Lopez-Valdez[10], Holger Thiele[11], Peter Nürnberg[11,12,13], Deborah A. Nickerson[14], Michael J. Bamshad[14], Jun Z. Li[2], Christian Kubisch[1], Thomas W Glover[2,] Leslie B Gordon[15,16]

[1]Institute of Human Genetics, University Medical Center Hamburg-Eppendorf, Hamburg, Germany

[2]Department of Human Genetics, University of Michigan, Ann Arbor, Michigan, USA

[3]Center for Gerontology and Healthcare Research, Brown University, Providence, Rhode Island, USA

[4]Service de neurologie, CHU Ben Aknoun Alger, 2 route des deux Bassins, BenAknoun Alger, Algeria

[5]Oak Ridge Institute for Science and Education, Office of Biotechnology Products, Center for Drug Evaluation and Research, Food and Drug Administration, Silver Spring, MD 20993, USA

[6]Alessandrescu-Rusescu INSMC, Regional Center of Medical Genetics, Bucharest, Romania

[7]Department of Pediatrics, University of Debrecen, Debrecen, Hungary

[8]Department of Genetics, University Hospital Iasi, Iasi, Romania

[9]Instituto de Genética Humana, Facultad de Medicina, Pontificia Universidad Javeriana, Bogotá, Colombia

[10]Department of Genetics, Centenario Hospital Miguel Hidalgo, Aguascalientes, México

[11]Cologne Center for Genomics, University of Cologne, Cologne, Germany

[12]Center for Molecular Medicine Cologne, University of Cologne, Cologne, Germany

[13]Cologne Excellence Cluster on Cellular Stress Responses in Aging-Associated Diseases, University of Cologne, Cologne, Germany

[14]Department of Genome Sciences, University of Washington, Seattle, USA

[15]Warren Alpert Medical School of Brown University, Providence, Rhode Island, USA

[16]Department of Pediatrics, Division of Genetics, Hasbro Children's Hospital, Providence, Rhode Island, USA

[#]Corresponding author: Davor Lessel, MD
                            Institute of Human Genetics
                            University Medical Center Hamburg-Eppendorf
                            Martinistrasse 52
                            20246 Hamburg, Germany
                            Phone: +49-40-7410 51818
                            Fax: +49-40-7410 55138
                            Email: d.lessel@uke.de

Gene	Chr	Total Depth	Nucleotide Change	Protein Change	gnomAD	Inheritance
DNER	2	65	c.121C>T	p.(Pro41Ser)	6/162/282732	maternal
DNER	2	43	c.762T>A	p.(Asp254Glu)	1/315/43882	paternal
PYCR1	17	190	c.219_220insAC	p.(Ile74Thr*fs**10)	0/0/245176	paternal
PYCR1	17	63	c.938G>T	p.(Arg313Leu)	0/0/245668	maternal

Supplementary Table 1. Rare variants identified in individual 10

Individual	1	2	3	4	5	6	7	8	9	10	11	12	13	14
Intrauterine growth retardation	+	+	-	+	?	+	+	+	+	+	+	+	+	+
Postnatal growth retardation	+	?	+	+	?	+	+	+	-	-	+	-	?	?
Triangular face	+	+	-	+	+	+	+	+	-	+	+	+	+	+
Sparse scalp hair	-	+	+	+	+	+	+	+	-	+	+	+	+	+
Thin / translucent skin	+	+	+	+	+	+	+	+	+	+	+	+	+	+
Prominent scalp veins	+	+	+	+	+	+	+	+	-	+	+	+	+	+
Frontal bossing	+	+	+	+	+	-	+	-	-	+	+	+	-	-
Low set ears	+	+	-	+	+	-		-	-	-	+	-	-	-
Mandibular underdevelopment	+	+	+	+	+	+	+	+	+	+	+	+	+	+
Joint hypermobility	-	+	-	-	?	-	-	-	-	+	-	+	+	+
Joint contractures	+	-	+	+	+	-	-	-	+	-	-	-	+	-
Motor development delay	-	+	+	+	?	+	+	-	-	+	-	+	+	?
Muscular hypotonia	-	+	+	-	?	+	+	-	-	+	+	+	+	+
Impaired speech development	-	+	+	+	?	+	+	-	-	+	?	+	?	?
Dental anomalies	+	+	+	+	?	-	-	-	-	-	+	-	-	-
Cataract / corneal opacities	-	+	-	-	?	-	-	+	-	-	-	-	-	-
Osteopenia / osteoporosis	-	+	+	-	?	-	-	-	-	-	?	-	-	-
Lipodystrophy	+	+	+	+	+	+	+	+	+	+	+	+	+	+
Cardiac anomalies	-	+	-	+	?	-	-	-	-	-	+	-	-	+
Wrinkled skin	-	+	-		?	+	-	-	-	+	-	+	+	+
Microcephaly	?	+	-	-	?	+	+	?	-	+	+	+	+	+
Congenital respiratory problems	-	+	-	+	?	-	+	-	-	-	+	-	-	+
Hearing loss	-	+	-	-	?	-	-	-	-	-	-	-	-	-
Brain anomalies	?	+	?	?	?	+	+	?		+	+	?	+	+
Causative gene	PO	PY	CO	PO	PY	PY	PY	?	?	PY	PO	PY	PY	PY

+, present; -, absent; ?, unknown or not done; PO, *POLR3A*; PY, *PYCR1*; CO, *COL1A1*.

Supplementary Table 2. Clinical characteristics of all 14 patients presented here.

6) KRATKI SAŽETAK I NASLOV NA ENGLESKOM JEZIKU

IDENTIFICATION OF NOVEL MONOGENIC CAUSES OF SEGMENTAL PROGEROID SYNDROMES

Segmental progeroid syndromes are extremely rare, clinically and genetically heterogeneous disorders characterized by signs of premature / accelerated aging affecting multiple tissues or organs. The aim of the here presented studies was to identify novel monogenic causes of selected segmental progeroid syndromes. Using a combination of different genetic analyses, primarily utilizing next-generation sequencing technologies, accompanied in certain cases by *in-depth* functional characterization, using both cellular and animal models, I have identified biallelic mutations in *SPRTN*, *MDM2* and *POLR3A*, as genetic causes of Ruijs-Aalfs syndrome (OMIM # 616200), Lessel-Kubisch syndrome (OMIM # 618681) and Wiedemann–Rautenstrauch syndrome (OMIM # 264090), respectively. The impact of these results is two-fold. First, as in case of identification of novel genetic cause for any monogenic disorder, these results enable establishment of the proper diagnosis, assessment of the prognosis, accurate estimation of the risk of similar disorders in the patient's family members, and in the growing number of cases enable individualized support and prevention program. Secondly, from the translational perspective, especially mutations in *SPRTN* and *MDM2*, offer a strong basis for further studies aiming to further elucidate the pathophysiologic basis of carcinogenesis and hence identify novel and/or improved targeting strategies in cancer therapy.

7) LITERATURA

1.   Martin GM. Genetic modulation of senescent phenotypes in Homo sapiens. Cell. 2005;120(4):523-32.
2.   Lessel D, Kubisch C. Hereditary Syndromes with Signs of Premature Aging. Dtsch Arztebl Int. 2019;116(29-30):489-96.
3.   Carrero D, Soria-Valles C, Lopez-Otin C. Hallmarks of progeroid syndromes: lessons from mice and reprogrammed cells. Dis Model Mech. 2016;9(7):719-35.
4.   Lopez-Otin C, Blasco MA, Partridge L, Serrano M, Kroemer G. The hallmarks of aging. Cell. 2013;153(6):1194-217.
5.   Yu CE, Oshima J, Fu YH, Wijsman EM, Hisama F, Alisch R, et al. Positional cloning of the Werner's syndrome gene. Science. 1996;272(5259):258-62.
6.   Eriksson M, Brown WT, Gordon LB, Glynn MW, Singer J, Scott L, et al. Recurrent de novo point mutations in lamin A cause Hutchinson-Gilford progeria syndrome. Nature. 2003;423(6937):293-8.
7.   De Sandre-Giovannoli A, Bernard R, Cau P, Navarro C, Amiel J, Boccaccio I, et al. Lamin a truncation in Hutchinson-Gilford progeria. Science. 2003;300(5628):2055.
8.   Lessel D, Oshima J, Kubisch C. [Werner syndrome. A prototypical form of segmental progeria.]. Med Genet. 2012;24(4):262-7.
9.   Oshima J, Martin GM, Hisama FM. Werner Syndrome. In: Adam MP, Ardinger HH, Pagon RA, Wallace SE, Bean LJH, Stephens K, et al., editors. GeneReviews((R)). Seattle (WA)1993.
10.   Ellis NA, Groden J, Ye TZ, Straughen J, Lennon DJ, Ciocci S, et al. The Bloom's syndrome gene product is homologous to RecQ helicases. Cell. 1995;83(4):655-66.
11.   Kitao S, Shimamoto A, Goto M, Miller RW, Smithson WA, Lindor NM, et al. Mutations in RECQL4 cause a subset of cases of Rothmund-Thomson syndrome. Nat Genet. 1999;22(1):82-4.
12.   Rossi ML, Ghosh AK, Bohr VA. Roles of Werner syndrome protein in protection of genome integrity. DNA Repair (Amst). 2010;9(3):331-44.
13.   Salk D, Au K, Hoehn H, Stenchever MR, Martin GM. Evidence of clonal attenuation, clonal succession, and clonal expansion in mass cultures of aging Werner's syndrome skin fibroblasts. Cytogenet Cell Genet. 1981;30(2):108-17.
14.   Friedrich K, Lee L, Leistritz DF, Nurnberg G, Saha B, Hisama FM, et al. WRN mutations in Werner syndrome patients: genomic rearrangements, unusual intronic mutations and ethnic-specific alterations. Hum Genet. 2010;128(1):103-11.
15.   Saha B, Lessel D, Nampoothiri S, Rao AS, Hisama FM, Peter D, et al. Ethnic-Specific WRN Mutations in South Asian Werner Syndrome Patients: Potential Founder Effect in Patients with Indian or Pakistani Ancestry. Mol Genet Genomic Med. 2013;1(1):7-14.
16.   Yokote K, Chanprasert S, Lee L, Eirich K, Takemoto M, Watanabe A, et al. WRN Mutation Update: Mutation Spectrum, Patient Registries, and Translational Prospects. Hum Mutat. 2017;38(1):7-15.
17.   Saha B, Lessel D, Hisama FM, Leistritz DF, Friedrich K, Martin GM, et al. A Novel LMNA Mutation Causes Altered Nuclear Morphology and Symptoms of Familial Partial Lipodystrophy (Dunnigan Variety) with Progeroid Features. Mol Syndromol. 2010;1(3):127-32.
18.   Hisama FM, Lessel D, Leistritz D, Friedrich K, McBride KL, Pastore MT, et al. Coronary artery disease in a Werner syndrome-like form of progeria characterized by low levels of progerin, a splice variant of lamin A. Am J Med Genet A. 2011;155A(12):3002-6.
19.   Sargolzaeiaval F, Zhang J, Schleit J, Lessel D, Kubisch C, Precioso DR, et al. CTC1 mutations in a Brazilian family with progeroid features and recurrent bone fractures. Mol Genet Genomic Med. 2018;6(6):1148-56.

20.	Lessel D, Saha B, Hisama F, Kaymakamzade B, Nurlu G, Gursoy-Ozdemir Y, et al. Atypical Aicardi-Goutieres syndrome: is the WRN locus a modifier? Am J Med Genet A. 2014;164A(10):2510-3.
21.	Lessel D, Hisama FM, Szakszon K, Saha B, Sanjuanelo AB, Salbert BA, et al. POLD1 Germline Mutations in Patients Initially Diagnosed with Werner Syndrome. Hum Mutat. 2015;36(11):1070-9.
22.	Gordon LB, Brown WT, Collins FS. Hutchinson-Gilford Progeria Syndrome. In: Adam MP, Ardinger HH, Pagon RA, Wallace SE, Bean LJH, Stephens K, et al., editors. GeneReviews((R)). Seattle (WA)1993.
23.	Lin F, Worman HJ. Structural organization of the human gene encoding nuclear lamin A and nuclear lamin C. J Biol Chem. 1993;268(22):16321-6.
24.	Andres V, Gonzalez JM. Role of A-type lamins in signaling, transcription, and chromatin organization. J Cell Biol. 2009;187(7):945-57.
25.	Broers JL, Ramaekers FC, Bonne G, Yaou RB, Hutchison CJ. Nuclear lamins: laminopathies and their role in premature ageing. Physiol Rev. 2006;86(3):967-1008.
26.	Goldman RD, Shumaker DK, Erdos MR, Eriksson M, Goldman AE, Gordon LB, et al. Accumulation of mutant lamin A causes progressive changes in nuclear architecture in Hutchinson-Gilford progeria syndrome. Proc Natl Acad Sci U S A. 2004;101(24):8963-8.
27.	Capell BC, Erdos MR, Madigan JP, Fiordalisi JJ, Varga R, Conneely KN, et al. Inhibiting farnesylation of progerin prevents the characteristic nuclear blebbing of Hutchinson-Gilford progeria syndrome. Proc Natl Acad Sci U S A. 2005;102(36):12879-84.
28.	Lessel D, Ozel AB, Campbell SE, Saadi A, Arlt MF, McSweeney KM, et al. Analyses of LMNA-negative juvenile progeroid cases confirms biallelic POLR3A mutations in Wiedemann-Rautenstrauch-like syndrome and expands the phenotypic spectrum of PYCR1 mutations. Hum Genet. 2018;137(11-12):921-39.
29.	Paolacci S, Bertola D, Franco J, Mohammed S, Tartaglia M, Wollnik B, et al. Wiedemann-Rautenstrauch syndrome: A phenotype analysis. Am J Med Genet A. 2017;173(7):1763-72.
30.	Lessel D, Vaz B, Halder S, Lockhart PJ, Marinovic-Terzic I, Lopez-Mosqueda J, et al. Mutations in SPRTN cause early onset hepatocellular carcinoma, genomic instability and progeroid features. Nat Genet. 2014;46(11):1239-44.
31.	Lessel D, Wu D, Trujillo C, Ramezani T, Lessel I, Alwasiyah MK, et al. Dysfunction of the MDM2/p53 axis is linked to premature aging. J Clin Invest. 2017;127(10):3598-608.
32.	Reversade B, Escande-Beillard N, Dimopoulou A, Fischer B, Chng SC, Li Y, et al. Mutations in PYCR1 cause cutis laxa with progeroid features. Nat Genet. 2009;41(9):1016-21.
33.	Dimopoulou A, Fischer B, Gardeitchik T, Schroter P, Kayserili H, Schlack C, et al. Genotype-phenotype spectrum of PYCR1-related autosomal recessive cutis laxa. Mol Genet Metab. 2013;110(3):352-61.